IMPROVEMENT TO A TRANSPORT MODEL OF ASPHALT BINDER OXIDATION IN PAVEMENTS: PAVEMENT TEMPERATURE MODELING, OXYGEN DIFFUSIVITY IN ASPHALT BINDERS AND MASTICS, AND PAVEMENT AIR VOID CHARACTERIZATION

A Dissertation

by

RONGBIN HAN

Submitted to the Office of Graduate Studies of
Texas A&M University
in partial fulfillment of the requirements for the degree of

DOCTOR OF PHILOSOPHY

May 2011

Major Subject: Chemical Engineering

IMPROVEMENT TO A TRANSPORT MODEL OF ASPHALT BINDER OXIDATION IN PAVEMENTS: PAVEMENT TEMPERATURE MODELING, OXYGEN DIFFUSIVITY IN ASPHALT BINDERS AND MASTICS, AND PAVEMENT AIR VOID CHARACTERIZATION

A Dissertation

by

RONGBIN HAN

Submitted to the Office of Graduate Studies of
Texas A&M University
in partial fulfillment of the requirements for the degree of

DOCTOR OF PHILOSOPHY

Approved by:

Chair of Committee,	Charles J. Glover
Committee Members,	Amy Epps Martin
	Mark Holtzapple
	Zhengdong Cheng
Head of Department,	Michael Pishko

May 2011

Major Subject: Chemical Engineering

ABSTRACT

Improvements to a Transport Model of Asphalt Binder Oxidation in Pavements: Pavement Temperature Modeling, Oxygen Diffusivity in Asphalt Binders and Mastics, and Pavement Air Void Characterization.

(May 2011)

Rongbin Han, B.S., Tianjin University;
M.S., National University of Singapore
Chair of Advisory Committee: Dr. Charles J. Glover

Although evidence is mounting that asphalt binder oxidizes in pavements, and that oxidation and subsequent hardening of asphalt binder has a profound effect on pavement durability, important implementation issues remain to be understood better. Quantitative assessment of asphalt binder oxidation for a given pavement is a very important but complex issue.

In this dissertation, a fundamentals-based oxygen transport and reaction model was developed to assess quantitative asphalt binder oxidation in pavements. In this model, oxygen transport and reaction were described mathematically as two interlinked steps: 1) diffusion and/or flow of oxygen from the atmosphere above the pavement into the interconnected air voids in the pavement; and 2) diffusion of oxygen from those air voids into the adjoining asphalt-aggregate matrix where it reacts with the asphalt binder.

Because such a model calculation depends extensively on accurately representing pavement temperature, understanding oxygen diffusivity in asphalt binders and mastics, and characterizing air voids in pavements, these key model elements were studied in turn. Hourly pavement temperatures were calculated with an improved one-dimensional heat transfer model, coupled with methods to obtain model-required climate data from available databases and optimization of site-specific pavement parameters nationwide; oxygen diffusivity in binders was determined based on laboratory oxidation experiments

in binder films of known reaction kinetics by comparing the oxidation rates at the binder surface and at a solid-binder interface at the film depth. The effect of aggregate filler on oxygen diffusivity also was quantified, and air voids in pavements were characterized using X-ray computed tomography (X-ray CT) and image processing techniques. From these imaging techniques, three pavement air void properties, radius of each air void (r), number of air voids (N), and average shell distance between two air voids (r_{NFB}) were obtained to use as model inputs in the asphalt binder oxidation model.

Then, by incorporating these model element improvements into the oxygen transport and reaction model, asphalt binder oxidation rates for a number of Texas and Minnesota pavements were calculated. In parallel, field oxidation rates were measured for these corresponding pavement sites and compared to the model calculations. In general, there was a close match between the model calculations and field measurements, suggesting that the model captures the most critical elements that affect asphalt binder oxidation in pavements.

This model will be used to estimate the rate of asphalt binder oxidation in pavements as a first step to predicting pavement performance, and, ultimately to improve pavement design protocols and pavement maintenance scheduling.

DEDICATION

I would like to dedicate all of my Ph.D. work and this dissertation to my wife, Yanyan Ji, my son, Ryan Han, as well as my parents for their love, encouragement, and support.

ACKNOWLEDGEMENTS

I am indebted to my research advisor, Dr. Charles J. Glover, for giving me the opportunity to study such an interesting project, and for his guidance, support, and encouragement throughout this research. I would also like to thank Dr. Amy Epps Martin, for her invaluable advice and comments that were tremendously helpful to my research and Dr. Mark Holtzapple, and Dr. Zhengdong Cheng for serving on my committee. It would not have been possible to achieve the goal of my research without the support that I received from all my colleagues, Nikornpon Prapaitrakul, Xin Jin, Yuanchen Cui, James J. Lawrence, Xue Lou, and Rong Lou, I thank all of them for the opportunity to share perspectives in research work and in life. All the support from these precious people made my study and achievement possible. I appreciate all of them from the deepest feelings of my heart.

NOMENCLATURE

$\widetilde{\alpha}$	Albedo
ε_a	Absorption Coefficient
E_a	Activation Energy
r_{CA}	Binder Oxidation Rate (Rate of Carbonyl Area Formation)
h_0	Dimensionless Henry's law constant
G'/(η'/G')	DSR Index
η'(ω)	Dynamic Shear Viscosity
ε	Emission Coefficient (Emissivity)
G'(ω)	Elastic (Storage) Dynamic Shear Modulus
A	Frequency (Pre-Exponential) Factor
R	Gas Constant
HS	Hardening Susceptibility
h_c	Heat Transfer Coefficient
m	Log-viscosity Intercept
η_o^*	Low Shear Limiting Viscosity
r_{O2}	Oxygen Consumption Rate
$\mathcal{D}_{O_2}$	Oxygen Diffusivity
POV	Oxygen Pressure Vessel

α	Oxygen Reaction Order
η_o	Original Viscosity
P	Pressure
PAV	Pavement Aging Vessel
k	Thermal Conductivity
η_t	Viscosity at Time t

TABLE OF CONTENTS

CHAPTER Page

CHAPTER Page

Page

LIST OF FIGURES

Page

Page

LIST OF TABLES

CHAPTER I
INTRODUCTION

Introduction

Today, there are more than 2 million miles of paved roads and highways in the United States. Among them, 94% are surfaced with asphalt pavements. Each year billions of dollars are spent in asphalt pavement construction and maintenance. With such a large expenditure, it is highly desirable that asphalt pavements last for a long time. However, even with appropriate design and construction initially, pavements fail within 10 to 20 years, with signs of fatigue cracking, thermal cracking, or other distresses.

One of the main contributing factors for long term asphalt pavement failure is the chemical and physical property changes of asphalt binder in pavements with oxidation. With oxidation, carbonyl (– C=O) groups are formed that increase the associations of polar species in asphalt binder, producing a more stiff, less ductile material.[1,2,3,4] A typical asphalt binder has a viscosity of 2000 poise at 60 ^{o}C before mixing at elevated temperatures and 4000 poise after hot-mixing, These materials can then harden further to several thousand poises over several years of oxidation while in service on the road. Hardening of the asphalt binder in pavements, while altering mixture properties, makes pavements less flexible and more susceptible to cracking due to repeated traffic loading and severe environmental conditions.[5,6] Thus, a good asphalt pavement design initially might not be a good design in terms of long-term performance. Designing pavements in to account for asphalt binder oxidation and achieve maximum pavement service life and better performance is an important issue. One essential component to this effort is to develop a deterministic model to quantitatively assess asphalt binder oxidation and hardening in a given pavement (over time and with pavement depth) with known asphalt binder and mixture properties, along with environmental conditions.

The dissertation follows the style of the *AIChE Journal*.

Asphalt concrete is a compacted heterogeneous composite material of aggregates (~95% by mass), asphalt binder (~5% by mass), and air voids; and is used as a layer in asphalt pavements. It features structurally a complex distribution of air voids in an asphalt binder-aggregate matrix. Recent studies reveal that the majority of air voids in the pavement are interconnected air channels, existing from the top to the bottom of the specimen.[7,8] Connectivity of air voids assures that ambient air diffuses and/or flows into air void channels in the pavements and provides an adequate availability of oxygen for diffusion into the surrounding asphalt binder-aggregate matrix and reaction with the asphalt binder.

The goal of this work is to develop a reliable heat and mass transport computational model based on pavement air void characterization for use in quantitatively assessing asphalt binder oxidation in pavements and predicting asphalt binder properties in pavements over time. This model will be used to estimate the rate of asphalt binder oxidation in pavements as a first step to predicting pavement performance, and ultimately, to improve pavement design protocols and pavement maintenance scheduling.

The research background for this dissertation is divided to cover the important elements necessary to develop a thermal and oxygen transport and reaction model. The first section reviews past development on pavement heat transfer fundamentals and pavement temperature modeling. The second section briefly describes asphalt binder oxidation chemistry and asphalt binder oxidation and hardening kinetics. The third section discusses pavement air void structural features, oxygen transport in pavements, and oxygen diffusivity in asphalt binder materials. The fourth section summarizes some recent work on pavement oxidation modeling. Based on this background information, research objectives and a dissertation outline are summarized in the last section.

Pavement Heat Transfer Fundamentals and Pavement Temperature Modeling

One of the key environmental factors that influence asphalt pavement design and performance is pavement temperature, which varies with location, time (daily and seasonally), and depth below the pavement surface. Accurate presentation of pavement temperature and temperature history are of extreme importance to predict pavement oxidation and hardening as oxidation and hardening rate of an asphalt binder follows the Arrhenius equation that states an exponential proportion between oxidation and hardening rates with the inverse of asphalt binder temperature.

Extensive research has been performed to obtain accurate pavement temperatures. Fundamental early models of heat transfer in pavements included shortwave solar radiation, down-welling and upwelling long-wave radiation, convective heat transfer at the pavement surface, and heat conduction inside the pavement,[9,10,11] as summarized in Figure I–1. There are multiple sources of heat transfer at the pavement surface: solar radiation and reflection of the solar radiation at the surface by a fraction $\widetilde{\alpha}$, the albedo; absorption of atmospheric down–welling long–wave radiation by the pavement surface; emission by long–wave radiation to the atmosphere; and convective heat transfer between the pavement surface and the air close to the surface, which is enhanced by wind. Below the surface and within the pavement and ground beneath it, heat is transferred by conduction. Key model parameters used to adjust some component for different climate conditions are also shown in Figure I–1, including $\widetilde{\alpha}$, the fraction of reflected solar radiation albedo of the pavement surface; ε_a, the absorption coefficient of the pavement; ε, the emission coefficient (emissivity) of the pavement; h_c, the heat transfer coefficient that is a function of air temperature, pavement surface temperature, and wind speed; and k, thermal conductivity of the specific asphalt concrete.

Following these endeavors, the enhanced integrated climate model (EICM), a one–dimensional coupled heat and moisture simulation model based on these fundamentals was developed and later integrated into the current mechanistic-empirical pavement design guide (MEPDG) to couple pavement design with modeled pavement

temperature.[12] The EICM model uses a finite–difference approximation for calculating heat conduction within the pavement and underlying layers, subject to heat fluxes at the surface (shortwave solar radiation, long-wave radiation, and convective heat transfer) and a constant-temperature boundary condition well below the pavement surface. Using required climatic input data including solar radiation, ambient temperature, and wind speed and constant model parameters such as pavement albedo, pavement emissivity, and thermal diffusivity, the model is solved numerically for temperature over time and depth.

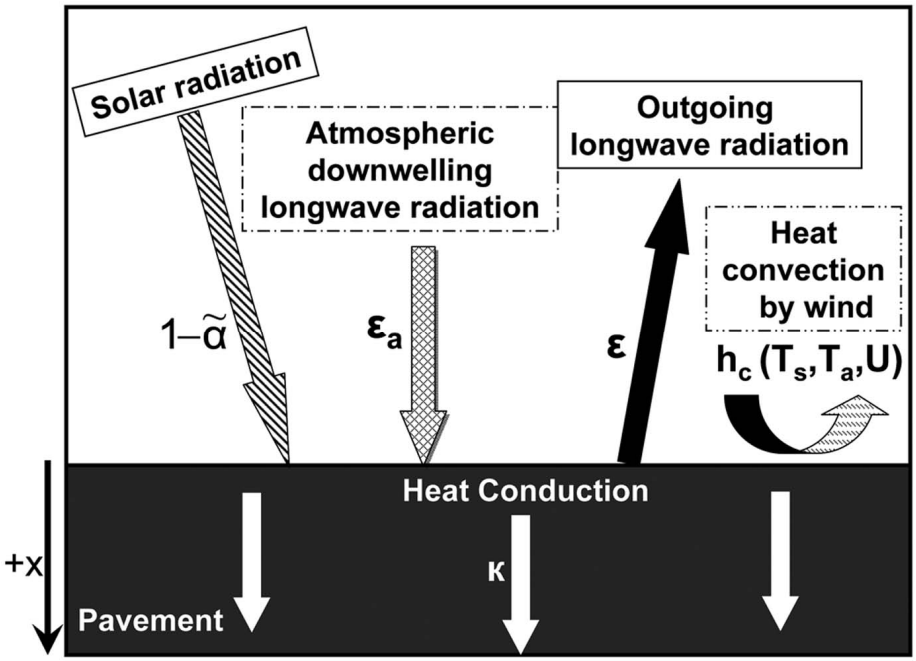

Figure I–1. Schematic Representation of Heat Transfer Model of Pavement

Although temperatures predicted with the EICM model satisfy pavement design needs in general, there have been some large errors when compared to measured pavement temperature. In one study of Ohio pavements, differences as high as 20 ^{o}C were observed in the top 10 inches (0.25 m) of pavement and there was an average

difference of 10 ^{o}C at 30 inches (0.75 m) depth.[13] Similar results are seen in the studies on New Jersey pavements for which an average difference of 15 ^{o}C over the top 20 inches was calculated from reported data.[14] These errors are most likely caused by several factors: the assumption that heat fluxes at the pavement surface are exactly balanced by conduction into the ground well below the surface, inaccuracy of climatic input data (especially calculated solar radiation) due to imperfect data interpolation schemes, the assumptions of the constant-temperature boundary condition, and site-independent pavement-related model parameter values. As reported by other studies, model parameters such as pavement albedo are not constant, but depend on region and season dependent.[15,16]

Recently, significant improvement in accuracy over the EICM model has been achieved by several groups using a similar one-dimensional heat transfer model, but with an unsteady-state surface heat flux boundary condition, measured model input data, and site-specific model parameters that were optimized based on measured pavement temperatures.[15,16,17] Most of this work focused primarily on determining yearly maximum and minimum pavement temperatures for the purpose of asphalt binder selection. Recent efforts for more detailed modeling have been restricted to short time scales and to a specific pavement site, because of the general lack of accurate hourly climatic input data and an understanding of how site-specific pavement parameters vary with location.

Asphalt Binder Oxidation Chemistry and Kinetics

Past developments have addressed a number of important questions concerning asphalt binder oxidation including: What is asphalt binder oxidation? How fast does it occur? What is the impact of oxidation on asphalt binder physical properties?

Oxidation Chemistry

When exposed to oxygen, asphalt binder forms carbonyl (–C=O) compounds by oxidizing aromatic compounds in the naphthene aromatic, polar aromatic, and asphaltene fractions resulting in an increase in carbonyl content and asphaltene fraction.[4,18,19] Although the exact nature of the carbonyl compounds and the formation rates may vary from asphalt binder to asphalt binder, the common factor is that for asphalt binders the carbonyl content can be used as a surrogate for total oxidative changes. Carbonyl content (CA) is measured as the area under the Fourier Transform Infrared Spectroscopy (FTIR) absorption band from 1650 to 1820 cm^{-1}.

The formation of asphaltene leads to asphalt binder hardening. The binder hardening rate can be expressed as follows:[3,20,21]

$$r_\eta = \frac{\partial \ln \eta}{\partial t} = \frac{\partial \ln \eta}{\partial AS} \cdot \frac{\partial AS}{\partial \mathrm{CA}} \cdot \frac{\partial \mathrm{CA}}{\partial t} \qquad \text{(I–1)}$$

Three terms in Equation I–1 are important characteristics of asphalt binder that depend on its chemical composition. $\partial \ln \eta / \partial AS$ is the effect of asphaltene (AS) increase on increasing viscosity and is affected by asphaltene size. $\partial AS / \partial \mathrm{CA}$ is the asphaltene formation susceptibility (AFS) that is a measure of the capacity of the maltene to produce new asphaltenes with aging. $\partial \mathrm{CA} / \partial t$ is the rate of carbonyl area (CA) formation, also called binder oxidation rate.

Oxidation Kinetics

The carbonyl reaction is characterized by an initial rapid rate period (A) that declines over time until a constant rate period (B) is reached, as demonstrated in Figure I–2. Although the reaction mechanisms are still not fully understood, the reaction–rate

for the constant–rate period can generally be described using an Arrhenius expression for temperature variation and pressure dependence:[1,2]

$$\frac{dCA}{dt} = r_{CA} = AP^{\alpha} e^{-E/RT} \qquad \text{(I–2)}$$

where A is the frequency (pre-exponential) factor, P is the pressure, α is the reaction order with respect to oxygen pressure, E is the activation energy, R is the gas constant, and T is the absolute temperature. Values of A, E, and α depend on asphalt binder, although A and E are generally correlated.

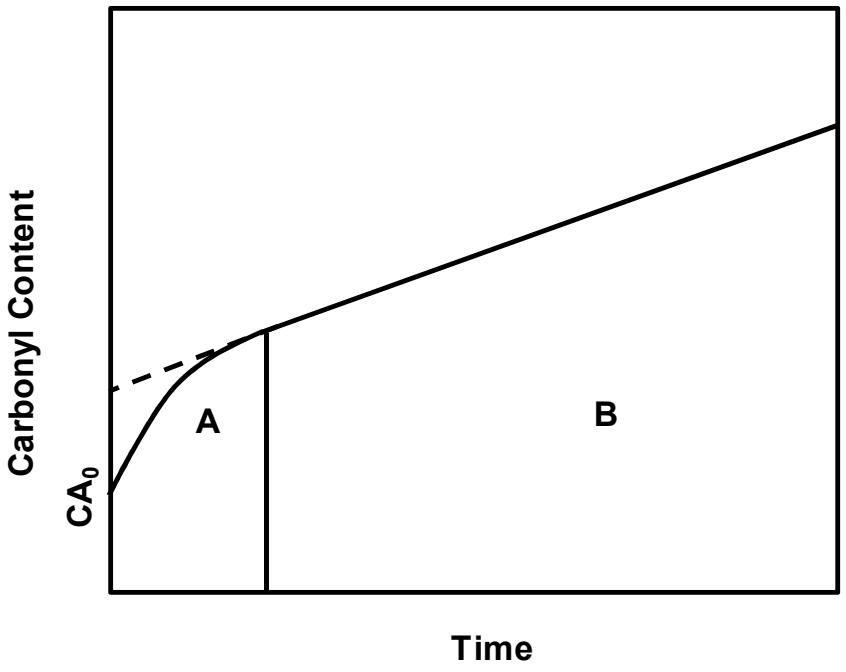

Figure I-2. Typical CA Growth of an Asphalt Binder to Oxidation

Effects of Oxidation on Asphalt Binder Physical Properties

Carbonyl formation leads to stronger associations between asphalt binder polar components and results in an increase of asphaltene fraction and a stiffer asphalt binder in both its elastic modulus and viscosity. Quantitatively, carbonyl growth correlates linearly with changes in rheological properties, such as log (low shear limiting viscosity) or DSR index ($G'/(\eta'/G')$)[4,22,23] measured at 44.7 ^{o}C and 10 rad/s. Here, low shear limiting viscosity is a measurement of rheological properties of asphalt binder when it is not disturbed by external forces. The DSR index is a rheological complex function measured with the Dynamic Shear Rheomter (DSR); and it consists of two measured visco-elastic properties, G'(storage modulus) and η' (dynamic viscosity).

Figure I–3 shows an example of the correlation between low shear limiting viscosity and carbonyl growth for several asphalt binders.

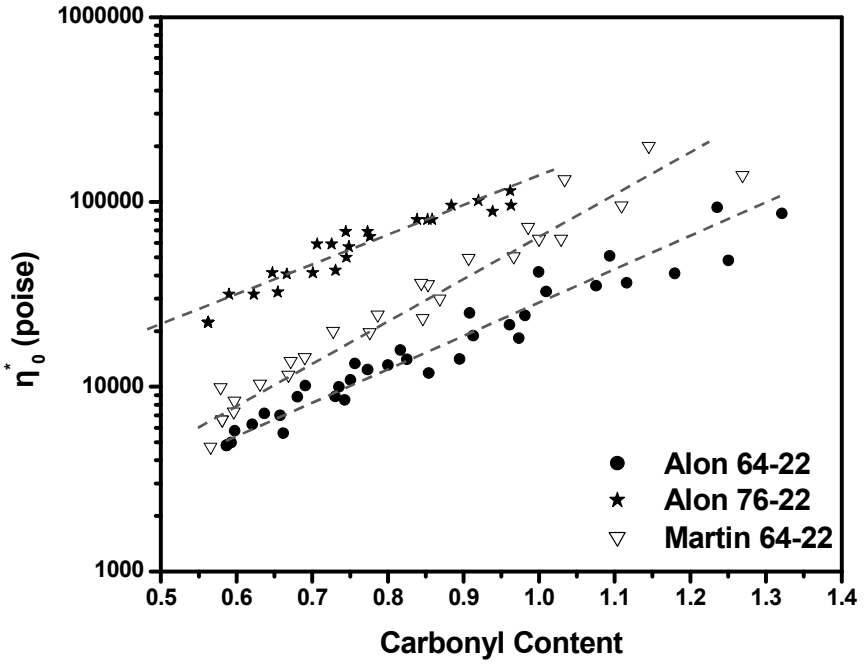

Figure I–3 Correlation between Low Shear Limiting Viscosity and Carbonyl Growth for Several Asphalt Binders

The mathematical expression for this physicochemical relationship that governs binder rheology with oxidation is:[22,23]

$$\eta_0^{*} = \exp(HS * CA + m) \tag{I–3}$$

where, *HS* is hardening susceptibility. This relationship is asphalt binder dependent and reflects the change in log-viscosity with respect to the change in carbonyl content, and *m* is the log-viscosity intercept.

HS and *m* are determined from experimental data and are asphalt binder dependent and functions of absolute temperature according to Equations I–4 and I–5:[24]

$$HS(T) = HS(T_0) + \gamma\left(\frac{1}{T} - \frac{1}{T_0}\right) \tag{I–4}$$

$$m(T) = m(T_0) + \delta\left(\frac{1}{T} - \frac{1}{T_0}\right) \tag{I–5}$$

where, γ and δ are determined from viscosity activation energy. An average value of 1656 K/CA for γ and 20,360 K for δ were reported based on measurements on a number of asphalt binders.

The hardening susceptibility can be multiplied by the oxidation reaction rate to obtain the hardening rate after the initial jump period has been passed, with the reaction rate constant at a fixed temperature. With oxidation and hardening kinetics known for an asphalt binder along with environmental conditions (pressure and temperature) specified, asphalt binder hardening rates can be calculated over time using Equation I–6.[1,20,21]

$$\ln \eta_t = \ln \eta_{ot} + \Delta\left(\ln \eta_j\right)[P] + r_{CA}[T,P] \cdot HS[P](\text{time}) \tag{I–6}$$

where, [*T, P*] or [*P*] indicates that the property is a function of temperature and pressure or only pressure, respectively. Here, η_t is the viscosity at any time, $\ln\eta_{ot}$ is the initial viscosity of the asphalt binder after the hot-mix asphalt plant simulated by oven aging of loose asphalt concrete, $\Delta\left(\ln\eta_j\right)$ is the hardening that occurs in the early rapid initial jump stage.

Although the physicochemical relationships discussed are expressed in terms of zero-shear limiting viscosity, the DSR index that is measured at 44.7 ^{o}C and 10 rad/s follows the similar trends.[25,26] The importance of using the DSR index is that it not only correlates with carbonyl growth with oxidation, but also relates to asphalt binder ductility very well. It has been shown that binder ductility correlates very well with DSR index G'/(η'/G') in the ductility range from 2 cm to 10 cm.[26] Asphalt binders harden and become more brittle with oxidation, which decreases the performance in terms of flexibility over time and eventually destroys the pavement. Asphalt binder ductility has been used as an important measurement of asphalt binder brittleness. It has been reported that ductility values in the range of 2 to 3 cm for 15 °C at 1 cm/min appear to correspond to a critical level for age-related cracking.[27] From this perspective, embrittlement of asphalt binders with oxidation can be tracked with measurement of the binder DSR index that correlate with binder ductility (measured at 15 °C, 1 cm/min). Such correlation can be represented on a map of G' versus (η'/G'), which traces an asphalt binder as it ages.[26] On this map, as the binder ages over time, it moves from the lower right to the upper left as the result of the increase in elastic stiffness and viscosity.

Oxygen Availability in Pavements

Given an adequate supply of oxygen, asphalt binders in pavements will harden and become brittle.[6] Over time, as their ductility decreases pavement cracking increases.[7, 28,29,30,31,32,33] A key question is how quickly oxygen can be supplied to the asphalt binder in the pavement to feed the reaction. The answer to this question lies in

the distribution of pores through the asphalt concrete mixture to allow air into the pavement, plus the oxygen diffusivity in the binder.

Pavement Permeability and Air Void Structure

Conventionally, it was believed that pavements are not that permeable, and that air can only penetrate into a very thin surface layer of the asphalt pavement (top 1.5 inches).[34] Although direct measurement of pavement permeability to air is extremely difficult, measurement of air void properties such as interconnected air void content (or accessible air void content) can serve as a surrogate. This property is determined by a number of weight measurements including the weight of the dry asphalt pavement core in air, the weight of the saturated pavement core underwater, and the weight of the dry pavement core underwater. Two methods were used to determine these weights, a saturated surface-dry (SSD) method [35] and the Corelok® method.[36,37] The Corelok® operating procedure can be found in the Corelok® Operator's Guide. Accessible air void contents have been determined for a number of pavement cores in several studies, ranging from 2% to 10% depending on mixture type,[6, 38] compaction effect, and other factors, which suggests that asphalt pavements might be more permeable than conventional thinking suggests.

Interior air voids structure in pavements has been recently studied using X-ray computed tomography (CT) and image analysis techniques. Using a connectivity algorithm with the computer software, it was found that the majority of air voids are interconnected air channels, existing from top to bottom of the specimen.[7,8,39] Connectivity of air voids assures that ambient air can diffuse and/or flow into the air void channels and provides a path for access to and diffusion and reaction within the adjoining asphalt binder. This idea is partly supported by the observation that for a large number of Texas pavements tested, the results indicate strongly that asphalt binders are oxidizing well below the pavement surface and that the hardening of asphalt binders is virtually unabated over time.[5,6]

From this perspective, oxygen transport and reaction in pavements can be described as two interlinked steps: 1) diffusion or flow of oxygen through interconnected air voids from the ambient atmosphere into the pavement; and 2) diffusion of oxygen from air voids into the adjoining asphalt binder-aggregate matrix and reaction. Both steps are a strong function of pavement temperature.

Oxygen Diffusivity in Asphalt Binders

To determine a quantitative estimate of oxygen concentration in pavements (in air voids and in the asphalt binder–aggregate matrix) where oxygen transport is limited by diffusion, knowledge of a key transport parameter, oxygen diffusivity, is crucial. Although diffusivity of oxygen in air is well understood, the literature is rather limited with regard to oxygen diffusion properties in asphalt binder materials, not to mention any quantitative model relating oxygen diffusivity in asphalt binder to asphalt binder material properties. Part of the difficulty in performing such experimental measurements is to separate oxygen transport from oxygen reaction with asphalt binder materials.

Lunsford[24] made an early attempt to estimate oxygen diffusivity and its dependency on asphalt binder viscosity using fundamental transport and reaction equations on 1 mm asphalt binder films. Diffusivity values of the order of 10^{-13} to 10^{-11} m^2/s were reported for several asphalt binders with temperature ranges from 60 to 80 ^oC. Although conceptually sound, his experiments were designed to determine kinetic parameters, not for accurate diffusivity measurement. The 1mm asphalt binder film was too thin to establish a sufficiently diffusion limited condition for accurate diffusivity measurement. Also, the assumption of a constant value of 1 for Henry's law constant led to additional error. Nevertheless, his serendipitous diffusivity measurement provided an important proof of concept for measuring diffusivity.

A further hindrance of oxygen diffusion in pavements is the presence of aggregates that are impervious to diffusion. Such aggregates impede the diffusion of oxygen into the asphalt binder and require that oxygen molecules take a more tortuous

path through the asphalt binder, thus lengthening the diffusion path and thereby effectively reducing the oxygen diffusivity. Measurements of the diffusivity of oxygen in mastics (asphalt binder and fine aggregates) will be needed in order to quantify this effect. The effect of volume fraction of inclusions on transport behavior in heterogeneous materials has been well understood for many years. Theoretically, with a known volume fraction of fines for a given mixture design, oxygen diffusivity in mastics can be estimated from well-established conventional prediction models (Maxwell, Rayleigh, or Non-spherical complex models).[40]

Recent Efforts on Pavement Oxidation and Modeling

Incorporation of an asphalt binder oxidation model in pavement design has been a subject of interest for years, but researchers may have been mislead by an early report by Coons and Wright[34] that asphalt binder oxidation occurs only in the top 1.5 inch (3.75 cm) of the pavement and that below the top inch, the asphalt binder is left virtually unaffected by years of use and years of environmental exposure. This conclusion is formalized in a recently developed mechanistic empirical pavement design guide (MEPDG)[41] that assumes in its calculation that binders oxidize only in the top inch.

Recent evidence contradicts this early report with measured asphalt oxidation in a large number of pavements as a function of time and depths in pavements. It indicates that asphalt binders are oxidizing in pavements, and that oxidation is an ongoing process throughout a pavement's service life and through the entire depth of the pavement.[5, 6] In addition, the effect of asphalt binder oxidation in pavements can be very negative as far as pavement durability is concerned. With asphalt binder oxidation and subsequent hardening, pavements become less flexible and more susceptible to cracking under repeated traffic loading and severe environmental conditions. Although the mechanism of this fatigue life decline with oxidation is not yet well understood, it is believed to be an important phenomenon, and governed by fundamental material properties.

An extensive set of data on asphalt binder oxidation in pavements has been reported in Glover et al,[6, 25] in which a number of Texas and Minnesota pavements were cored, the binder extracted and recovered, and tested to determine asphalt binder rheological properties as a function of time and depths in pavements. By comparing oxidation rates in Texas and Minnesota, it was concluded that oxidation rate is largely determined by the temperature as a function of time and position (depth) in the pavement, provided the accessible air voids are sufficiently high (4 % or greater). When the accessible air voids in pavements are sufficiently low (2 % or less), the oxidation rate of binders in Texas pavements is significantly reduced. Not included in the study is the difference in asphalt binder oxidation and hardening kinetics among these tested pavement sites, which, in fact, is the primary factor that accounts for these measured differences in field oxidation rates. Although this recent study provides insight on key elements that influence asphalt binder oxidation in the field, the data are not detailed enough to be the basis for a quantitative deterministic model of binder oxidation in pavements, a model that is needed in order to incorporate asphalt binder oxidation into pavement design.

Prapaitrakul et al. recently made the first attempt to calculate asphalt binder oxidation in pavements with an oxygen transport and reaction model.[42,43] Based on the observation that air void channels in pavements are positioned and connected from top to bottom, a diffusion and reaction model was formulated that accounts for oxygen diffusion and reaction in the surrounding cylindrical shell of an air void channel. This model assumes a constant oxygen pressure (0.2 atm) in all air voids, a mono-disperse air void distribution at each pavement layer, and the same air voids content from pavement layer to layer. Two air void properties, average air void radius (r_{PS}) and the average half-distance between two adjacent pores (r_{NFB}) were calculated using image analysis methods and used to define a cylindrical shell matrix through which oxygen diffuses and reacts. Oxidation rates in this asphalt binder-aggregate matrix were calculated by modeling oxygen diffusion and reaction in the matrix with known asphalt binder

oxidation kinetics, an estimated value for oxygen diffusivity, and an estimated tortuosity factor to account for the presence of aggregate in the diffusion path.

This model, although encouraging, can be further improved with: 1) understanding or modeling oxygen concentration in the air voids, instead of assuming a constant oxygen pressure in all air voids (0.2 atm); 2) more realistic characterization of the air void structure in a pavement with an air void size distribution and a layer–by – layer air void structure difference; 3) better understanding of oxygen diffusivity in asphalt binders and mastics; and 4) accurate prediction of hourly pavement temperatures.

Objectives

The goal of this dissertation is to develop a reliable deterministic heat and mass transport computational model to predict asphalt binder oxidation in pavements. Such a model will be used to assess asphalt binder properties in pavements over time, to study the effect of asphalt binder oxidation on pavement performance, and ultimately, to improve pavement design protocols and pavement maintenance scheduling.

Oxygen transport and reaction in pavements occurs as two interlinked steps: 1) diffusion or flow of oxygen through interconnected air voids from the ambient atmosphere into the pavement; and 2): diffusion of oxygen from air voids inside the adjoining asphalt binder-aggregate matrix and reaction with asphalt binder. Both steps are a strong function of pavement temperature.

Based on the conceptual oxygen transport and reaction process discussed previously, mathematical models to describe the process were developed. Figure I-4 illustrates the key elements for this modeling effort.

The model uses fundamental input including asphalt binder oxidation and hardening parameters (measured in the laboratory), pavement temperature (as a function of time and depth), oxygen diffusivity in asphalt binder and in the asphalt binder-aggregate matrix, pavement air void parameters, and pavement asphalt concrete mixture properties. With these inputs, asphalt binder oxidation rates and hardening levels in

pavements will be calculated and then validated with field measurements. The main tasks for this modeling effort will serve as a separate chapter of this dissertation.

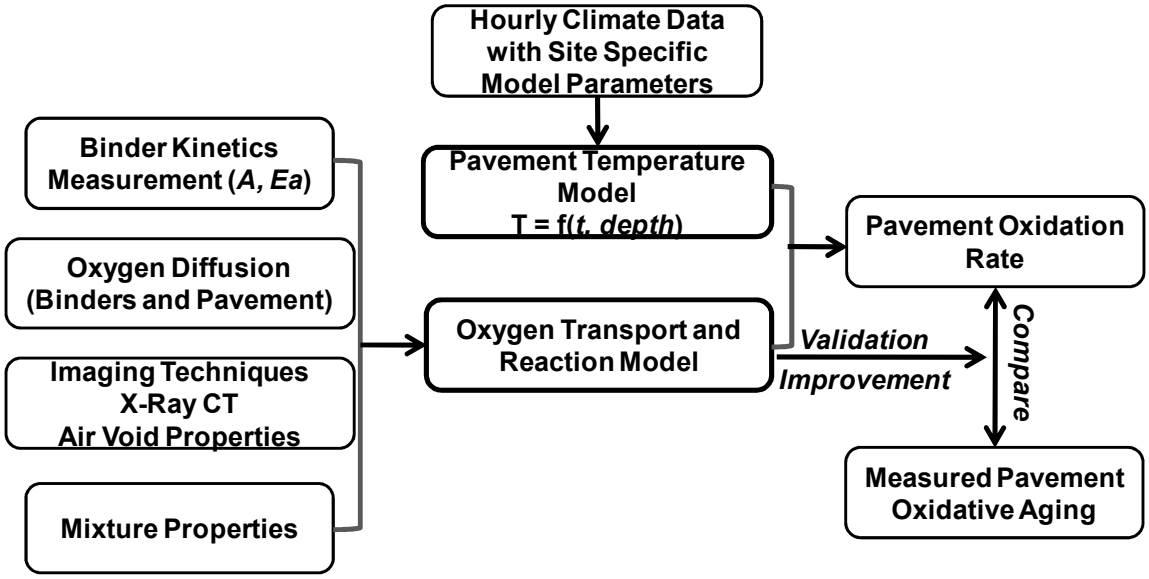

Figure I-4. Schematic Layout of Necessary Components of Pavement Oxidation Model

Pavement temperature modeling as a function of time and depth below the pavement surface is address in Chapter II. Pavement temperature varies with location (climate), time (day and season), and depth below the pavement surface. Accurate representation of pavement temperature is essential for calculating and modeling pavement oxidation because both oxygen transport processes and reaction rates in pavements are highly temperature sensitive.

Oxygen diffusivity in asphalt binder and asphalt binder-aggregate mixtures is presented in Chapter III. To get a quantitative evaluation of oxygen concentration in pavements where oxygen diffusion is limited, knowledge of the key transport parameter, oxygen diffusivity, is crucial. A further hindrance of oxygen diffusion in the asphalt binder-aggregate matrix is the presence of aggregates that are impervious to diffusion.

Measurements of the diffusivity of oxygen in mastics (asphalt binder and fine aggregate) were needed in order to quantify this effect.

Mathematical modeling of oxygen transport and reaction in pavements with improved pavement air void characterization is addressed in Chapter IV. A more realistic computational oxygen transport and reaction model was developed with more realistic representation of actual pavement air void structures to model transport through the air voids, transport within the asphalt binder-aggregate matrix, and to use these elements to calculate a layer-by-layer bulk asphalt binder oxidation rate and total asphalt binder oxidation rate. Both model development and air void characterization are discussed.

Model calculations and validation are presented in Chapter V. Oxidation rates for a number of Texas and Minnesota pavements were measured, and used to validate and further improve the model. In addition, the effect of pavement temperature, air voids properties, and binder oxidation kinetics on field oxidation rates are discussed by comparing field oxidation rates at these selected pavement sites.

CHAPTER II
PAVEMENT TEMPERATURE MODELING

Introduction

Pavement temperature varies with location, time (daily and seasonally), and depth below the pavement surface. Because asphalt binder oxidation rates follow the Arrhenius equation that states an exponential proportion between the oxidation rates and the inverse of asphalt binder temperature,[1] the ability to accurately predict pavement temperature is critical to model asphalt binder oxidation in pavements. In addition, universal model that can predict pavement temperature for any given pavement site is more favorable for implementation concerns.

Fundamental source components of heat transfer in pavements have been identified and summarized in Chapter 1. These include shortwave solar radiation, down-welling and upwelling long-wave radiation, convective heat transfer at the pavement surface, and heat conduction inside the pavement.[9, 10, 11] Previous modeling efforts based on these heat transfer fundamental components, though encouraging, did not completely succeed because of either large prediction errors generated by flawed model concepts (EICM model) or lack of accurate hourly climate input data and an understanding of how site specific model parameters vary with locations (more recent improved models).[12, 13, 14, 15, 16, 17]

In this work, a generally applicable one-dimensional model, coupled with methods to obtain model-required climate data from available databases and optimization of site-specific pavement parameters, was developed to calculate hourly pavement temperatures nationwide at a function of depth over yearly time scales. The model would be useful for various applications, but especially for calculations of binder oxidation in pavements, as it changes hour-by-hour and depth according to temperature.

Materials and Methodology

Overview of Experimental Design

A one-dimensional heat transfer model that employs an unsteady-state heat flux boundary condition at the pavement surface, a depth-independent heat flux 3 m below the surface, and the ability to estimate site-specific model parameters using known measured pavement temperatures was firstly developed. Then, a general method to obtain or impute (if needed) climatic data (solar radiation, ambient temperature, and wind speed) in an hourly format was adapted. With these input data and model, key model parameters such as pavement albedo, pavement emissivity, and absorption coefficients at 29 pavement sites (where measured pavement temperature were available) across the United States were estimated. The effects of climate pattern and site-specific conditions on these model parameters were further evaluated, and interpolation strategies were determined. The ability of the model, combined with imputed climate data and interpolated model parameters, to predict pavement temperature was then evaluated. Ultimately, this model aims to provide a general tool to obtain accurate hourly pavement temperatures (as a function of time and depth) at any desired pavement site for various applications, but especially for calculations of asphalt binder oxidation in pavements.

Pavement Sites Studied

Twenty-nine widely distributed pavement sites across the United States, where one to three months of measured continuous hourly pavement temperatures were available, were selected in this study. Measured pavement temperatures for those 29 sites were collected from the Long–Term Pavement Performance (LTPP) database. Distribution of these 29 pavement sites is shown in Figure II-1. Among those sites, two distinct LTPP sites are extremely valuable, Pavement 48-1068 in Lamar, Texas, and

Pavement 27-1028 in Otter Tail, Minnesota. These two sites are among the very few with hourly temperature data for an entire year, and as a function of depth.

Model Development

The one-dimensional model, similar to that of Gui et al., was developed based on radiation and conduction energy balance fundamentals.[17] The heat transfer process is depicted schematically in Figure II-1. There are multiple sources of heat transfer at the pavement surface: solar radiation and reflection of the solar radiation at the surface by a fraction $\tilde{\alpha}$, the albedo; absorption of atmospheric down-welling long-wave radiation by the pavement surface; emission by long-wave radiation to the atmosphere; and convective heat transfer between the pavement surface and the air close to the surface, which is enhanced by wind. Below the surface and within the pavement and ground beneath it, heat is transferred by conduction. Not included in this model is heat transfer enhancement by precipitation or the effect of moisture freeze and thaw in the pavement. Mathematical details of this model follow.

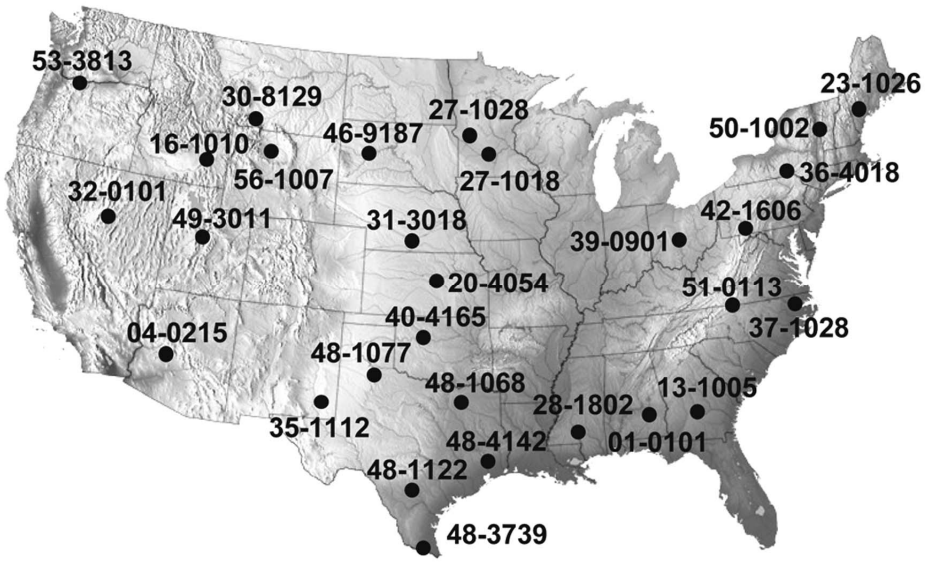

Figure II-1. Distribution Map of 29 SMP Pavement Sites Studied

Heat Transfer in Pavements

Heat transfer in the pavement is governed by the classical thermal diffusion equation:

$$\frac{\partial T}{\partial t} = \kappa \frac{\partial^2 T}{\partial x^2} \tag{II-1}$$

where, T is the pavement temperature as a function of time (t) and depth below the surface (x), and κ is the thermal diffusivity, $\kappa = k / \rho C$ where k is the thermal conductivity, ρ is the density, and C is the pavement heat capacity.

Surface Boundary Condition

For the surface boundary condition, considering a differential element of the pavement surface, its thermal energy (temperature) will change to the extent the fluxes from above and from below do not balance. The various fluxes shown in Figure I-1 led to the following surface condition:

$$\rho C \frac{\Delta x}{2} \frac{\partial T_s}{\partial t} = Q_s - \tilde{\alpha} \cdot Q_s + Q_a - Q_r - Q_c - Q_f \tag{II-2}$$

Where, ρC is the volumetric heat capacity of the pavement; T_s is the pavement surface temperature; x is the depth below the pavement surface; $\frac{\Delta x}{2}$ is the (differential) pavement thickness for the energy balance; Q_s is the heat flux due to solar radiation; $\tilde{\alpha}$ is the albedo of the pavement surface (the fraction of reflected solar radiation); Q_a is the down-welling long-wave radiation heat flux from the atmosphere; Q_r is the outgoing

long-wave radiation heat flux from the pavement surface; Q_c is the convective heat flux between the surface and the air**;** Q_f is the conduction from surface into the pavement.

The incoming and outgoing long-wave radiations are calculated by:

$$Q_a = \varepsilon_a \sigma T_a^4 \tag{II-3}$$

$$Q_r = \varepsilon \sigma T_s^4 \tag{II-4}$$

where, ε_a is the absorption coefficient of pavement; ε is the emission coefficient (emissivity) of pavement; T_s is the pavement surface temperature, K; T_a is the air temperature, $\sigma = 5.68 \times 10^{-8}\,\mathrm{W \cdot m^{-2} K^{-4}}$ is the Stefan-Boltzman constant.

The convective heat flux is calculated as:

$$Q_c = h_c (T_s - T_a) \tag{II-5}$$

where, h_c is the heat transfer coefficient ($W/m^2 \cdot K$) from the empirical equation:[12]

$$h_c = 698.24 \cdot a \cdot \left[0.00144 \left(\mathrm{abs}\left(\frac{T_s + T_a}{2} \right) \right)^{0.3} U^d + 0.00097(\mathrm{abs}(T_s - T_a))^{0.3} \right] \tag{II-6}$$

where, U is the hourly wind speed, m/s; a and d are two dimensionless empirical parameters

The heat flux within the pavement at the surface is expressed by Fourier's law:

$$Q_f = -k \left(\frac{\partial T}{\partial x} \right)\Bigg|_s \tag{II-7}$$

where $\left(\frac{\partial T}{\partial x}\right)\Big|_s$ is the temperature gradient at the pavement surface**,** and k is the thermal conductivity of asphalt concrete.

Combining these results, a thermal energy balance at the surface provides the surface boundary condition:

$$\rho C \frac{\Delta x}{2}\frac{\partial T_s}{\partial t} = Q_s - \tilde{\alpha}\cdot Q_s + \varepsilon_a \sigma T_a^4 - \varepsilon \sigma T_s^4 - h_c(T_s - T_a) + k\left(\frac{\partial T}{\partial x}\right)\Big|_s \qquad \text{(II-8)}$$

Bottom Boundary Condition

Commonly, a constant-temperature boundary condition, some distance below the surface, is reported in the literature. For example, Hermansson[15, 16] used the annual mean temperature 5 m below the surface as a bottom boundary condition. Gui et al.[17] used a measured temperature of 33.5 ^{o}C at a depth of 3 m as the boundary condition. In the EICM model, temperatures were measured from water wells across the country at a depth of 10 to 18 m, from which an isothermal map was constructed. Such a constant-temperature boundary condition has the advantage of simplicity, but the disadvantage is that these temperatures are not accurately known.

For the bottom boundary condition, from available measured pavement temperatures, it was observed that temperatures at a depth beyond 2 m tend to vary approximately linearly with depth. Using this result, the following bottom boundary condition was used at a depth of 3 m:

$$\left(\frac{\partial T}{\partial x}\right)\Big|_{3\text{m}} = \text{independent of depth} \qquad \text{(II-9)}$$

Such a boundary condition, which is based on field observation, has the advantage over the constant boundary condition in that it is location independent and does not require a specific value for the boundary condition. In addition, it is quite

straightforward to implement this boundary condition in the finite difference calculation procedure. Of course, this linear variation with depth condition is not strictly correct as extrapolating it to too great a depth will lead to significant error.

Model Structure and Calculation

The model employs climatic input data including hourly solar radiation, daily average wind speed, and imputed hourly air temperature. With known site-specific model parameters for given pavement sites, the model calculates temperature as a function of time and depth. The structure of the model is shown in Figure II-2. The model uses a finite difference approximation for calculating heat conduction within the pavement and underlying layers, subject to heat fluxes at the surface and a constant-flux boundary condition well below the pavement. In the numerical solution, the pavement thickness was divided into cells, which are thinner near the surface and thicker at deeper levels. Each cell is given a temperature (equal to air temperature) at the start of the calculation as an initial condition. The model then calculates a new transient temperature for each cell at each time step.

Acquisition of Climate Model Inputs

For any pavement site, model calculations require accurate hourly climatic data as input. Climatic input data for the model includes hourly solar radiation, hourly air temperature, and daily average wind speed data in an hourly format.

Solar radiation imputed empirically based on extraterrestrial incident radiation has been commonly used in most pavement temperature modeling efforts including the EICM model. Recently, several more advanced models have been developed to produce more accurate solar radiation data based on satellite images which are available from the National Solar Radiation Database (NSRDB). In this work, hourly solar radiation data

modeled using the SUNY model[44] or the METSTAT model[45], were used. Those data are generally available and cover nearly all parts of the United States from 1990 to 2005.

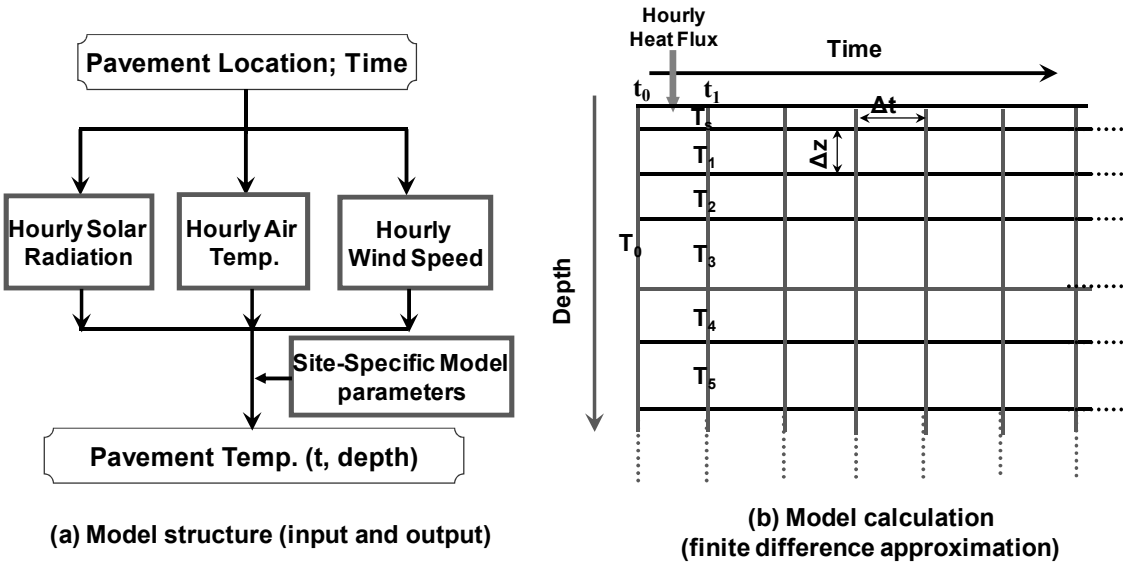

Figure II-2. Pavement Temperature Prediction Model: (a) Model Structure and (b) Model Calculation

Daily average wind speed can be directly collected from the Virtual Weather Station program in the Long–Term Pavement Performance (LTPP) database. Additionally, daily average wind speed can be obtained directly from the National Climatic Data Center (NCDC) or the meteorological network in each state. Although hourly wind speed is preferred, site-specific hourly wind speed data are difficult to obtain and highly dependent on unknown environmental conditions, making interpolation between locations problematic. Fortunately, the model is not overly sensitive to the wind speed, and daily average values are sufficient.

Hourly air temperature data are not commonly available in favor of daily maximum and minimum air temperatures, but reasonable estimates of hourly temperatures are needed for accurate temperature calculations. A conventional method to compute hourly air temperatures fits a sinusoidal function to the daily maximum and minimum air temperatures (EICM model). However, the daily profile of air temperature

is not exactly sinusoidal. Typically, the time for the air temperature to rise from the daily minimum temperature to the daily maximum temperature is about 9 hours, whereas 15 hours are taken for the air temperature to decrease from the daily maximum temperature to the daily minimum. To provide the model with accurate hourly air temperature data, a time-series analysis was employed.[46] Accordingly, an imputation method was developed to obtain a local hourly air temperature pattern from limited recorded hourly air temperature data. The pattern was then combined with commonly available recorded daily maximum, minimum, and average air temperatures to interpolate hourly air temperature data. Recorded daily maximum, minimum, and average air temperatures can be obtained easily from the Virtual Weather Station program in the LTPP database or NCDC.

Optimization of Site-specific Model Parameters

To obtain good model estimates of pavement temperatures, values of model parameters need to be determined for given pavement sites. Although some parameters are fairly well known (e.g. ρ, k, C,), others are site specific and require a parameter estimation process. Site–specific model parameters are albedo, emissivity, absorption coefficient, thermal diffusivity, and the parameters a and d in the heat convection coefficient correlation.

The sensitivity and importance of each parameter in the pavement temperature prediction model were assessed. Parameters were varied independently of one another over a range of values based on typical literature values. The temperature average absolute error (model calculation versus reported data) was used as a statistical measure of the model accuracy. This estimation method using average absolute error is preferred to, for example, the least-squares error by which a section with unusual properties receives more weight than a section with more typical properties. Then, parameter optimization was conducted for these model parameters at 29 pavement sites across the United States by comparing model estimates of pavement temperature to reported

measurements. Variation of these parameters with climate and pavement properties was also evaluated.

Results and Discussion

Sensitivities of Model Parameters

Model parameters were varied independently of one another over a range of values based on typical literature values. The temperature average absolute error (model calculation versus reported data) was used as a statistical measure of the model accuracy. The results are presented in Figure II-3 where the abscissa scale is different for each parameter with its values shown in the legend.

As shown in Figure II-3, when the albedo increased from 0.15 to 0.4, the average absolute error of the model prediction increased dramatically from about 1.5 to about 3.5 ^{o}C, implying an important role of the albedo in temperature prediction. Similarly, changing the emissivity (from 0.8 to 0.95) or the absorption coefficient (from 0.7 to 0.85) alone induced a significant variation in the model prediction accuracy. Interestingly, although individual changes in the emissivity or the absorption coefficient can significantly affect model accuracy, if both parameters are changed together while keeping the difference between them constant, there is very little effect on the model prediction. The value of thermal diffusivity (κ), *a,* and *d* are relatively less important in terms of their effect on model accuracy. Thus, constant values of these three parameters are suggested. Studies have suggested that different aggregates have slightly different thermal diffusivity, from 0.002–0.01 m^2/s based on reported values on several aggregate types.[47, 48] Reported thermal diffusivity of asphalt concrete, made from different aggregate sources, has a range from 0.0035 to 0.015 m^2/s based different measurement techniques.[48, 49] Based on optimization of thermal diffusivity of six pavement sites, a constant value of 0.005 cm^2/s was selected as a reasonable value for the thermal

diffusivity of the pavement. This value also agrees well with values recently reported by others.[49] For a and *d*, values of 1.4 and 0.5, respectively, were used.

Based on these results, accurate values for the albedo and the difference between the emissivity and absorption coefficients are important for obtaining a good temperature prediction for each pavement site. Additionally, a value of either the emissivity or the absorption coefficient is required. In the subsequent analysis, the absorption coefficient is used, recognizing that having its exact value is not critical.

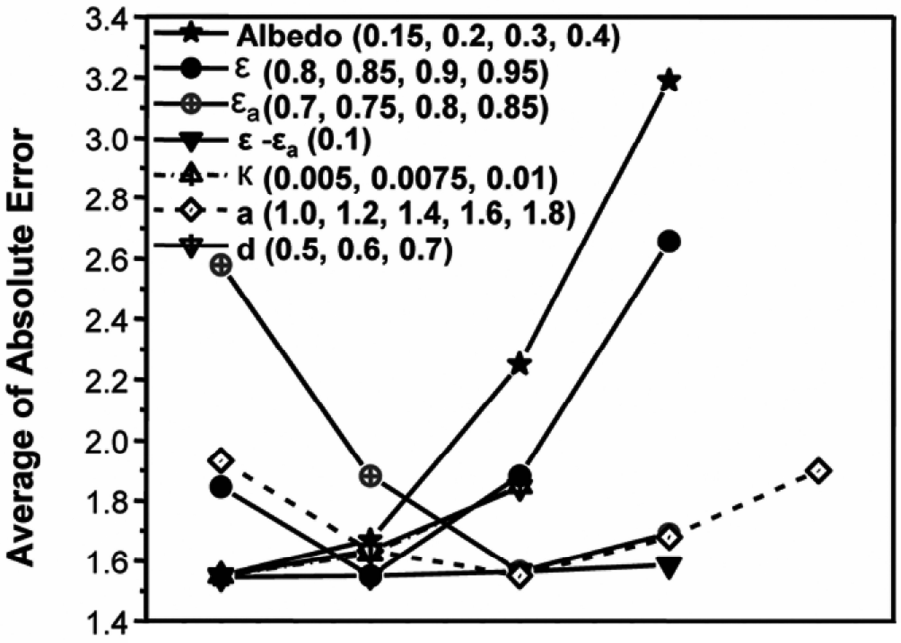

Figure II-3. Model Parameters Sensitivity Analysis: Effect of Changing Mode Parameters in Their Practical Ranges to Average of Absolute Error of Model Prediction

Optimization and Interpolation of Model Parameters

Although albedo, emissivity, and the absorption coefficient are site specific, there is no clear understanding of how these parameters vary with climate and pavement properties. To address this issue, parameter optimization was conducted for these model

parameters at 29 pavement sites across the United States by comparing model estimates of pavement temperature to reported measurements. Previous studies[16] suggested that albedo and emissivity values in the winter are different from their values the rest of the year. Therefore, in this work, two separate sets of model parameters were obtained, one set for the winter and one set for the other seasons (represented by summer). From further analysis of the distribution and seasonal variation of those model parameters, interpolation strategies have been developed for each model parameter and are presented subsequently.

The algorithm to find values of the three parameters identified by sensitivity analysis (albedo, difference between emissivity and absorption coefficient, and the absorption coefficient) is straightforward. Each parameter was given a range of values and increments within the range based on literature reports. By examining the ability of each set of model parameters to give the best match between the measured and the calculated pavement temperatures, the optimum set was obtained. Model parameters were optimized by examining the ability of each set of model parameters to minimize the average absolute error in temperature at the mid-depth of the asphalt concrete layer. Optimized values of these parameters are summarized in Table II-1; their distribution across the United States is discussed subsequently. The average absolute error between measured and calculated with optimized parameters are in general within 2 ^{o}C.

Albedo

Figure II-4 shows the distribution of the optimized albedo values across the United States. As seen in Figure II-4(a), the summer optimized albedo values for most of the pavement sites is constant at 0.2, with a slight variation from 0.2 to 0.15 in several pavement sites in Texas. In the winter (Figure II-4(b)), the optimal albedo values in the southern part of the country are the same as in the summer, while the albedo values in the north increased from 0.2 to from 0.3 to 0.35. Similar observations and conclusions have been reported in the literature.[16, 50]

Table II-1. Optimized Model Parameters of 29 Pavement Sites across the Country

LTPP SECTION	STATE	SUMMER				WINTER			
		$\widetilde{\alpha}$	ε	ε_a	ε-ε_a	$\widetilde{\alpha}$	ε	ε_a	ε-ε_a
01-0101	Alabama	0.2	0.85	0.75	0.1	0.2	0.85	0.75	0.1
04-0215	Arizona	0.2	0.9	0.7	0.2	0.2	0.85	0.7	0.15
13-1005	Georgia	0.2	0.85	0.75	0.1	0.2	0.85	0.75	0.1
16-1010	Idaho	0.2	0.85	0.7	0.15	0.35	0.85	0.7	0.15
20-4054	Kansas	0.2	0.85	0.7	0.15	0.2	0.85	0.7	0.15
23-1026	Maine	0.2	0.8	0.75	0.05	0.3	0.8	0.75	0.05
27-1018	Minnesota	0.2	0.8	0.75	0.05	0.3	0.8	0.75	0.05
27-1028	Minnesota	0.2	0.8	0.75	0.05	0.3	0.8	0.75	0.05
28-1802	Mississippi	0.2	0.85	0.75	0.1	0.2	0.8	0.75	0.05
30-8129	Montana	0.2	0.9	0.7	0.2	0.35	0.85	0.7	0.15
31-3018	Nebraska	0.2	0.85	0.7	0.15	0.3	0.85	0.7	0.15
32-0101	Nevada	0.2	0.85	0.7	0.15	0.2	0.85	0.7	0.15
35-1112	New Mexico	0.2	0.85	0.7	0.15	0.2	0.85	0.7	0.15
36-4018	New York	0.2	0.9	0.75	0.15	0.35	0.85	0.75	0.1
37-1028	North Carolina	0.2	0.8	0.75	0.05	0.2	0.8	0.75	0.05
39-0901	Ohio	0.2	0.8	0.75	0.05	0.3	0.8	0.75	0.05
40-4165	Oklahoma	0.2	0.8	0.7	0.1	0.2	0.8	0.7	0.1
42-1606	Pennsylvania	0.2	0.9	0.75	0.15	0.3	0.85	0.75	0.1
46-9187	South Dakota	0.2	0.9	0.7	0.2	0.35	0.9	0.7	0.2
48-1068	Texas	0.15	0.85	0.7	0.15	0.15	0.85	0.7	0.15
48-1077	Texas	0.2	0.85	0.7	0.15	0.2	0.85	0.7	0.15
48-1122	Texas	0.15	0.85	0.75	0.1	0.15	0.85	0.75	0.1
48-3739	Texas	0.15	0.85	0.75	0.1	0.15	0.85	0.75	0.1
48-4142	Texas	0.15	0.85	0.75	0.1	0.15	0.85	0.75	0.1
49-3011	Utah	0.2	0.9	0.7	0.2	0.35	0.85	0.7	0.15
50-1002	Vermont	0.2	0.8	0.75	0.05	0.35	0.8	0.75	0.05
51-0113	Virginia	0.2	0.8	0.75	0.05	0.2	0.8	0.75	0.05
53-3813	Washington	0.2	0.85	0.75	0.1	0.35	0.85	0.75	0.1
56-1007	Wyoming	0.2	0.9	0.7	0.2	0.35	0.85	0.7	0.15

Although the exact reason for the albedo increase in the winter in the north is not clear, it seems that changes to the pavement surface, associated with the snow coverage and freezing condition in the winter, likely is a key. This hypothesis is supported by comparing the optimized winter albedo values on a national snowfall or freezing condition distribution map, published at NCDC online and based on the average of recorded data from 1961 to 1990[51]. It seems that the seasonal albedo variation of pavements is more affected by the freeze state and snowfall, and less affected by other environmental factors and material properties of the pavement. To interpolate albedo values at other pavement sites, a reasonable approach is to separate the northern and southern parts of the United States according to the snowfall distribution map. As the albedo value in each region is quite stable in either the winter or summer, the value for the nearest pavement site in the same region, based on the 29 pavement sites studied, can be adopted as the albedo value for the specific pavement site. Alternatively, the albedos for the nearest three pavement sites in the same region can be averaged to obtain the albedo for the pavement of interest.

Because snowfall and freezing conditions vary with time, one question is how to determine winter versus non-winter periods. Ground albedo values have been recorded daily or monthly using satellite remote sensing techniques, commonly with a resolution of 10 km across the country. These observations support the conclusion that distinctly higher values of albedo occur during winter snow coverage and freezing conditions than during other periods. Satellite recorded albedo values, although not specifically for pavements, have been collected in several databases that can be easily accessed (such as NCDC or NSRDB). For any specific pavement site and year of interest, recorded albedo data from these databases at the nearest location can be extracted. The winter period suggested by high albedo values in those databases may then be used to define the winter period for pavement calculations.

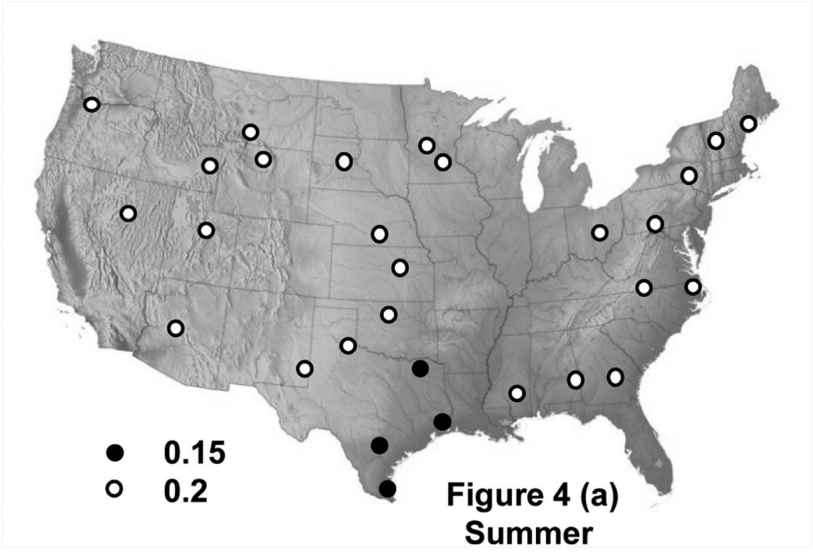

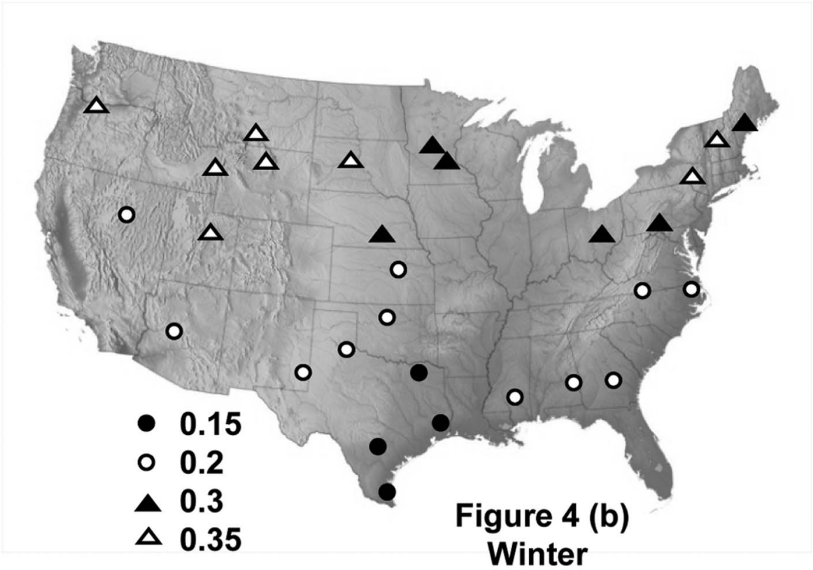

Figure II-4 Distribution of Optimized Albedo Values at: (a) Summer and (b) Winter

Algebraic Difference between Emissivity and Absorption Coefficient

The second important model parameter is the algebraic difference between the pavement emissivity and absorption coefficient. Figure II-5 shows the optimized values of the parameter for the 29 national pavement sites on a national terrain map in both winter (Figure II-5(a)) and summer (Figure II-5(b)). Four different values were obtained (0.05, 0.1, 0.15 and 0.2), but distribution patterns that follow climatic regions can be noted. Region A covers the northeast and east north central regions and generally experiences a humid climate with long winters. The optimized value for the algebraic difference in this region generally is 0.05. Region B, the southeast areas and part of the south is located in a mesothermal zone with humid sub-tropical climate. An optimized value of 0.1 is common for pavement sites in this region. Region D covers the western part of the United States, especially mountain regions and a dry, cold climate is dominant. Here a value of 0.2 was generally obtained in the winter while in the summer a value of 0.15 was obtained. Region C is a transition zone between Regions B and D, and a value of 0.15 was commonly obtained for both winter and summer. Despite several slight deviations, the optimized value for the algebraic difference in most of the pavement sites followed these general trends reasonably well.

Previous studies have suggested that the absorption coefficient is mainly affected by the water partial pressure in the air. A linear relationship between absorption coefficients with partial pressure in a clear sky have been further developed using linear regression techniques.[52] It also has been known that the long-wave emissivity of a pavement is mainly affected by the pavement surface property and environmental conditions.[50] From this perspective, it is not surprising to see that the optimized values of the algebraic difference between the emissivity and absorption coefficients varies from winter to summer at pavement sites in Region D, most likely due to climate effects. As emissivity also is affected by site-specific pavement surface properties, small deviations from the general trends of the climatic regions are reasonable.

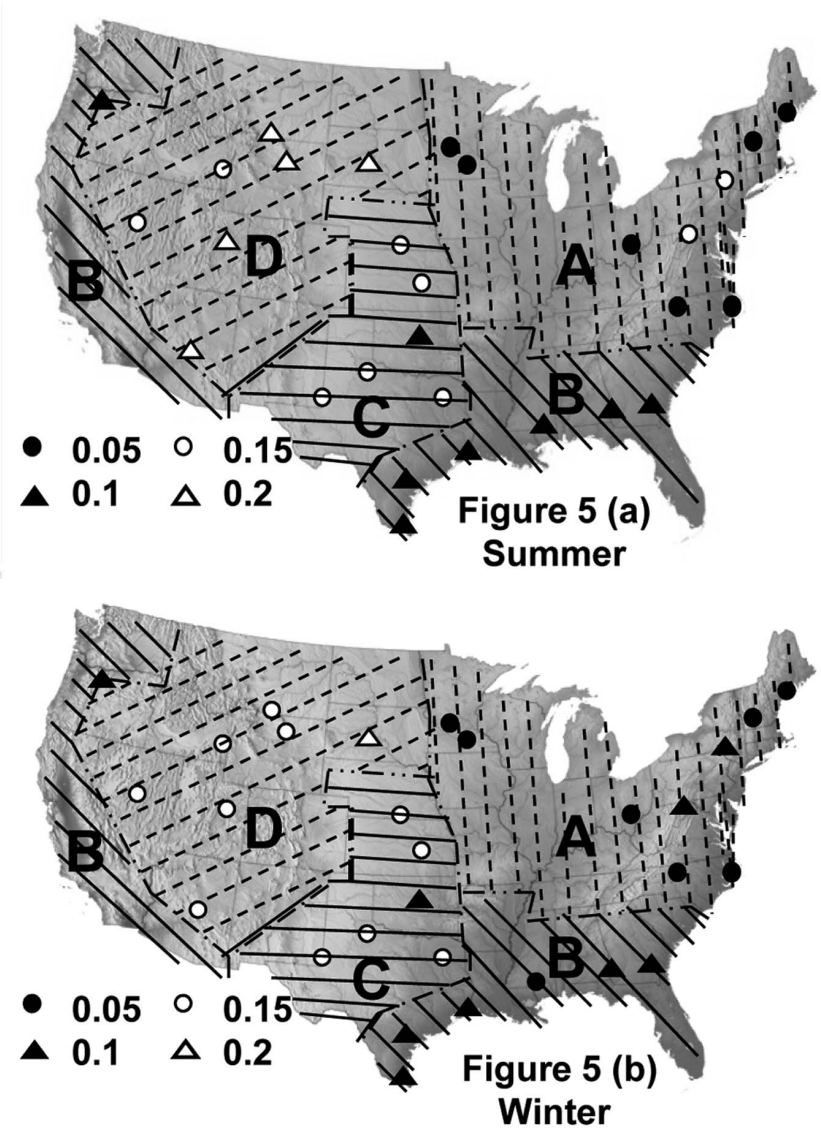

Figure II-5. Distribution of Optimized Values of the Algebraic Difference between Emissivity and Absorption Coefficient at: (a) Summer and (b) Winter

With a known pavement location, values of the difference between the emissivity and absorption coefficient for any pavement site in each region can be approximated based on the observed trends described. Alternatively, to consider possible deviations from the general trends caused by different pavement material properties, parameter values obtained from the nearest three pavement sites (of the 29 sites studied in this

work) and in the same climatic region, can be averaged to obtain a value for the specific pavement site.

Absorption Coefficient

The third important parameter is the absorption coefficient for down-welling long-wave radiation from the air. Figure II-6 shows the estimated value of the absorption coefficients for the 29 pavement sections. Two values of the absorption coefficient, 0.75 in the east and south (and northwest) coastal regions and 0.7 in the drier Midwest to west regions were observed. As the absorption coefficient is mainly affected by the water partial pressure in the air, optimized values match quite well with national relative humidity distribution based on average recorded data from 1961 to 1990.[53] The optimized values in both winter and summer are the same, indicating the parameter is less affected by seasonal variation.

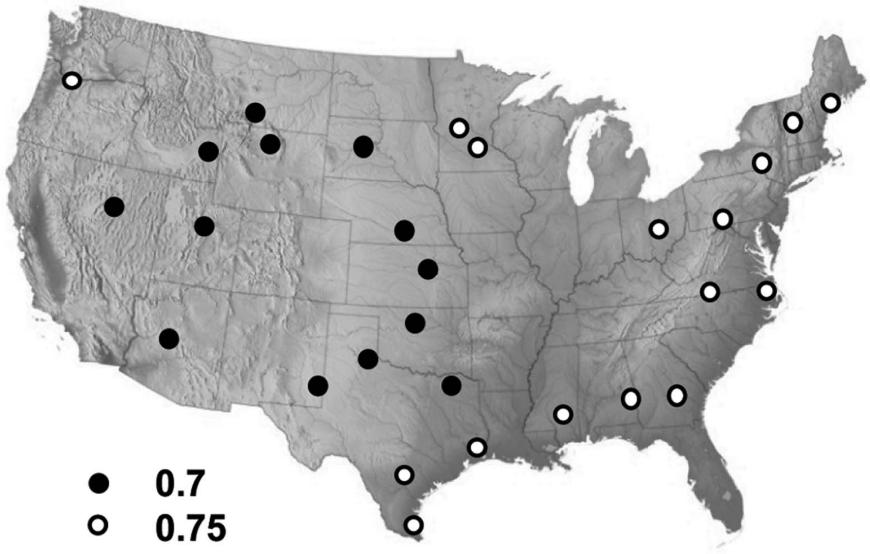

Figure II-6. Distribution of Optimized Values of Absorption Coefficient

So, based on the 29 pavement sites studied in this work, values of the absorption coefficient at other pavement sites can be interpolated from their values at the nearest pavement sites in the same humidity region, obtained from the national humidity map.

Model Validations

To demonstrate the process of obtaining hourly climatic data input and model parameters and to validate the accuracy of proposed pavement temperature models over an entire year, two distinct LTPP seasonal monitoring pavement (SMP) sites were selected for inclusion in this work: Pavement 48–1068 in Lamar, Texas, and Pavement 27–1028 in Otter Tail, Minnesota. These sites are among the very few with hourly temperature data for an entire year, and as a function of depth. Pavement temperatures at these two pavement sites were calculated based on the above proposed procedures and then compared to field measured temperatures. The average absolute error between hourly predicted temperatures and measured temperatures was used to indicate the accuracy of model prediction.

Lamar, Texas, Pavement 48–1068

As a complete record of measured hourly pavement temperatures was only available in 1994 in the LTPP database for pavement site 48-1068, pavement temperatures in 1994 were modeled and then compared to the measured data. The calculation started with collecting climatic data, including hourly solar radiation, ambient air temperature, and wind speed. In the NSRDB, hourly solar radiation data were listed by state and site name. Although solar radiation data for the Lamar site were not available, solar radiation data from a nearby site (Denison, 62 miles from Lamar) were available and were used instead. Daily maximum and minimum air temperatures recorded at the LTPP database were extracted and then combined with the daily air temperature pattern (developed using a time series analysis method based on limited

recorded hourly air temperature data at the nearest weather station) to obtain required hourly air temperature data. Daily average wind speed data at the pavement site were obtained directly from the LTPP database (Virtual Weather Station).

Values of model parameters were then estimated from the parameter map with interpolation. For Pavement 48–1068, an albedo of 0.15 (the albedo value at the nearest Pavement Site 48–4142), an algebraic difference between emissivity and absorption coefficients of 0.1 (the value at the nearest Pavement Site in Region C, 40–4165), and an absorption coefficient of 0.7 (the value at the nearest pavement site in the same humidity zone, 40–4165) were selected as constants throughout the year.

With estimates for these model parameters determined, pavement temperatures were calculated using the numerical simulation model at three different depths of 25, 128, and 232 mm below the surface. Figure II-7 shows a sample comparison of the calculations to the field measured temperatures over the one-year study period at 25, 128, and 232 mm below the surface. Statistically, the average absolute error between the measured and predicted temperatures of for the entire year was about 2.4 ^{o}C at 25 mm below the surface, 2.0 ^{o}C at 128 mm below the surface, and 2.2 ^{o}C at 232 mm below the surface. A close comparison in March was also provided at 25mm and 128mm to demonstrate the ability of model to capture daily pavement temperature fluctuation, as shown in Figure II-8.

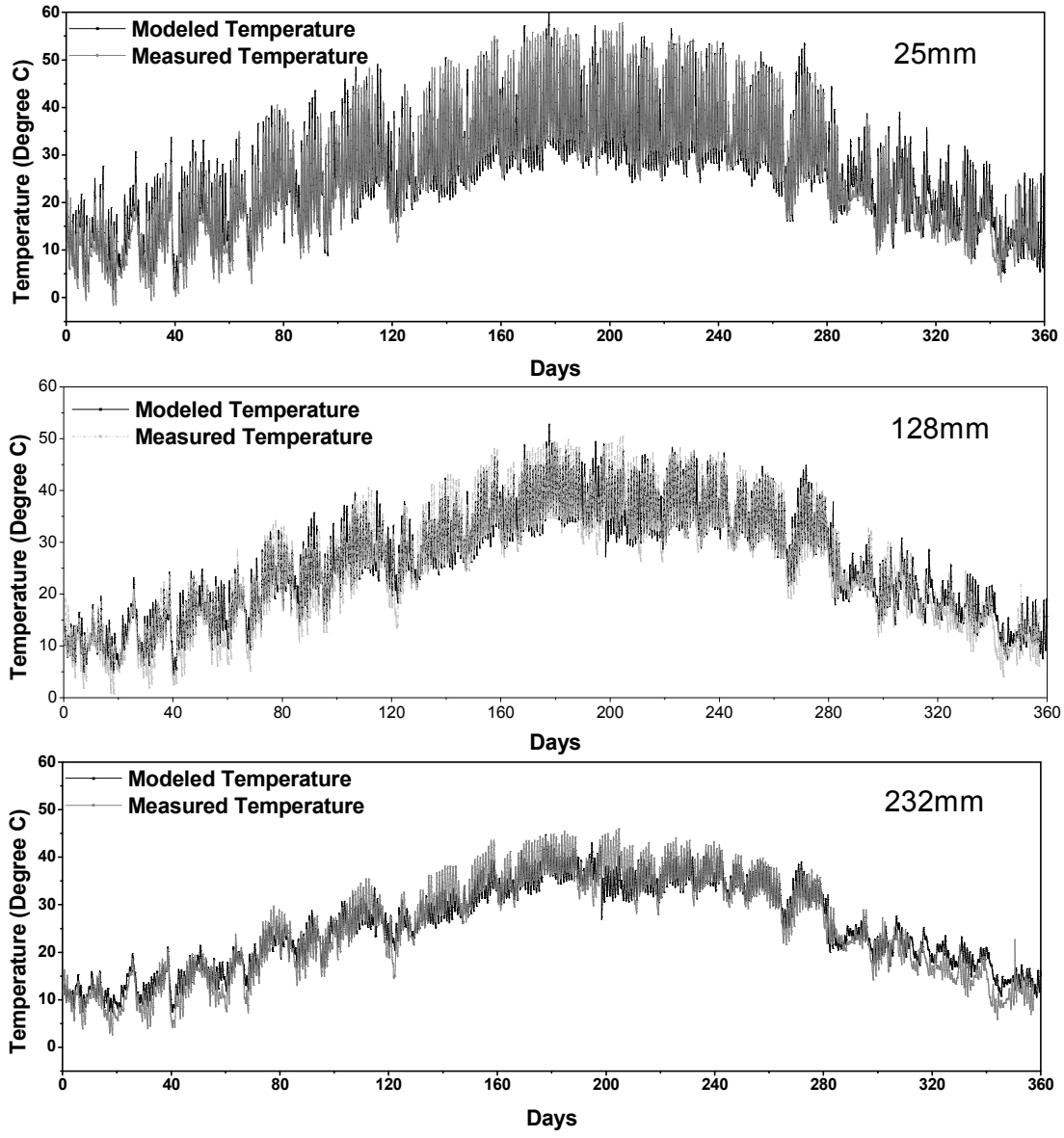

Figure II-7. Comparison of Model Predicted Annual Hourly Pavement Temperature and Field Measurement in Pavement 48-1068 [Lamar, Texas] at Depth of 25, 128, and 232 mm below the Surface

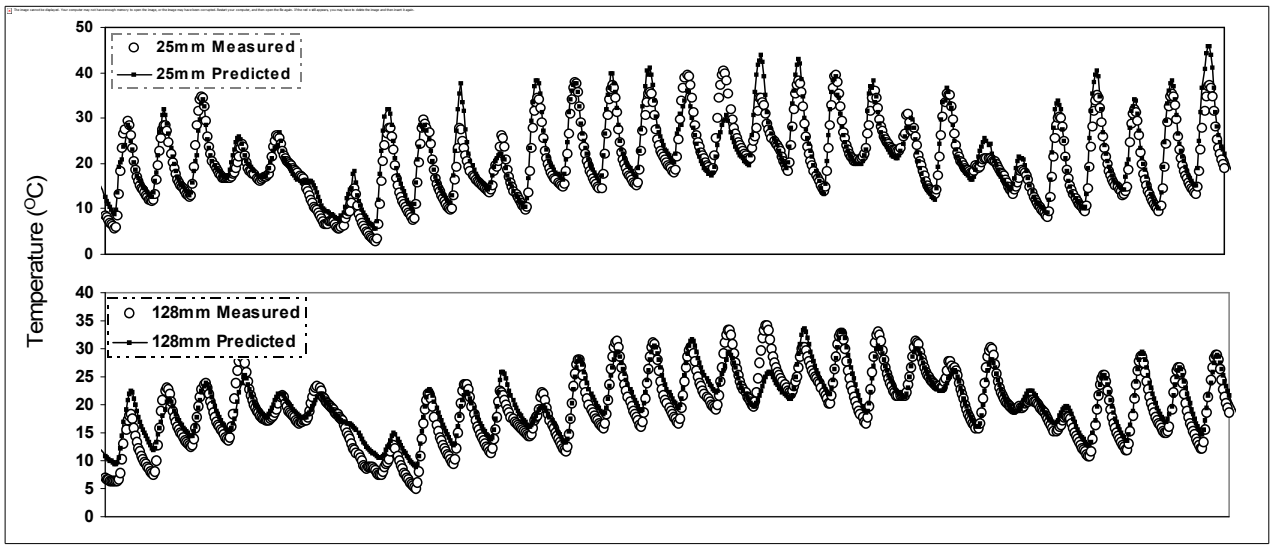

Figure II-8 Comparison of Model Predicted Hourly Pavement Temperature and Field Measurement of Pavement 48-1068 in March 1994 at 25mm and 128mm below the Surface

Otter Tail, Minnesota, Pavement 27–1028

As a complete record of measured hourly pavement temperatures was available in the LTPP database at this site only from April 1996 to March 1997, pavement temperatures during that period were modeled and then compared to measured data to validate the model. The procedure to obtain hourly climatic data and model parameters for the Otter Tail, MN, pavement is quite similar to that for Lamar, TX, except that two sets of model parameters were used because model parameters in the winter differ from the values obtained for the summer. The parameter values determined from the nearest Pavement Site 27–1018 for the month were albedo 0.3, the algebraic difference between emissivity and absorption coefficients 0.05, and the absorption coefficient 0.75. In the summer, these parameters that differed significantly from the winter values were: albedo 0.2, the difference between emissivity and absorption coefficients 0.05, the absorption

coefficient 0.75. The winter period, when the winter set of parameters needs to be used, was determined directly as the time when a high albedo value was recorded in NSRDB. At Fergus Falls (32 miles away from Otter Tail) from 1996 to 1997, a high albedo value was obtained only from January 1996 and January 1997. Therefore, for the one-year period April 1996 through March 1997, the winter set of parameter values were used only during January 1997.

With estimates for these model parameters determined, pavement temperatures were calculated using the numerical simulation model at three different depths of 25, 115, and 205 mm below the surface. Figure II-9 shows a sample comparison of the calculations to the field measured temperatures at pavement depths of 25, 115, and 205 mm below the surface. Statistically, the average absolute error between the measured and predicted temperatures was 1.8 ^{o}C at 25 mm below the surface, 2.0 ^{o}C at 115 mm below the surface, and 1.9 ^{o}C at 205 mm below the surface.

In general, while the model cannot exactly reproduce the measured pavement temperature profiles, it works quite well for these two sites. Statistically speaking, only 1.3 % of the calculations have an error as large as 10 ^{o}C while 46% percent of the calculations have an error less than 2 ^{o}C based on a yearly comparison. Further improvements to the model should incorporate heat transfer enhancement by precipitation or the effect of moisture freeze and thaw in the pavement. Although yearly pavement profiles at deeper depths are not shown for these two sites, the amplitude of daily temperature fluctuation attenuates with depth, while daily average temperature is about the same at different depths when comparing pavement temperature profiles at different depths.

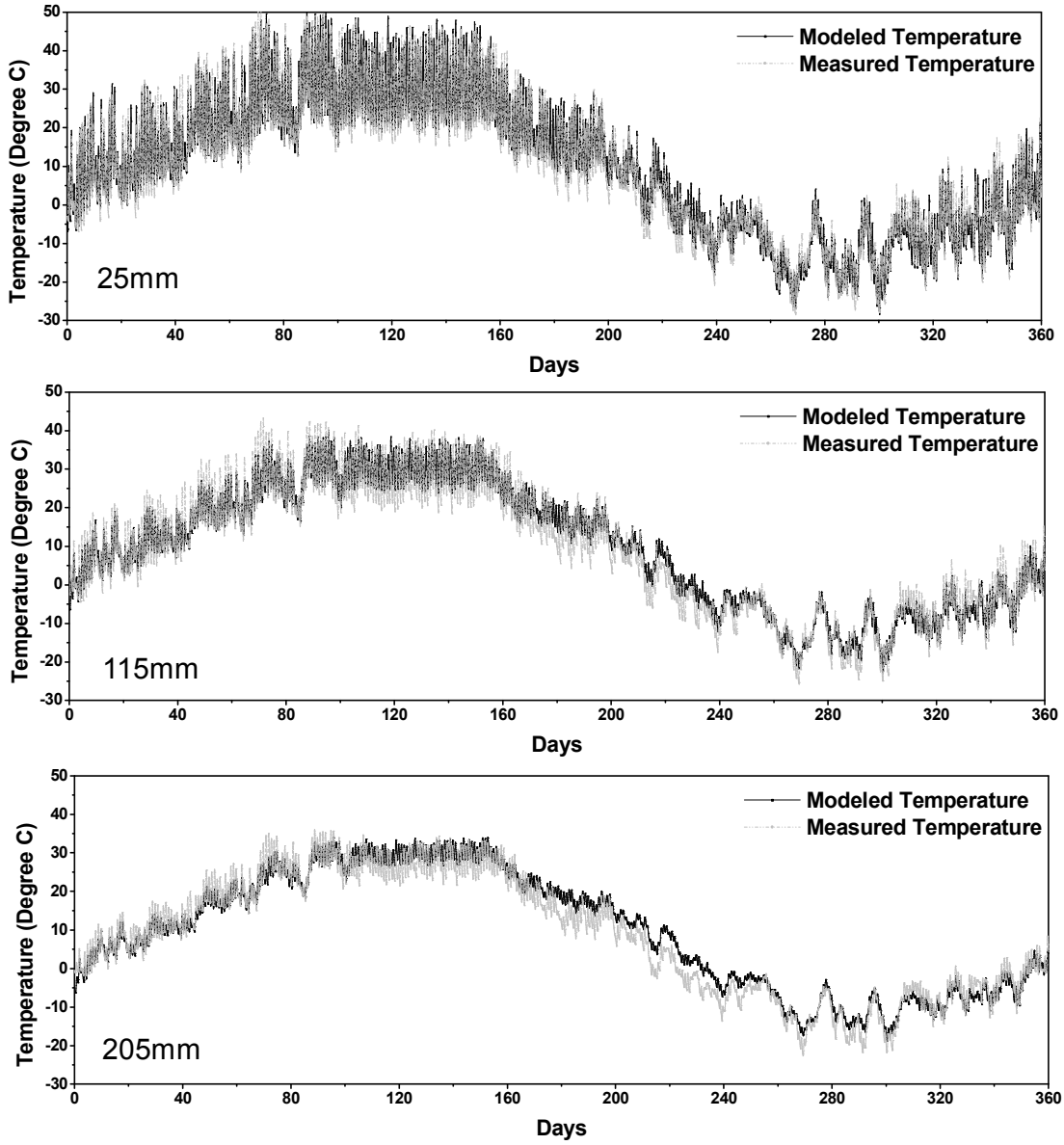

Figure II-9. Comparison of Model Predicted Annual Hourly Pavement Temperature and Field Measurement in Pavement 27–1028 [Otter Tail, Minnesota] at depth of 25, 115, and 205 mm below the Surface

Conclusions

An accurate model for pavement temperature prediction is critical in the study of asphalt pavement performance. This work provides a general tool to obtain accurate hourly pavement temperature as a function of depth at any desired pavement site for various applications, especially for calculations of asphalt binder oxidation in pavements where fairly accurate results are required. To this purpose, an improved one-dimensional model was developed to predict pavement temperature nationwide based on heat transfer fundamentals. The model employs commonly recorded hourly solar radiation, daily average wind speed, and interpolated hourly air temperature as climate input data. Three key site-specific model parameters were identified, and national distribution of their values correlates with climatic patterns, suggesting possible interpolation strategies based on climate. The temperature model, proposed data sources, and interpolated model parameters provided calculations that agreed well with field measurements, suggesting a general approach to predict pavement temperature nationwide with acceptable accuracy. This model provides a powerful tool for engineers for pavement design, performance modeling, and pavement durability.

CHAPTER III
OXYGEN DIFFUSIVITY IN ASPHALT BINDERS AND MASTICS

Introduction

Asphalt binder oxidation has been studied for many years with respect to reaction kinetics and the resulting chemical and physical changes. An important part of the oxidation process is the formation of carbonyl (– C=O) groups that increase the associations between polar species.[1, 54] The increased associations that arise because of the carbonyl formation produce a dramatic stiffening of the asphalt binder, characterized most notably by an increase in its low shear rate viscosity.[3, 4] This increase of low shear rate limiting viscosity relates exponentially to these carbonyl increases.

Given an adequate supply of oxygen, asphalt binders in pavements will harden and become brittle.[6] Over time, as their ductility decreases pavement cracking increases.[7, 28, 29, 30, 31, 32, 33] A key question is how quickly oxygen can be supplied to the asphalt binder to feed the reaction. The answer to this question lies in part on the permeability of the pavement to air through connected air voids, and in part on oxygen diffusivity in asphalt binders.

The literature is rather limited on oxygen diffusion in asphalt binder materials and on values of oxygen diffusivity and its relation to other asphalt binder properties. Part of the difficulty with measuring diffusivity is separating transport behavior from reaction. Lunsford made an early and important proof of principle attempt to measure oxygen diffusivity and its dependence on asphalt binder viscosity using fundamental transport and reaction theory on 1–mm asphalt binder films.[24] Although conceptually sound, the 1–mm asphalt binder films that he used were too thin to establish the strong diffusion dependence needed for accurate diffusivity measurements, the result of the films being designed for reaction kinetics measurements instead of diffusivity. Nevertheless, the work stands as an important demonstration of the method for making these measurements.

A further hindrance to oxygen diffusion in pavements is the presence of aggregates that are impervious to diffusion. Such aggregates require that oxygen molecules take a longer, more tortuous path through the asphalt binder, thus reducing the effective oxygen diffusivity. Measurements of this effect in asphalt mastics have not been reported.

The primary objective of this work was to measure oxygen diffusivity in both unmodified and modified asphalt binders using laboratory oxidation of asphalt binder films of known reaction kinetics and to relate these diffusivity measurements to temperature and binder rheology. A second objective was to quantify the effect of aggregate fines on oxygen diffusivity in mastics.

In this work, estimates of oxygen diffusivity in binders were made based on laboratory oxidation experiments in binder films of known reaction kinetics. Fundamental asphalt binder properties that influence oxygen diffusivity and effect of aggregate fines on oxygen diffusivity are also studied.

Materials and Methodology

Overview of Experimental Design

Asphalt binder or mastic samples were deposited into a pre-molded aluminum tray to form a thin asphalt binder/mastic film (Figure 1). Two surfaces were created: the exposed surface (ES) with direct interfacial contact between the asphalt binder material and atmospheric oxygen, and the substrate interface (SI) between the asphalt binder film and the aluminum support tray that is impermeable to oxygen. This configuration allows oxygen from the atmosphere above the ES to be absorbed by the film and then to diffuse and react throughout it, while blocking oxygen absorption at the SI. Reaction throughout the film results in an oxygen concentration gradient that is a function of time and depth inside the film and thus a difference in oxidation rates at the ES and SI. By comparing oxidation rates at the ES and the SI using an oxygen diffusion and reaction

model, oxygen diffusivity throughout the film can be estimated first by a method that assumes that the oxygen diffusivity is constant during the oxidation period and uniform throughout the film, at an appropriate average value. Then, this approximate method was verified with detailed calculations of the diffusion and reaction transport model. Using this method, oxygen diffusivities for a number of asphalt binders and polymer–modified asphalt binders of different rheology were determined at several temperatures. In addition, oxygen diffusivities for asphalt mastics with different volume fractions of fines were measured at several temperatures to study the effect of impermeable aggregate fines on oxygen diffusivity.

Materials

Eight asphalt binders (five base binders and three polymer modified binders) were used in this study to measure oxygen diffusivity in neat binders. Three asphalt mastics with three different volume fractions of aggregates fines (0, 10, and 25%) were prepared to evaluate the effect of fines on oxygen diffusivity. Due to experimental design limitations on the film thickness, aggregate fines (sandstone) sized between sieve #100 (150 μm) and sieve #200 (75 μm) were used to prepare the mastics. Table III-1 summarizes the binder materials used in this study, along with their oxidation and hardening properties.

All asphalt binders used in this study were pre-oxidized to move them past the fast-rate reaction period into the constant-rate reaction region. Constant-rate oxidation kinetics parameters (AP^{α} and E) for these binders, required for the oxygen diffusivity calculations, are also provided in Table III-1. The rate of oxidation in the constant-rate reaction region (indicated by carbonyl content production) can generally be described using an Arrhenius expression for temperature variation and pressure dependence, as given in Equation III-1. [1]

$$r_{CA} = \frac{\partial CA}{\partial t} = AP^{\alpha} e^{-E/RT} \qquad \text{(III–1)}$$

where, AP^{α} is the frequency (pre-exponential) factor, P is the pressure, α is the reaction order with respect to oxygen pressure, E is the activation energy, R is the gas constant, and T is the absolute temperature.

Values of AP^{α}, and E vary with the asphalt binder and were measured experimentally by oxidizing asphalt binders at different temperatures.

Table III-1 List of Materials and Material Parameters

Asphalt binder	Oxidation and Hardening Parameters				Mastics Prepared with
	AP$^{\alpha}$ ln(CA/day)	***E*** (kJ/Mol)	***HS*** (1/CA)	***m*** ln(poise)	
Alon 64-22	21.905	76.256	3.527	6.633	√
Alon 76-22	22.642	78.769	3.388	8.310	
SEM 64-22	21.611	75.228	4.935	5.551	√
SEM 70-22	22.051	76.468	4.028	7.047	√
Lion 64-22	23.013	79.002	3.739	5.535	
Lion 70-22	18.391	65.334	3.154	8.204	
Valero-H 64-22	18.769	67.649	4.427	6.248	
Martin 64-22	19.974	70.047	5.095	6.005	

Methodology

Asphalt Binder/Mastic Film Preparation

Asphalt mastics were prepared by stirring asphalt binder with fines at 163 ^{o}C, 1000 rpm for half an hour under a nitrogen blanket (to prevent oxidation). Thin asphalt binder or mastic films were fabricated by depositing the appropriate amount of asphalt binder or mastic in a pre-molded aluminum tray. The optimized film thicknesses of asphalt binder at each test temperature were 1.5 mm at 60 ^{o}C, 2 mm at 75 ^{o}C, and 2.5

mm at 90°C. The film thicknesses were designed to be thick enough to establish diffusion as a significant factor within the film, while not so thick as to give too long a test time.

Carbonyl Measurement

Oxidation of asphalt binder is characterized by formation of carbon and oxygen double bonds, C=O. A Nicolet 6700 Fourier Transform Infrared Spectroscopy (FT-IR) spectrometer was used to analyze the carbonyl content. Growth in the area under the FTIR spectrum from 1650 to 1820 cm^{-1} in arbitrary units, the carbonyl area (CA), is used to represent this oxidation.

Measurement of Oxidation Rates at the ES and SI

Asphalt binder/mastic films were oxidized in pressure oxygen vessels at three different temperatures and at 1 atm air pressure. Samples were retrieved at different time points. Small amounts of asphalt binder were scratched using a spatula from the top surface of the film, and used to measure carbonyl content at the ES. Then, asphalt binder was gently removed from the aluminum tray, and the remaining asphalt binder residue at the asphalt binder and aluminum support interface were collected to measure carbonyl content at the SI. At each temperature, a constant-rate model was fit to the carbonyl content measurements to obtain the oxidation rate at both the ES and SI.

Limiting Zero Shear Complex Viscosity (η_o*) Measurement

The rheological properties of the asphalt binders were measured on a CarriMed 500 controlled stress dynamic shear rheometer, with 2.5 cm diameter parallel-plate geometry and 500 micrometer gap. Viscosity master curves were constructed with viscosity measurements at the 60 °C and 80 °C in the frequency range from 0.1 rad/s to

100 rad/s. The specific rheological property used in this work that relates well to oxygen diffusivity is the low-shear rate limiting complex viscosity η_o*. This property is read from a viscosity master curve at the low frequency end where viscosity approaches a plateau. This property is independent of frequency or shear rate for unmodified binders.

Estimation of Base Binder η_o* for Polymer-modified Asphalt Binders (PMB)

The viscosity of each of the polymer-modified binders was determined as above, but an estimate of the hypothetical base binder viscosity in the PMB also was made. This determination was made from the measured viscosity of the PMB, coupled with hardening susceptibility relations for both the PMB and the base binder, as described subsequently. This viscosity versus carbonyl relationship for both the base asphalt binder and the PMB are well represented by Equation 2. [4, 22, 23]

$$\ln \eta_0^* = HS \cdot CA + m \qquad \text{(III-2)}$$

where, *HS* is termed the hardening susceptibility, the change in log-viscosity with respect to the change in carbonyl content, and *m* is the log-viscosity intercept. *HS* and *m* are asphalt binder dependent and are affected by polymer modification; their values for the selected asphalt binders (for both base binders and their corresponding polymer modified binders) are summarized in Table III-1.

Oxidation of the PMB increases the CA of the asphalt binder component of the PMB, but the polymer makes no contribution. Accordingly, η_o* for the PMB together with the *HS* relationship for the PMB was used to calculate the corresponding CA for the PMB; then this CA was used to calculate η_o* for the base asphalt binder using its own specific *HS* relationship.

.

Thin Film Model for Oxygen Diffusivity Calculation

Thin asphalt binder films are fabricated by depositing an appropriate amount of asphalt binder or mastic into a pre-molded aluminum tray to form a finite thickness as depicted in Figure III-1. There are two surfaces in this thin film model, the ES that is in direct contact with oxygen, and the SI between the asphalt binder and aluminum tray support. The oxygen concentration in the asphalt binder at the ES is in equilibrium with the ambient atmosphere, 1 atm for these experiments. At the SI, due to the impermeable nature of aluminum, the oxygen concentration gradient is zero. Inside the film, asphalt binder oxidation (and thus oxygen consumption) results in asphalt binder hardening over time and an oxygen concentration gradient that is a function a time and depth inside the film.

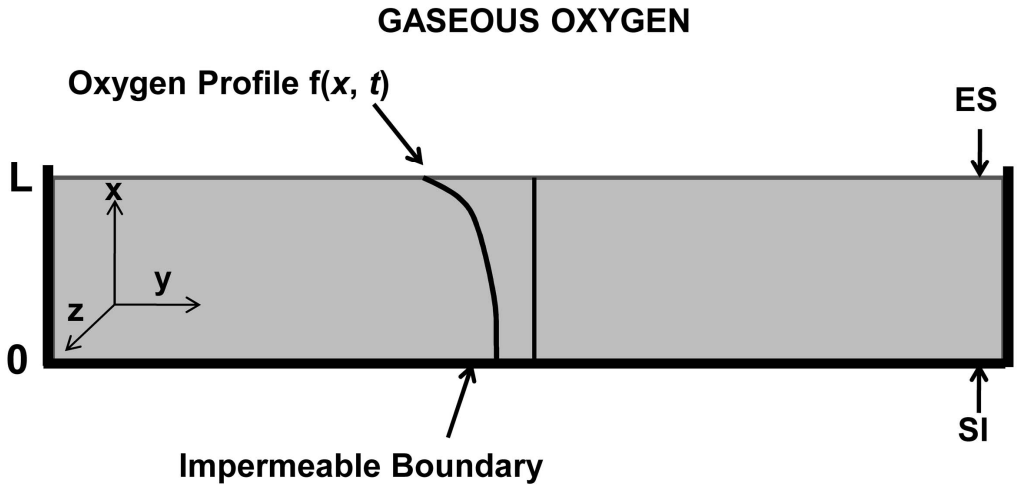

Figure III-1. Schematic of Thin Film Model Configuration

A mathematical model accounting for oxygen diffusion and reaction in a differential volume of the asphalt binder film is given by:

$$\left(\frac{\partial C_{O_2}}{\partial t}\right) = -\nabla \cdot N_{O_2} - r_{O_2} \qquad \text{(III-3)}$$

where, C_{O_2} is the oxygen concentration and r_{O_2} is the rate of oxygen consumption.

The molar flux of oxygen, N_{O_2}, can be expressed by Fick's first law of diffusion as:

$$N_{O_2} = -\mathcal{D}_{O_2} \nabla C_{O_2} \tag{III-4}$$

where, $\mathcal{D}_{O_2}$ is the oxygen diffusivity in the asphalt binder.

Oxygen transport in the asphalt binder film is assumed to occur in only one direction, based on the experiment configuration. Equation III-1 is further developed as:

$$\left(\frac{\partial C_{O_2}}{\partial t}\right) = \left(\frac{\partial \mathcal{D}_{O_2}}{\partial x}\right)\left(\frac{\partial C_{O_2}}{\partial x}\right) + \mathcal{D}_{O_2}\left(\frac{\partial^2 C_{O_2}}{\partial x}\right) - r_{O_2} \tag{III-5}$$

where, x is the depth into the film and diffusivity varies with depth due to different levels of oxidation (binder hardening) in the film.

Because the experiments are designed at low oxygen pressure, the ideal gas law converts oxygen gas phase partial pressure P_{O_2} to asphalt binder phase concentration C_{O_2} using T and the dimensionless Henry's Law constant h:

$$C_{O_2} = h\left(\frac{P_{O2}}{RT}\right) \tag{III-6}$$

For asphalt materials, a dimensionless value of 0.0076 at 30°C has been estimated based on the literature. [55] It is a function of temperature according to Equation III-7:

$$h = h_0\left[1 + 0.00215\left(T - T_r\right)\right] \tag{III-7}$$

where, h_0 is the dimensionless Henry's law constant at reference temperature T_r, and the unit for the constant is in reciprocal degrees Celsius.

It has been found that the oxygen reaction rate is directly proportional to carbonyl growth rate for asphalt binders:

$$r_{O_2} = cr_{CA} \tag{III-8}$$

where, c is dependent of asphalt binder, ranging from 2.75×10^{-4} gmol O_2 / mL CA to 4.59×10^{-4} gmol O_2 / mL CA for c obtained for ten asphalt binders.[56] In this study, an average value of 3.71 is used.

Combining Equation III-4, III-5, and III-7, the governing equation for this diffusion and reaction process is given in terms of P, h, and CA kinetics as:

$$\left(\frac{\partial P}{\partial t}\right) = \left(\frac{\partial \mathcal{D}_{O_2}}{\partial x}\right)\left(\frac{\partial P}{\partial x}\right) + \mathcal{D}_{O_2}\left(\frac{\partial^2 P}{\partial x}\right) - \left(\frac{cRT}{h}\right)r_{CA} \tag{III-9}$$

where, P throughout the film is the gas phase oxygen partial pressure that would be in equilibrium with the asphalt binder phase oxygen concentration at that point in the film. Equation III-9 is cast in terms of P rather than C_{O_2} because the reaction kinetics is cast as a function of P to avoid measurement of C_{O_2}.

For the final form, the boundary conditions and the initial condition are:

$P_{ES} = P$ (gas)	at $x = 0$	[ES]
$\frac{\partial P}{\partial x} = 0$	at $x = L$	[SI]
$P = 0$	at t = 0	[Initial Condition]

With oxygen diffusivity (or diffusivity as a function of the level of oxidative aging, CA) specified, this model can be solved numerically to obtain the oxygen partial

pressure in the film as a function of time, temperature, and depth below the film surface. However this model as stated is not sufficient to allow determining values for diffusivity and the model must be viewed differently.

In this work, the oxygen partial pressure at the SI at a specified time was inferred from measured reaction rates at both the ES and SI and used as additional information. Applying Equation III-1 to both surfaces, oxidation rates at the ES and the SI relate to partial pressures according to:

$$r_{ES} = AP_{ES}{}^{\alpha} e^{-E/RT} \tag{III-10}$$

$$r_{SI} = AP_{SI}{}^{\alpha} e^{-E/RT} \tag{III-11}$$

For a given asphalt binder, A and E are constant and the film temperature is uniform, so combining Equation III-10 and III-11 gives:

$$P_{SI} = P_{ES}\left(\frac{r_{SI}}{r_{ES}}\right)^{1/\alpha} \tag{III-12}$$

From Equation III-12, a value for the oxygen pressure at the SI can be calculated by comparing measured oxidation rates at the ES and the SI. Reaction order α for a number of asphalt binders has been measured and varies from about 0.23 to 0.3;[1] an average value of 0.27 was used for these calculations.

The estimated value of the oxygen pressure at the SI is based on the average oxidation rate for the entire test period, while the exact time to achieve this particular oxygen pressure at the SI is unknown. However, a linear decrease of pressure at the SI (P_{SI}) over time is indicated by model simulation. With this observation, $P_{SI(i)}$ at given time t can be shown as:

$$P_{SI(i)} = P_{SI(0)} + \frac{\left(P_{SI(0)} - P_{SI(1)}\right)}{\left(t_0 - t_1\right)}\left(t_i - t_0\right) \tag{III-13}$$

Here, $P_{SI(0)}$ is P_{SI} at the start of the experiment, time (t_0); and $P_{SI(1)}$ is P_{SI} at the end of the experiment, at time (t_1).

The average oxidation rate at the SI for the entire testing period will be a function of $P_{SI(i)}$ according to:

$$r_{SI} = \frac{\int_{t0}^{t1} k P_{SI(i)}{}^{\alpha} dt}{(t_0 - t_1)} e^{-E/RT} \qquad \text{(III-14)}$$

By substituting the $P_{SI(i)}$ expression of Equation III-13 into Equation III-14 and feeding Equation III-14 into Equation III-12, P_{SI} estimated based on the oxidation rate at both SI and ES for the entire testing period as follows:

$$P_{SI} = \left[\frac{\left(P_{SI(0)}{}^{1+\alpha} - P_{SI(1)}{}^{1+\alpha} \right)}{\left(P_{SI(0)} - P_{SI(1)} \right)(1+\alpha)} \right]^{1/\alpha} \qquad \text{(III-15)}$$

$P_{SI(0)}$ ranges from 0.15 to 0.2 atm, and $P_{SI(1)}$ ranges from 0 to 0.1 atm in experiments. In practice, the value of P_{SI} obtained is always close to the mean value of $P_{SI(0)}$ and $P_{SI(1)}$, suggesting that the time to obtain this measured value of P_{SI} at SI is close to the mean time for the experiment.

With an estimated value of oxygen pressure at the SI at a given time and depth in the asphalt binder film and asphalt binder reaction kinetics parameters known, a trial and error numerical solution of the model was used to obtain optimal estimates of diffusivity by comparing oxygen pressure at the SI (inferred from the measured oxidation rate) to these model calculations according to Equation III-9. To start with, an assumption of constant oxygen diffusivity during the relatively short testing period is made.

There exists an oxygen concentration gradient in an asphalt binder film where oxygen transport is limited by diffusion, which will further induce gradients of asphalt binder oxidation rate, asphalt binder oxidation level, and asphalt binder rheology with time. Oxygen diffusivity, as a property that might be influenced by asphalt binder

physical properties, should also be a function of time and depth in the film. Because of that, Equation III-9 states that oxygen diffusivity is a variable, changing with time and depth in the film as the oxidation level changes. However, how oxygen diffusivity changes with oxidation level is not clear. In this study, an assumption of constant oxygen diffusivity during the short testing period (independent of oxidation level and depths in the film) was made, and diffusivities for asphalt binders were the calculated based on this assumption. These calculated diffusivity values were then used to correlate with asphalt binder rheology to establish relationships between oxygen diffusivity and asphalt binder rheology. By comparing calculated carbonyl growth at both the ES and the SI (using Equation III-9 with the established correlation) with measured value, the initial assumption of constant oxygen diffusivity during the short testing period was examined.

Results and Discussion

Oxidation Rates at ES and SI of Asphalt Binder Film

Carbonyl growth at both the ES and the SI were measured as a function of oxidation time and temperatures, as shown in Figure III-2. For a given oxidation temperature, the oxidation rate at the SI is less than the oxidation rate at the ES, verifying the existence of an oxygen gradient in the film, which is essential for diffusivity measurement. At each temperature, measurements of CA at both the ES and the SI over an appropriate test period were used to obtain estimates of constant oxidation rates. Complete data on measured CA at the ES and the SI for the eight selected asphalt binders are reported in Appendix A.

Estimation of P_{SI} and Calculation of $\mathcal{D}_{O_2}$

Oxygen pressure at the SI was then calculated by comparing oxidation rates at the ES and the SI with Equation III-12. Then, with SI oxygen pressures, their corresponding times determined as described previously, asphalt binder film thickness, and asphalt binder reaction kinetics parameters known; oxygen diffusivity for each binder and temperature was estimated numerically based on the model described previously. For each experiment, Table III-2 shows the P_{SI} corresponding to the measured oxidation rate at the SI, the approximate time when this P_{SI} value is reached, and the diffusivity estimate. Diffusivities were of the order of 10^{-10} to 10^{-11} m^2/s for temperatures from 60 to 90 °C.

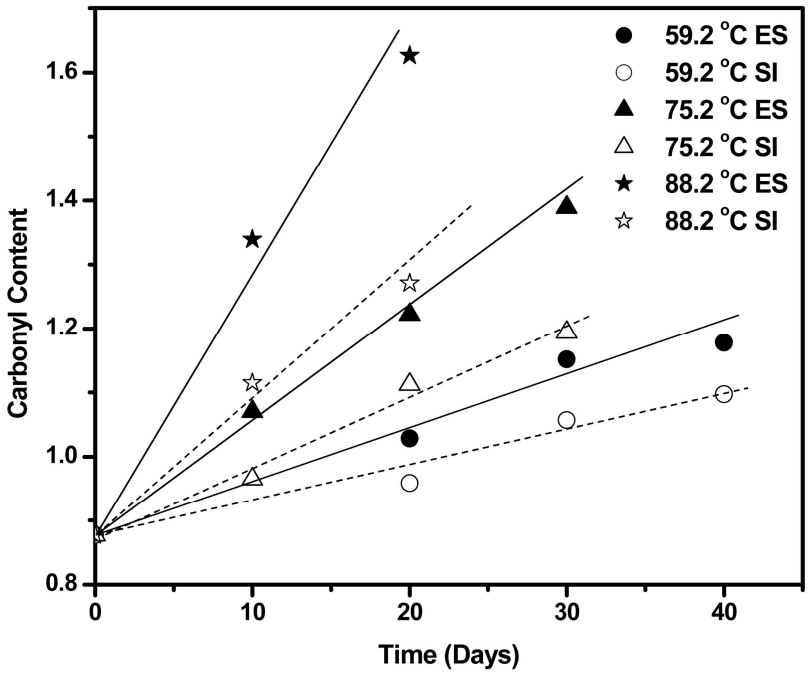

Figure III-2. Sample Comparison of Oxidation Rate at ES and SI (SEM 64-22)

Correlation of $\mathcal{D}_{O_2}$ with η_o*

Further analysis was conducted to establish correlations between asphalt binder material properties, test conditions, and oxygen diffusivity. Diffusivity of a single solute Molecule A through a stationary Medium B is given by: [40]

$$\mathcal{D}_{AB} = \mathrm{K}T\left(\frac{u_A}{F_A}\right) \tag{III-16}$$

where T is temperature, K is Boltzmann's constant, (u_A/F_A) is the mobility of a molecule A (the steady-state average velocity attained by the molecule under the action of a unit force).

For asphalt binder materials, this property might be highly associated with asphalt binder viscosity and the extent of molecular interaction for different asphalt binder components. To this effort, oxygen diffusivity divided by absolute temperature ($\mathcal{D}_{O_2}/T$) was plotted against the asphalt binder's low shear rate limiting viscosity (η_o*) at 60 ^{o}C, each on a log scale, as shown in Figure III-3. For polymer modified binders, it was found that the viscosity of the base asphalt binder correlated much better with diffusivity than that the viscosity of the modified asphalt binder did, suggesting that from the perspective of diffusing oxygen molecules, the relevant diffusion medium is the base asphalt binder, not the polymer modified network.

As shown in Figure III-3, a clear decrease of $\mathcal{D}_{O_2}/T$ with increases in η_o* was observed for each binder; and the data as a whole show a clear power law dependence that is consistent with Equation III-17:

$$\frac{\mathcal{D}_{O_2}}{T} = 5.21\times10^{-12}\left(\eta_0^{\,*}\right)^{-0.55} \tag{III-17}$$

Table III-2. Summary of P_{SI} and D_{O2} for Studied Asphalt Binders

Asphalt	Temperature (°C)	Time[a] (days)	P_{SI} (atm)	D_{O2}[b] (m^2/s)
Alon 64-22	59.3	25	0.0332	1.20×10^{-11}
	75.2	15	0.0088	4.42×10^{-11}
	88.2	10	0.0604	2.64×10^{-10}
Alon 76-22	63.4	15	0.1172	2.90×10^{-11}
	76.2	15	0.0984	1.00×10^{-10}
	87.3	5	0.0896	3.05×10^{-10}
SEM 64-22	59.2	20	0.0597	1.42×10^{-11}
	75.2	15	0.0408	6.55×10^{-11}
	88.2	10	0.0184	1.75×10^{-10}
SEM 70-22	59.2	20	0.0795	1.68×10^{-11}
	75.2	15	0.0311	5.35×10^{-11}
	88.2	15	0.0187	2.48×10^{-10}
Lion 64-22	55.8	25	0.0517	1.05×10^{-11}
	74.6	20	0.0551	7.60×10^{-11}
	89.2	10	0.0686	3.58×10^{-10}
Lion 70-22	63.4	20	0.1237	5.40×10^{-11}
	76.2	15	0.1096	1.62×10^{-10}
	87.3	5	0.0926	4.10×10^{-10}
Valero-H 64-22	55.8	25	0.0154	8.60×10^{-12}
	74.6	20	0.0731	6.61×10^{-11}
	89.2	10	0.0465	1.80×10^{-10}
Martin 64-22	63.4	15	0.0224	1.58×10^{-11}
	76.2	15	0.0388	7.70×10^{-11}
	87.3	5	0.0637	2.60×10^{-10}

[a]The time at which oxygen pressure in the film at the SI reaches P_{SI} (near the mid-time).
[b]The (uniform) diffusivity throughout the film at the reported time.

Interestingly, Equation III-17 can also be partially validated with fundamental laws, with the assumption that asphalt binder is a colloidal system with discrete asphaltene hard cores suspended in a maltene continuous phase. An effective oxygen

diffusivity, in this scenario, will be a function of volume fraction of asphaltene (which is impermeable to oxygen) as follows:

$$\frac{\mathcal{D}}{\mathcal{D}_0} = 1 - \frac{3\phi}{2+\phi} \tag{III-18}$$

where, $\mathcal{D}$ is effective diffusivity, $\mathcal{D}_0$ is diffusivity in the maltene phase, and Φ is the volume fraction of asphaltene.

In the meanwhile, using the viscosity mean-field theory,[3] the viscosity of a solvent is increased by solid spherical particles in relation to their volume fraction according to:

$$\eta = \eta_0 e^{2.5\phi} \tag{III-19}$$

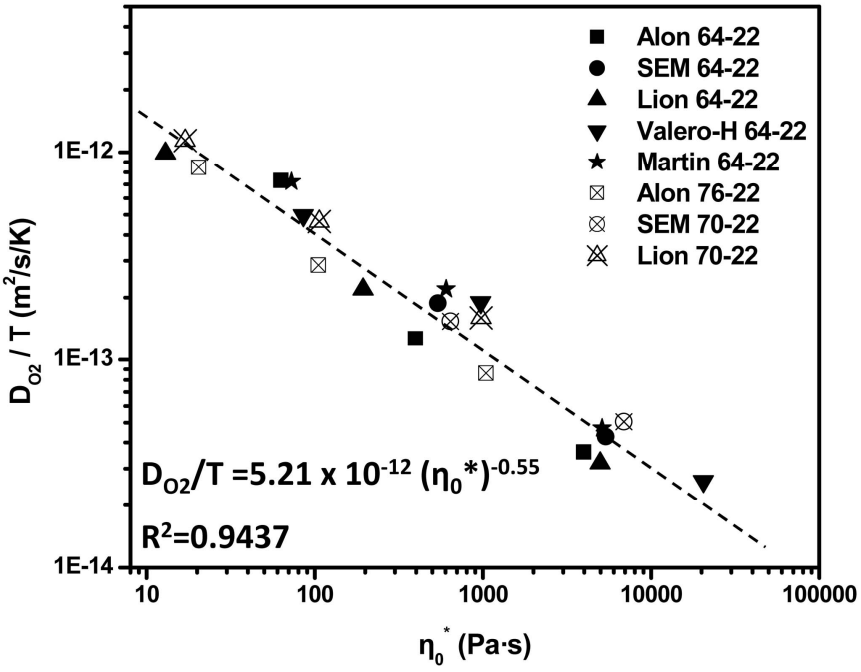

Figure III-3. Correlation of D/T with Limiting Viscosity (η_o*)

Assuming there is a correlation of the form of Equation III-17, with a pre-exponential unknown value of *A* and unknown power factor of *B*, substituting Equations III-18 and III-19 into Equation III-17 leads to:

$$B \approx \frac{-3\phi}{5\phi + 2.5\phi^2} \qquad \text{(III-20)}$$

The typical asphaltene content in asphalt binderS is from 5 to 30 percent, which gives a range of *B* from –0.52 to –0.59. The value of B obtained from the data fell within this theoretical range, consistent with the empirical correlation of Equation III-14. With this correlation, a value of oxygen diffusivity can be obtained by measuring the low shear rate limiting viscosity of an asphalt binder, which is an easily measurable property.

Prediction of Carbonyl Growth in an Asphalt Binder Film with ($\mathcal{D}_{O_2}/T$) and (η_o*) Correlation

The correlation between ($\mathcal{D}_{O_2}/T$) and (η_o*) discussed previously is based on diffusivity values that were calculated using a pseudo-steady-state assumption of constant oxygen diffusivity during the oxidation period, in spite of the fact that as oxidation proceeded, $\mathcal{D}_{O_2}$ decreased throughout the film and in a way that varied with depth in the film. To evaluate this assumption, carbonyl growth over time at the ES and SI for the various experiments was calculated using Equation III-9 while allowing oxygen diffusivity to change with oxidation according to Equations III-2 and III-17. These CA values were then compared to experimental measurements. Figure III-4 shows a sample comparison of CA versus oxidation time for an asphalt binder film of SEM 64-22. There is a good match between model calculations and experimental measurement of carbonyl growth, suggesting that the ($\mathcal{D}_{O_2}/T$) versus (η_o*) correlation describes the experimental data well, and that the diffusivity values determined by using the pseudo-

steady-state assumption over the test period are accurate to within the limitations of the data. Complete data on measured CA at the ES and the SI for the eight selected asphalt binders are reported in Appendix A.

As a further assessment of the accuracy of the diffusivity values reported above, the effects of varying the pressure power α in kinetics Equation III-1 and the factor relating the reactive incorporation of oxygen into asphalt binder molecules to FTIR CA measurements, c in Equation III-8, were determined. These parameters vary between asphalt binders, and averages of the values that have been measured to date were used in the diffusivity calculations. Measured values of α range from about 0.23 to 0.30 with an average of 0.27 used in the calculations, while c varies from about 2.75×10^{-4} to 4.59×10^{-4} gmol O_2 / mL *CA* with an average value of 3.71×10^{-4} gmol O_2 / mL *CA* used in the calculation. The sensitivity of estimated oxygen diffusivity values to variations in α and c is demonstrated in Figure III-5 for asphalt binder SEM 64-22.

Varying α over the range of values results in diffusivity variations of about 25 %. Similarly, variations in c result in diffusivity variations of about 60 %. A more complete assessment of diffusivity confidence intervals was not been made.

Effect of Mastic Fines on $\mathcal{D}_{O_2}$ in Asphalt Binders

A further hindrance to oxygen diffusion through asphalt binders in pavements is the presence of aggregate fines that are impervious to diffusion. To quantify this effect, oxygen diffusivities for three asphalt mastics with three different volume fractions of aggregate fines (0, 10, and 25 %) were measured. The data are summarized in Table III-3.

A universal trend of decreasing oxygen diffusivity with an increase in the volume fraction of fines was observed for each asphalt binder at each test temperature. Other than volume fraction of filler, oxygen diffusivity in mastics does not show any clear dependence on either test temperatures or asphalt binder types beyond that shown in Figure III-5.

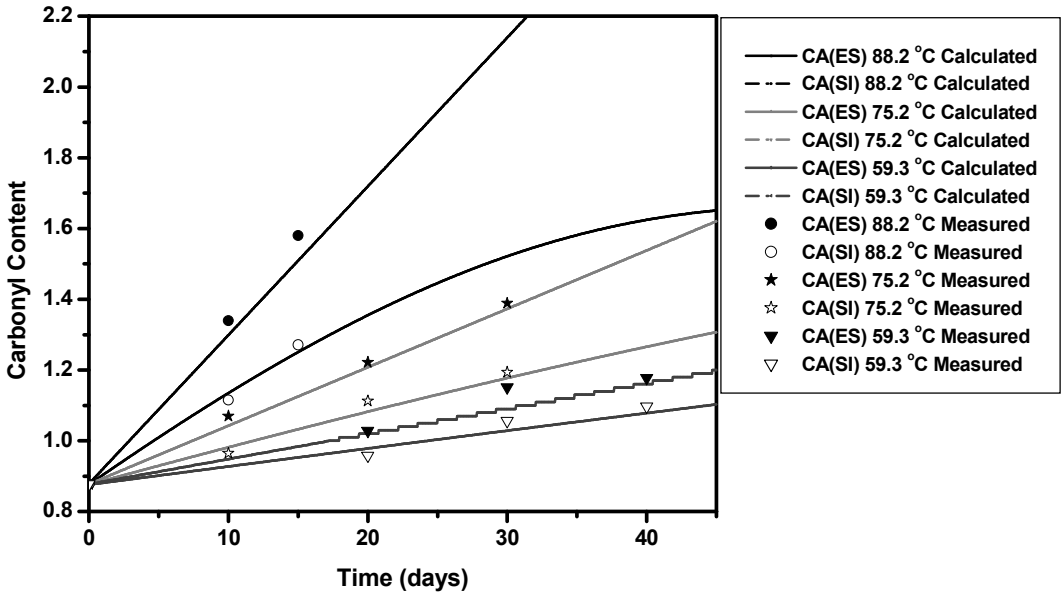

Figure III-4. Sample Calculation of Carbonyl Growth at ES and SI of an Asphalt Binder Film of SEM 64-22: Model Calculation vs. Experimental Measurement

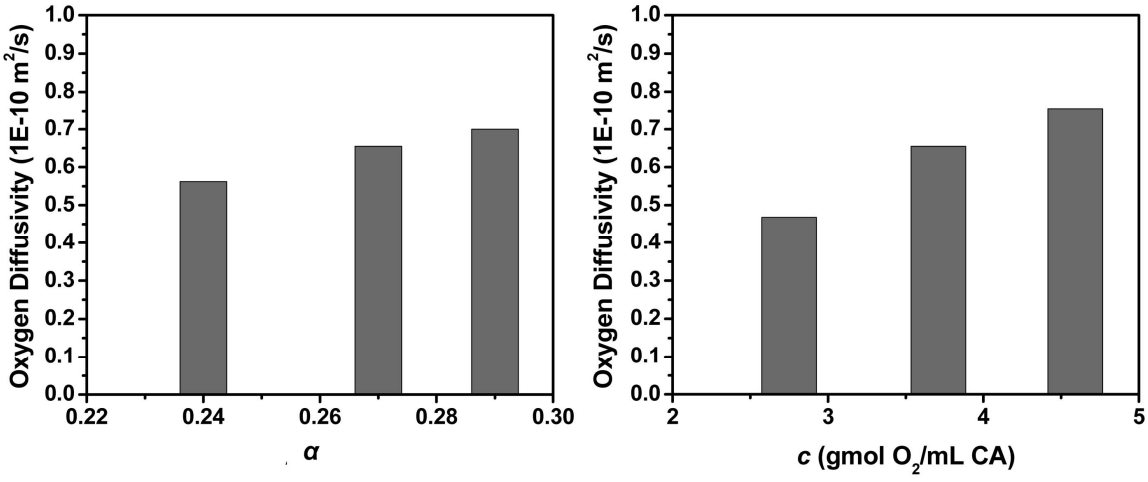

Figure III-5. Sensitivities of Calculated Oxygen Diffusivity on *c* and *α*

The effect of volume fraction of inclusions on transport behavior in heterogeneous materials has been well understood for many years. Theoretically, with a known volume fraction of fines for a given mixture design, oxygen diffusivity in mastics can be estimated from those conventional prediction models to a very reasonable degree of accuracy. Figure III-6 shows the comparison of measured average diffusivity dependency on volume fraction of fines with what is predicted by conventional models (Maxwell, Rayleigh, or Non-spherical complex models). A very good fit between those averages and the predictions of the conventional models is evident. Note also that over the volume fraction range from 0 to 60 %, these three model predictions agree well with each other.

Table III-3 Summary of D_{O2} for Studied Asphalt Mastics at Different Volume Fraction of Aggregate Fines

Mastics	Temperature	D_{O2} (m^2/s)		
		ϕ=0%	ϕ =10%	ϕ =25%
Alon 64-22	58.3	1.20×10^{-11}	8.60×10^{-12}	5.95×10^{-12}
	75.0	4.42×10^{-11}	3.90×10^{-11}	3.60×10^{-11}
	87.8	2.64×10^{-10}	2.16×10^{-10}	1.65×10^{-10}
SEM 64-22	62.9	1.42×10^{-11}	1.10×10^{-11}	9.63×10^{-12}
	75.8	6.55×10^{-11}	6.32×10^{-11}	3.48×10^{-11}
	88.4	1.75×10^{-10}	1.40×10^{-10}	1.00×10^{-10}
SEM 70-22	58.3	1.68×10^{-11}	1.38×10^{-11}	9.65×10^{-12}
	75.0	5.35×10^{-11}	4.70×10^{-11}	3.80×10^{-11}
	87.8	2.48×10^{-10}	2.30×10^{-10}	1.63×10^{-10}

Calculation of Pavement Oxidation

To demonstrate the importance of oxygen diffusivity in estimating pavement oxidation rates, example calculations were made using the pavement thermal and transport model.[42]

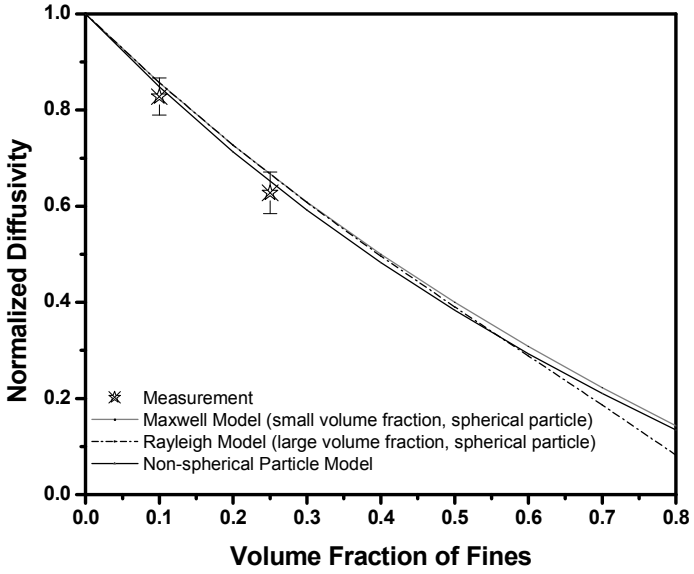

Figure III-6 Effect of Volume Fraction of Aggregate Fines on Oxygen Diffusivity

The model includes simplified air void characteristics, a pavement temperature profile model,[57] asphalt binder oxidation kinetics, and oxygen diffusivity. Holding all model input parameters (temperature, air void properties, binder kinetics parameters) constant, the oxidation rate at a depth of 0.02m below the pavement surface was calculated using the log $\mathcal{D}_{O_2}/T$ versus log η_o* correlation (Equation III-12) and compared to a calculation performed with a single oxygen diffusivity.

The results are shown in Figure III-7. Diffusivity values for the field conditions of these calculations ranged from 10^{-13} to 10^{-11} m^2/s (varying with field temperature and asphalt binder viscosity). A decrease in the average yearly oxidation rate (from 0.064 CA/year in the first year to 0.052 CA/year in the seventh year) was observed due to oxidative hardening of the asphalt binder and a consequent decrease in diffusivity at a fixed temperature, in accordance with Equation III-12. Models that use a constant diffusivity at each temperature fail to capture this hardening effect on oxidation rates.

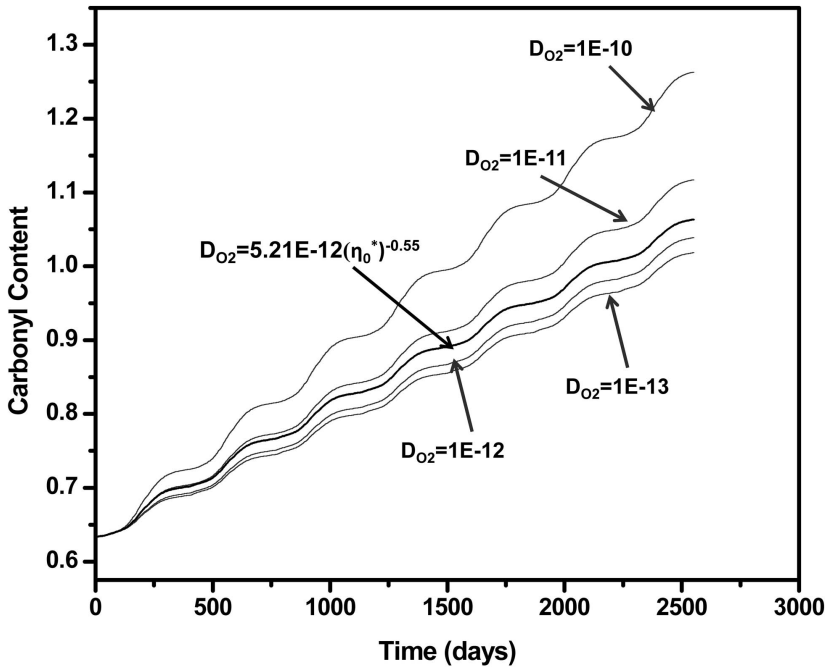

Figure III-7 Sample Calculation of Pavement Oxidation with Different Oxygen Diffusivity

Conclusions

In this work, estimates of oxygen diffusivity in asphalt binders were made based on laboratory oxidation experiments in binder films of known reaction kinetics. Comparing the oxidation rates at the asphalt binder surface (ES) and at a solid-binder interface (SI) at the film depth was used to estimate oxygen diffusivity.

For asphalt binders, oxygen diffusivities ($\mathcal{D}_{O_2}$) ranged from10^{-10} to 10^{-11} m^2/s, varying with temperature (T) and asphalt binder low shear rate limiting viscosity (η_o*); $\log(\mathcal{D}_{O_2}/T)$ varied linearly with $\log(\eta_o^*)$ for both base asphalt binders and polymer modified asphalt binders according to Equation III-17. For asphalt mastics, oxygen diffusivity was observed to decrease as filler volume fraction increased. Quantitatively, this effect follows a theoretical estimate of the effect of a dilute suspension of spherical inclusions on diffusivity.

CHAPTER IV
IMPROVED MODELING OF ASPHALT BINDER OXIDATION IN PAVEMENTS AND PAVEMENT AIR VOID CHARACTERIZATION

Introduction

Although asphalt pavements are designed for optimum performance initially, over time as asphalt binders oxidize, the properties of the asphalt binder change, resulting in decreased pavement durability. To design asphalt concrete pavement with maximum pavement durability, binder oxidation must be taken into account. One essential implementation issue in this regard is the ability to predict quantitatively how fast and how deep oxidation occurs for a given pavement over time.

To this purpose, oxidation in pavements has been modeled based on oxygen transport and reaction phenomena and air void structures in asphalt pavements. Recent studies have revealed that the majority of air voids in pavements are interconnected air channels, from top to bottom of the specimen.[7, 8] This connectivity of air voids assures that ambient air can diffuse and/or flow into the air void channels and provides a path for access to and diffusion and reaction within the adjoining asphalt binders. From this perspective, oxygen transport and reaction in pavements is described as two interlinked steps: 1) diffusion and/or flow of oxygen into the interconnected air voids; and 2) diffusion of oxygen from those air voids into the nearby asphalt binder-aggregate matrix accompanied by reaction with the asphalt binder.

Prapaitrakul et al. made the first attempt recently to calculate asphalt binder oxidation in pavements with an oxygen transport and reaction model,[24,25] with the same concept that air void channels in pavements are positioned and connected from top to bottom. A diffusion and reaction model was formulated that accounts for oxygen diffusion and reaction in the cylindrical shell surrounding an air void channel. Two air void properties, average air void radius (r_{PS}) and the average half-distance between two adjacent pores (r_{NFB}) were calculated based on bulk analysis of air void in a pavement

and used to define a cylindrical shell matrix through which oxygen diffuses and reacts. However, this model, being a first step, oversimplified the state of air voids in pavements by assuming atmospheric air pressure throughout the air voids, a single air pore channel diameter, and uniform air spacing of pores throughout the pavement.

Because oxygen concentration in pavements is highly dependent on the pavement air void structure (air void size and distribution), characterization of air voids is important in developing and validating an accurate model for calculations. The goal of this chapter was to develop a more realistic computational oxygen transport and reaction model with a more realistic representation of actual pavement air void structures to model transport through the air voids and within the asphalt-aggregate matrix and to use these elements to calculate a layer-by-layer bulk asphalt binder oxidation rate and total asphalt binder oxidation rate.

In this work, vertical transport through an air void channel and horizontal transport and reaction within the asphalt-aggregate matrix layer associated with an air void channel were modeled, a layer-by-layer bulk asphalt oxidation rate of pavement were calculated with careful characterization of pavement air voids.

Materials and Methodology

Overview of Experimental Design

The work for this enhanced model included modeling vertical transport through an air void channel, modeling horizontal transport and reaction within the asphalt-aggregate matrix layer associated with an air void channel, characterizing pavement air voids, and using these elements to calculate a layer-by-layer bulk asphalt binder oxidation rate.

Methodology

X-ray CT Imaging Technique

X-ray computed tomography (CT) imaging was used to investigate the air void characteristics and structure of pavement core specimens. It is ideal for non-destructively studying the interior of opaque solid objects. Two dimensional images, most commonly known as "slices," can be obtained using this process. Each slice reveals the interior of the object on a plane. If stacked together, the slices build a three dimensional image of the object. These slices are generally about 1-mm thick.

The X-ray system is composed of an X-ray source, a sample holder, and a detector, as demonstrated in the schematic in Figure IV-1 along with a grey-scale image. Basically, an X-ray source emits a beam of known intensity through the specimen, and a detector on the opposite side of the specimen measures the attenuated beam intensity. The specimen rotates 360° with respect to its center, an image is produced from the different density measurements that are registered, and these measurements are represented by a grey-scale. Then the specimen moves at a specific fixed vertical interval to enable evaluation of the entire specimen volume by vertical slices. The whole procedure is repeated once again to produce the next image until the entire solid is scanned.

X-ray CT Image Processing

The original grey-scale images obtained from X-ray CT are converted to black and white by the spreadsheet macro with a user-input threshold, where black areas represent the voids and white areas represent the aggregates and the mastic. The appropriate user-input threshold parameter was chosen between 0 and 56,000. By matching the air void content obtained from X-ray CT imaging with the air void content obtained from experimental measurements (Corelok method), an appropriate threshold

was obtained. The areas of the original images were converted to black (voids phase) if the gray intensity of the areas were less than the indicated threshold, and the areas were converted to white if the intensities were higher than the threshold (aggregate and mastic phase).

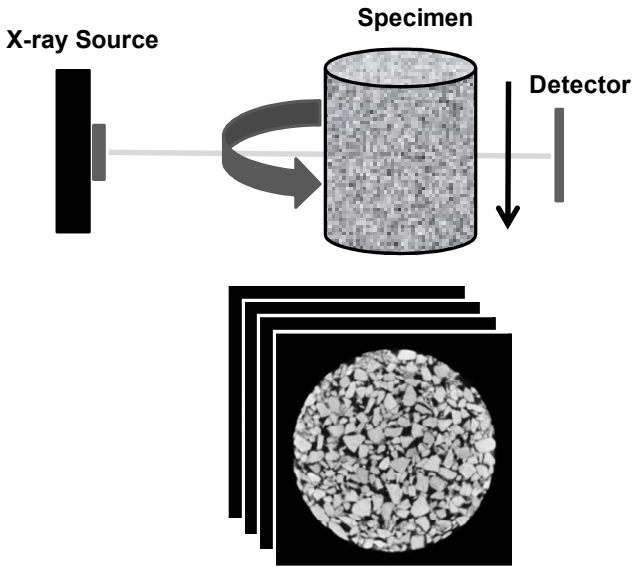

Figure IV-1. Schematic of X-ray CT System and Grey-Scale Images Obtained

Interconnected air voids are the air void channels that connect from the top to the bottom of specimens. To determine the interconnected air void content and distribution, stacks of images at different depth increments of the specimen were collected, and these black-and-white images were converted to binary bit files by macros developed by Masad et al.[27] These binary files then were analyzed to determine the connected paths from the top to the bottom of the specimen using a FORTRAN-built algorithm. Then the interconnected air void content of these images was calculated.

The images obtained after each image analysis steps is demonstrated in Figure IV-2. In sequence, they are the original grey image of a pavement specimen slice obtained with X-ray CT (a), the black-and-white image of all the air voids in the slice

after image processing (b), and the black-and-white image of interconnected air voids in the slice after image processing (c).

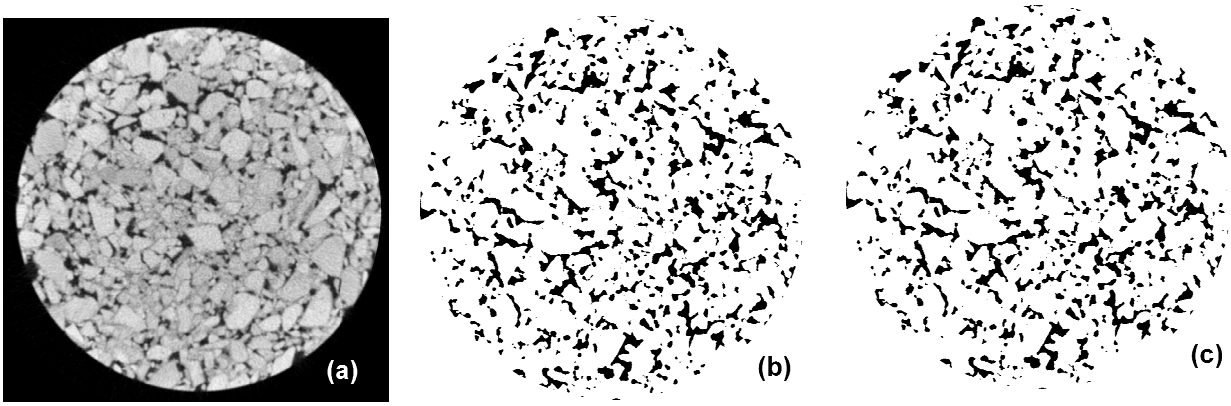

Figure IV-2. X-ray CT Image Analysis. (a) Original Gray-scale Image; (b) Black-and-white Image after Threshold; and (c) Black-and-white Image of Interconnected Air Void

Then black-and-white images of all the air voids or interconnected air voids for a pavement specimen slice were analyzed with image analysis software, Image J, to obtain statistically the air void size and number of air voids for this specimen slice. There is a built-in function in Image J to analyze particle size and number of particles in an image with proper calibration between actual image size and pixel of the image.

Air Void Measurements with CoreLok

The air void content of the specimens must be measured to provide the necessary calibration of the original grey-scale images obtained from X-ray CT scanning. In this work, the CoreLok® method was used to determine the total air voids and the accessible air voids (those that water can penetrate when the CoreLok® vacuum bag is opened underwater) from bulk specific gravity and maximum specific gravity measurements of

the core specimens. The details of such measurements have been described in several reports. [6, 35, 36, 37]

Results and Discussion

Modeling of Oxygen Transport and Reaction in Pavements

Oxygen transport and reaction in pavements is described as two interlinked steps, as demonstrated in Figure IV-3: 1) diffusion and/or flow of oxygen from the atmosphere above the pavement into the interconnected air voids in the pavement; and 2) diffusion of oxygen from those air voids inside the adjoining asphalt-aggregate matrix where it reacts with the asphalt binder. Further details of developing the enhanced model are described subsequently including transport through air void channels and transport and reaction within the finite asphalt-aggregate matrix layer associated with the air void channels.

Vertical Diffusion and/or Flow of Air Through the Air Void Channels

In pavements, diffusion and/or convective flow of oxygen must occur in order to supply oxygen to the interconnected air channels. From these channels, oxygen diffuses into and reacts within an asphalt-aggregate matrix. Accurately representing the oxygen concentration in those interconnected air channels is extremely important in modeling asphalt binder oxidation in pavements. This vertical oxygen transport process could occur by diffusion, when there is an oxygen concentration gradient between ambient air at the surface of the pavement and the oxygen concentration in the interconnected air voids, and/or by convective flow (for example, when air undergoes expansion or contraction with pavement temperature fluctuations); however, there are no direct measurements of such convective flow in pavements. In the case that oxygen transport is dominated by convective flow, it is fair to assume a constant 0.2 atm oxygen pressure in the interconnected air void channel, regardless of depth in the pavements, while in the

case that primary oxygen transport is by diffusion, the oxygen concentration decreases with depth below the pavement surface in the air void channel.

In this work, both situations are considered, giving two distinct and extreme oxygen concentration profiles in the air voids. One profile assumes pure diffusion from the pavement surface down into the air void channel; the other assumes constant oxygen pressure in these interconnected air voids (0.2 atm oxygen) when convective flow dominates. These two conditions establish a range, instead of a single value, of asphalt binder oxidation rates in pavements. The assumption of constant oxygen pressure at 0.2 atm in interconnected air voids gives the highest possible oxidation rate, while the assumption of vertical diffusion produces the lowest oxidation rate.

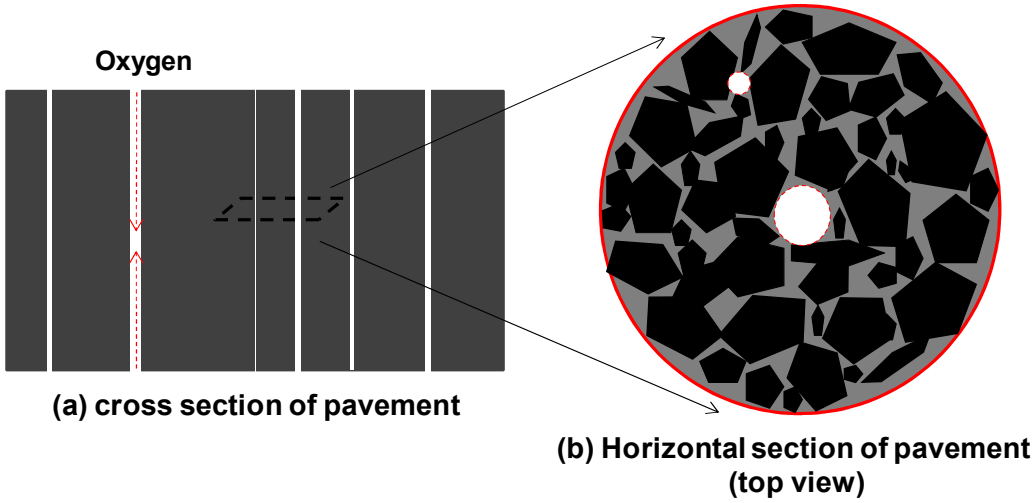

Figure IV-3. Schematic of Two Steps Involved in Oxygen Transport and Reaction in Pavements

In the case of oxygen transport through the pores by diffusion only, the oxygen concentration through the air voids needs to be determined. The oxygen concentration gradient is influenced by the air void size (diameter d), the distance oxygen must diffuse below the surface (z), the consumption rate of oxygen inside the adjoining asphalt-

aggregate matrix (r_{O2}), and the oxygen diffusivity in air ($D_{O2\text{-}Air}$). Considering that the diameter of the air voids is much smaller than the diffusion distance below the pavement surface, the oxygen concentration gradient in the radial direction of the pore is neglected in this work. Therefore, the oxygen concentration in an air void channel is a function of z only. With these assumptions, the oxygen partial pressure in an air void channel as a function of time and distance from the surface in a cylindrical coordinate system is given in Equation IV-1 as:

$$\left(\frac{\partial P}{\partial t}\right) = D_{O2-\text{Air}}\frac{\partial P}{\partial z} + A * r_{O2} \qquad \text{(IV-1)}$$

The boundary and initial condition are defined as:

$$\left(\frac{\partial P}{\partial z}\right) = 0 \quad \text{at} \quad z = \text{half of the pavement depth} \quad \text{(BC1)}$$

$$P = 0.2 \quad \text{at} \quad z = 0 \quad \text{(BC2)}$$

$$P = 0 \quad \text{at} \quad t = 0 \quad \text{(IC)}$$

where, $D_{O2\text{-}Air}$ is oxygen diffusivity in air where a constant value of 0.2 cm^2/s is used. A is the ratio of the area of the finite aggregate-asphalt matrix where oxidation occurs and the cross-sectional area of the air void channel. In this work, it was assumed that both the pavement top and bottom are exposed to ambient air, so that a non-flux boundary condition is defined at half the distance from the pavement surface to the pavement bottom. Ambient air at the bottom of the pavements is assumed because asphalt pavement base is rather porous and ambient air can easily get access to it from the underground water table or from the sides of pavements.

The term r_{O2} in Equation IV-1 is introduced because while oxygen diffuses throughout an air void channel, it is also continuously being consumed by the adjoining asphalt binder-aggregate matrix; this lumped-parameter model distributes that

consumption evenly across the pore cross section rather than calculating it as transport from the pore at the pore surface. This oxygen consumption rate can be calculated with the horizontal diffusion and reaction model that is developed in the following section with known oxygen pressure in the air voids and asphalt binder kinetics. A maximum oxygen consumption rate was used to calculate oxygen concentration gradient in an air void channel in this study. This maximum consumption rate was estimated by using asphalt binder oxidation kinetics parameters and the assumption of a constant oxygen pressure of 0.2 atm in an air void channel.

Figure IV-4 shows a sample calculation of oxygen concentration profile from the pavement surface to 0.25m below the surface. This air void channel has a diameter of 0.5 mm, shell thickness of 2 mm, and a length (depth) of 1 m. The asphalt binder used in the calculation is SEM 64-22. Two conditions (the one with oxygen transport by diffusion only in a pseudo steady state, and the one with ample convection through the pore) are established as a function of pavement depth, which can provide upper and lower limits for oxygen concentration in interconnected air voids at a specified depth. The assumption of a rapic resupply of air by convective flow established the upper limits, a constant oxygen pressure at 0.2 atm throughout the air void channel that is independent of depth in pavement. The assumption that oxygen transport occurs by diffusion only provided the lower limit, a decreasing oxygen concentration from the surface of the pavement.

Upper and lower limits of oxygen concentrations for a pavement layer can then be easily read from the plot and used as inputs to calculate binder oxidation rates in the finite volume of asphalt-aggregate matrix layer associated with this air void channel based on the horizontal diffusion and reaction model developed in the next section.

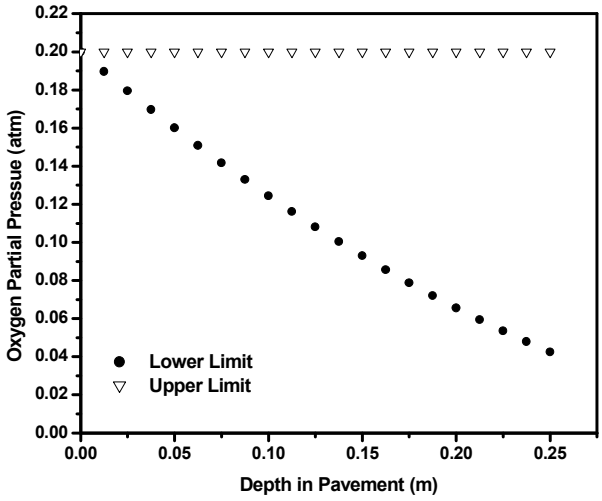

Figure IV-4. Sample Calculation of Oxygen Concentration Profile in an Air Void Channel at Two Limit Conditions

Horizontal Oxygen Diffusion and Reaction

From each air void channel, oxygen diffuses and reacts throughout the surrounding asphalt-aggregate matrix. The following accounts for the oxygen diffusion and reaction in a differential volume of the matrix:

$$\left(\frac{\partial C_{O_2}}{\partial t}\right) = -\nabla \cdot N_{O_2} - r_{O_2} \qquad \text{(IV-2)}$$

With Fick's first law of diffusion, a governing equation with boundary conditions could be used to estimate oxygen partial pressure throughout the matrix layer. The partial differential equation (PDE) is solved for the oxygen partial pressure as a function of time and distance away the from the air void-matrix interface in a cylindrical coordinate system, including oxygen consumption by reaction and binder hardening

(which decreases diffusivity) as a result of the oxidation. The resulting primary equation for the transport and reaction of oxygen in the asphalt-aggregate matrix is:

$$\left(\frac{\partial P}{\partial t}\right) = \frac{1}{r}\frac{\partial}{\partial r}\left(r\mathcal{D}_{O_2}\frac{\partial P}{\partial r}\right) - \left(\frac{cRT}{h}\right)r_{CA} \qquad \text{(IV-3)}$$

$\left(\frac{\partial P}{\partial r}\right) = 0$	at	$r = r_{NFB}$	No Flux Boundary
$P = P_{av}$	at	$r = r_{PS}$	Air Void Surface
$P = 0$	at	$t = 0$	Initial Condition

where, h is the Henry's law constant; c (a conversion factor from oxygen partial pressure units to concentration units in the asphalt binder) is asphalt binder dependent, ranging from 2.75×10^{-4} gmol O_2 /mL/CA to 4.59×10^{-4} gmol O_2 / mL/CA for ten asphalt binders reported.[56] In this study, an average value of 3.71×10^{-4} was used. r_{NFB} is an average distance between air voids, and P_{av} is the oxygen partial pressure in the air voids that is a function of distance in the air void channel from the atmospheric end and is calculated using the diffusion or convection flow model in the first modeling step of vertical transport, as appropriate. r_{CA} is carbonyl growth rate as described using an Arrhenius expression for temperature variation and pressure dependence following Equation I-1.

$\mathcal{D}_{O_2}$ can be expressed in terms of position (r), time (t), and pressure (P) with the following relationships: 1) oxygen diffusivity is a function of low shear limiting viscosity η_0^* (aging level) and temperature according to Equation III-12; 2) low shear limiting viscosity of asphalt binders is related to carbonyl content for asphalt binders according to Equation IV-4:

$$\eta_0^* = \exp\{HS \cdot CA + m\} \qquad \text{(IV-4)}$$

where, *HS* is asphalt binder hardening susceptibility and *m* is an experimental parameter. *HS* and *m* are functions of temperature and can be measured experimentally. Carbonyl content, *CA*, can be represented by Equation IV-5:

$$CA(t) = \int_0^t r_{CA}\, d\theta + CA_0 \tag{IV-5}$$

where, CA_0 is an integration constant determined from experimental data and r_{CA} can be calculated for an asphalt binder with known reaction kinetic parameters. Combing Equations IV-4, IV-5, and III-12; $\mathcal{D}_{O_2}$ is expressed as a function of position, time, and oxygen pressure.

Then, all the variables in Equation IV-3 are a function of position (*r*), time (*t*), and pressure (*P*). With defined boundary conditions and initial condition, oxygen pressure and oxidation rate are numerically solved for a finite asphalt-aggregate matrix layer associated with an air void channel. Asphalt binder oxidation and hardening kinetic parameters required in this calculation are measured from separate experiments.

Sample Calculation of Oxidation Rates for a Finite Volume Associated with One Air Void Channel

With the developed mathematical model, oxidation rates inside the finite aggregate-asphalt matrix associated with an air void channel at different depths in a pavement are calculated, as shown in Figure IV-5. Here, pavement layers at 0.02, 0.08, and 0.16 m are selected. Input for this calculation includes kinetics parameters of asphalt binder SEM 64-22, a value of air void radius of 0.5 mm, a value of shell distance of 5 mm, pavement temperature profiles calculated at Lufkin, Texas, for 1994, and calculated oxygen concentration profiles P_{av} (both upper and lower limits) in the air void channel as a function of depth. Output from the model calculation is the growth of carbonyl content in these three finite asphalt-aggregate matrix layers associated with the air void channel for the entire one-year period. At each depth, two carbonyl growth curves are generated;

one gives the highest oxidation rate, obtained from the upper limit of oxygen concentration in the air void channel (a constant 0.2 atm oxygen pressure) and the other provides the lowest carbonyl growth rate, calculated from the lower oxygen concentration limit in the air void channel.

The effect of pavement temperature on oxidation is clearly shown by comparing the highest or lowest carbonyl growth rates at these three depths. Pavement temperature at the pavement surface has the largest daily temperature fluctuation and the highest average pavement temperatures. Therefore, it is not surprising to see that the yearly oxidation rate is highest at the surface. Then it decreases deeper into the pavement structure because of decreasing daily temperature fluctuations that is coupled with the exponential reaction activation energy effect. In addition, the model results show that asphalt binder oxidation rates in the pavement were rather slow during spring and winter, and increased significantly during the summer due to higher pavement temperatures, as would be expected.

Also observed from model calculation is the effect of the oxygen pressure in the air void channel on oxidation rate. In general, the calculated oxidation rate is lower for the lower oxygen concentration values (due to the diffusion resistance) at each depth compared to the oxidation rate calculated at the higher oxygen pressure (0.2 atm oxygen throughout the air channel). At 0.02 m below the surface, there is a slightly reduced oxidation rate when the lower limit of oxygen concentration is used; and this reduced rate is more evident at deeper pavement depths where oxygen pressure in the air channel is further reduced by diffusion resistance.

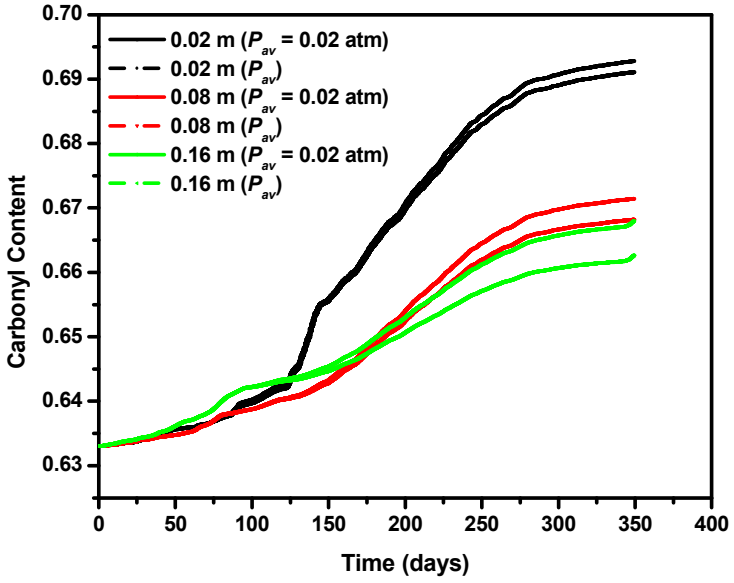

Figure IV-5. Sample Calculation of Carbonyl Growth for an Air Void Channel as a Function of Depth of Pavement Layers

Sensitivity of Air Void Parameters in the Model

The model calculation described used one set of values for the air void size and shell distance model parameters, while the actual air voids in pavements exhibit a large size distribution. The influence of air void size and shell distance on the final calculation was analyzed by changing their values over a practical range while keeping other input parameters constant.

As shown in Figure IV-6, with increases of air void radius from 0.1 mm to 3 mm while holding shell distance a constant, 5 mm, oxidation rates increase significantly from 0.041 to 0.057 CA/ year, suggesting that the air void radius is important in the model calculations.

For asphalt shell distance, while holding air void radius at a constant of 0.5 mm, increases in the shell distance lead to a rapid decrease in oxidation rate, as shown in Figure IV-7. As the shell distance increases, the oxidation rates tend to approach a

constant, most likely because oxygen, consumed by reaction, can no longer penetrate deeper into the matrix.

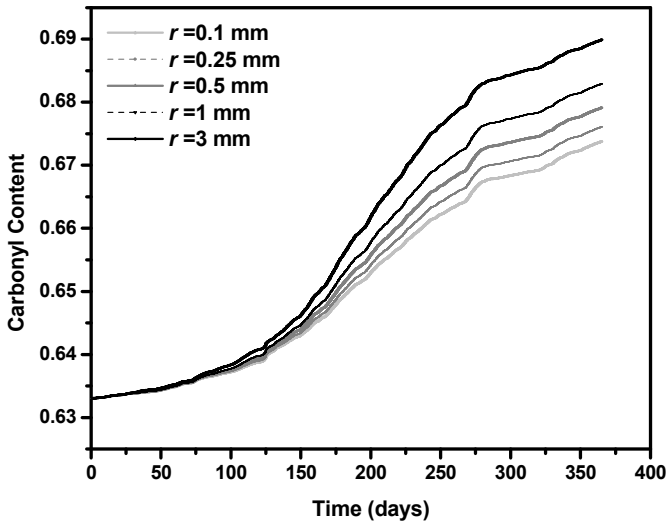

Figure IV-6. Effect of Air Void Radius on Yearly Carbonyl Growth Calculated

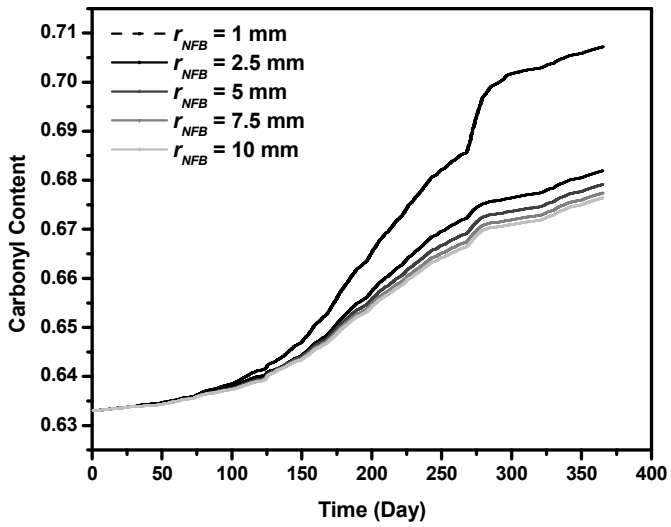

Figure IV-7. Effect of Shell Distance on Yearly Carbonyl Growth Calculated

From these Figures, IV-6 and IV-7, it seems that the model is rather sensitive to air void radius and shell distance. Because air voids in the pavement have a wide size distribution, characterization of air voids and acquisition of representative air void parameters for use by the model is very important to assure accurate model estimates of asphalt binder oxidation in pavements.

Pavement Air Void Characterization

The modeling effort described reviously calculates oxidation rates for a finite asphalt binder-aggregate matrix layer associated with an air void channel based on model parameters, including air void radius and shell distance. Considering the large variation of air voids in a pavement or pavement layer, characterization of air voids is essential to obtaining accurate bulk oxidation rates. This section addresses how to characterize air voids in pavement in order to acquire representative values for these air void parameters.

Air Void in Pavements — Characterization with X-ray CT

Air void structure in pavements has been assessed with X-ray CT and image analysis techniques to examine the internal microstructure of asphalt concrete mixtures, including air void distribution and interconnectivity. The detailed information and procedure has been described in the methodology. The final images after the imaging process are black-and-white images of total and interconnected air voids for each slice of the pavement core specimen.

A macro in image-J to analyze particle size and to count particle number is used to quantify the air void distribution from these final black-and-white images from X-ray CT. Information obtained from this analysis is the number of air voids and size of each air void, from which radius and shell distance for each air void channel can be estimated. Figure IV-8 shows a sample air void size distribution obtained from this analysis for one

image slice; air void size, in this particular slice, varies largely from 0.2 to 3 mm. The total number of air voids counted was 336.

Image slices at different depths of the pavement core specimen provide air void size distribution and number of air voids as a function of depth. A pavement specimen of US82 EBS (east bound shoulder) was used as a demonstration. The 2-inch pavement core was divided into four, half-inch (0.0125m) layers, starting at the pavement surface. The air void size distribution and number of air voids for each layer was analyzed and compared to the other layers. Figure IV-9 shows that the air void size distributions for the various layers are quite similar to each other. This conclusion holds with other pavement core specimens studied as well. Detailed air void size distribution for other studied pavements in shown in Appendix B1.

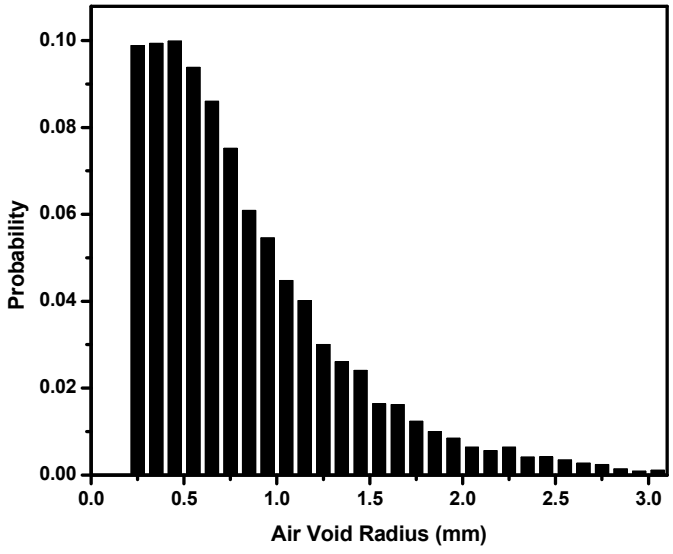

Figure IV-8. Sample Statistical Distribution of Air Void Size in a Pavement Layer of Pavement US82

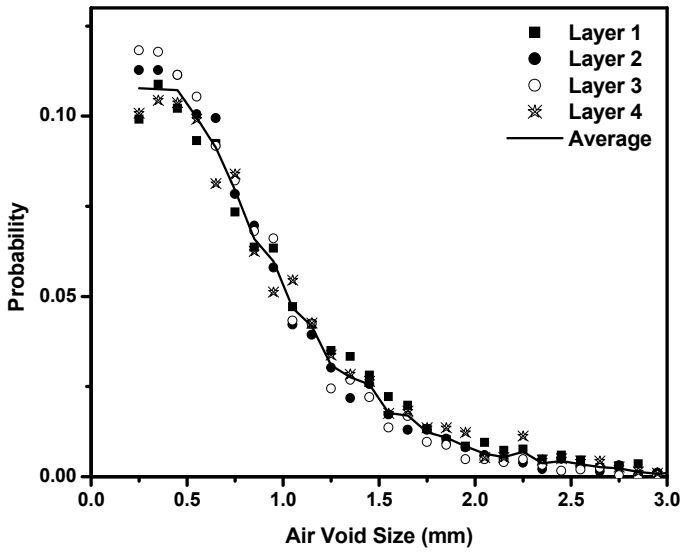

Figure IV-9. Air Void Distribution at Different Layers of Pavement US82

However, there are some significant differences in the number of air voids in each layer. The number of air voids were 336, 259, 227, and 276 for layers 1 to 4. It has been observed that air void content varies with depth in pavements, resembling a half "C" shape for field core and a "C" shape for lab compacted asphalt concrete specimen with higher air void content at the top of the specimen. Data from this work on the number of air voids in each layer agrees with this "C" shape distribution; This "C" shape distribution probably is due to the restriction imposed by the top and bottom surfaces during compaction.

X-ray CT Resolution Limit and Interpolation of Complete Air Void Distribution

One critical issue encountered when using X-ray CT for pavement air void analysis is undetected air voids with sizes smaller than 0.2 mm due to the resolution limit. The resolution of X-ray CT is affected by several factors such as the type and size of the X-ray source and detectors; the distance between the source, the solid, and the

detector; and the method used for image reconstruction. The images of the pavement specimens were taken at a resolution in the range of 0.146 to 0.195 mm/pixel that is also the detection limit. Consequently, for the X-ray CT images, there is a clear cut-off size near 0.2 mm; below this size, there are no air voids detected and this phenomenon is seen in Figure IV-8. However, this apparent minimum air void size most likely is not correct in reality.

To obtain a complete profile of air void distribution that cannot be fully measured by X-ray CT, distribution functions (probability density functions) may be used to predict the complete air void size distribution with the available size distribution measured with X-ray CT as an input. The ideal probability density functions were determined by plotting the pore size cumulative probability versus the cumulative probability of a test distribution using statistical packages. If the distribution of the data matched the test distribution, the data points should cluster around the equality line. According to the probability plots, there were two distributions that fit the data the best, Lognormal and Weibull distributions. Figure IV-10 shows an example of the probability plots for a pavement specimen using the Weibull and log-normal distributions. Log-normal density functions were used thereafter for the analysis.

The probability density function of a log-normal distribution is:

$$f(x;\mu,\sigma) = \frac{1}{x\sigma\sqrt{2\pi}} e^{-\frac{(\ln x-\mu)^2}{2\sigma^2}}, \quad x > 0 \qquad \text{(IV-6)}$$

where, μ and σ are the mean and standard deviation respectively of the variable's natural logarithm. By definition, the variable's logarithm is normally distributed. The location parameter μ can be any real number whereas the scale parameter σ can only be a positive real number. This type of distribution is commonly used to model continuous random data when the distribution is thought to be skewed. It has been shown that air void distribution in pavements might also follow such a distribution. [29, 58]

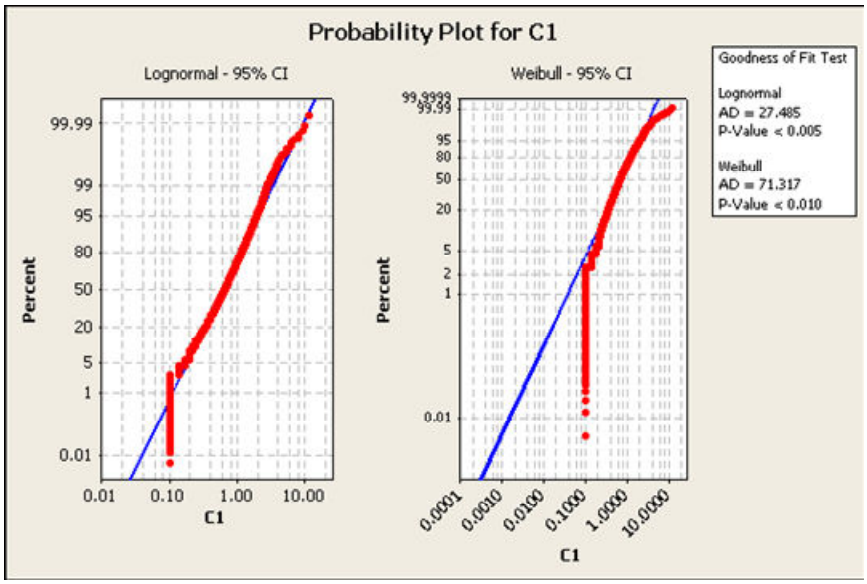

Figure IV-10. Example of Air Void Probability Plot for an Asphalt Pavement Specimen: Log-normal Distribution and Weibull Distribution

Measured size distributions of air voids, though incomplete, provide enough data to estimate lognormal distribution parameters, and then with those parameters, the entire distribution profile can be developed under the assumption that this distribution holds below the X-ray CT minimum resolution. Figure IV-11 provides a sample air void distribution obtained from a log-normal distribution with function parameters determined by analyzing the measured air void size distribution. Although the modeled air void distribution does not match exactly the measured air void distribution, overall it works pretty well. The use of log-normal distribution has also been validated with several other pavements, as shown in Appendix B2. A complete air void size distribution and the actual total number of air voids are thus estimated by using this log-normal air void distribution.

This complete profile of air void size distribution shows that the actual number of air voids in the range from 0 to 0.2 mm (area under the distribution curve from 0 to 0.2 mm as a fraction of the total area) is small; 7 % in this specific case. In practice, in the absence of statistical packages, it is reasonable approximation to draw a straight line in

between point zero and the data point measured at 0.2 mm to use as a substitution of the air void distribution in that range.

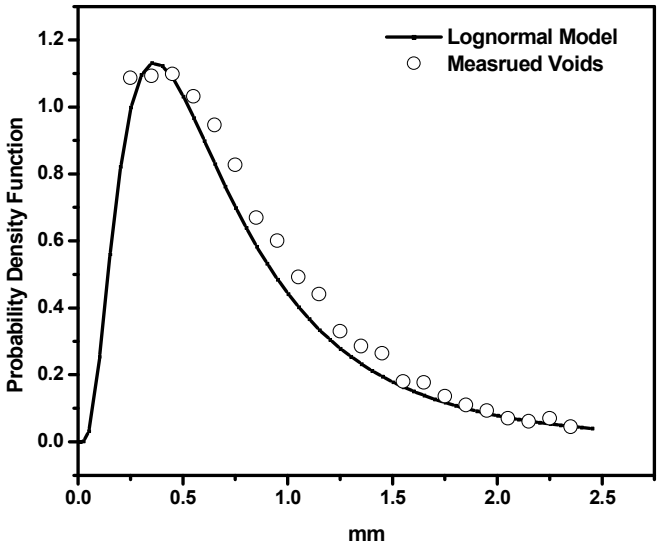

Figure IV-11. Sample Calculation of Air Void Distribution with a Log-normal Distribution Function

Calculation of Layer by Layer Bulk Oxidation Rates

The developments discussed using the X-ray CT technique and imaging analysis tools provide information on air voids size distribution and the number of air voids, for each pavement slice. From this information, air void parameters (air void radius and asphalt binder shell radius) for oxidation models can be estimated. The air void radius for each air void is directly obtained from image analysis, while with the total number of air voids known, the average shell distance for each pavement is used as the shell distance for each air void in the model calculations:

$$r_{NFB} = \frac{\text{Actual area of a pavement slice}}{\text{Number of air voids in this slice}} \quad \text{(IV-7)}$$

Theoretically, with a known air void radius and shell distance for each air void channel in a pavement layer, the oxidation rate for every finite aggregate-asphalt matrix volume associated with an air void channel in the layer can be computed to obtain the bulk oxidation rate. However this calculation takes too much computational effort and time. For a pavement layer with 1000 distinguishable air voids, we need to calculate 1000 calculations are required to get oxidation rates for every volume associated with each air void, which will take about 100 days to complete. To reduce the computational effort, air void sizes were divided into several ranges in this study, from 0 mm ~ 0.2 mm, 0.2 mm ~ 0.5 mm, 0.5 mm ~ 1 mm, 1 mm ~ 2 mm, and 2 mm ~ 3 mm. For each size range, the average air void radius (r_i) and the number of air voids (N_i) is determined; this information is then used by the model, along with shell distance ($r_{NFB,i}$), to calculate representative oxidation rates for air voids in this size range. The bulk oxidation rate for a pavement layer will be the sum of oxidation rates per unit volume calculated for each size range:

$$r_{O2}(\text{total}) = \sum_{i=1}^{n} \frac{r_{O2}(i) * N_i}{N} \quad \text{(IV-8)}$$

where, N_i is number of air voids in each size range, $r_{O2(i)}$ is the oxidation rate calculated for this size range, and N is the total number of air voids.

Figure IV-12 shows a schematic layout of the model structure with essential elements for this calculation. For a payment layer at depth d in a given pavement, the pavement temperature at this depth [$T(t, d)$] is first calculated as a function of time based on the pavement temperature model developed in Chapter II. In the meanwhile, X-ray CT scanning of a pavement core specimen is performed, and processed X-ray CT images at depth d are obtained to analyze the air void size distribution and the number of air voids from which an average air void radius (r_i), number of air voids (N_i), and shell distance ($r_{NFB,i}$) are obtained for each size range.

For each air void size range, there is an air void radius (r_i) and shell distance ($r_{NFB,i}$) pair. The vertical transport model is applied to this air void radius (r_i) and shell

distance ($r_{NFB,i}$) pair to generate the lower limit of P_{av} profile as a function of depth. As discussed in the vertical diffusion modeling section, an upper limit profile and a lower limit profile of P_{av} is defined depending on the oxygen transport behavior in interconnected air voids (diffusion versus convection). From the profiles, lower limits of P_{av} values at depth d are determined.

Combining the pavement temperature profile at d, X-ray CT air void size and spacing characterization, upper and lower P_{av} values as a function of air void parameters, plus oxidation and hardening kinetics and diffusion parameters for the asphalt binder used in the pavements, the horizontal diffusion and reaction model was used to calculate a range of probable oxidation rates as a function of depth d and air void parameters.

Thus, a bulk oxidation rate of this pavement layer was estimated with Equation IV-8 based on calculated oxidation rates for each air void size range and number of air voids in each size range.

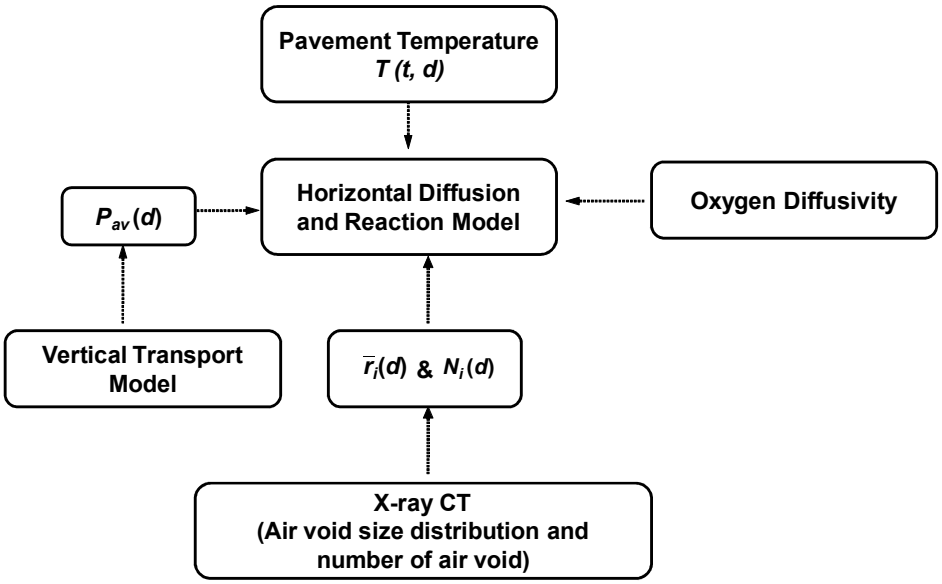

Figure IV-12. Schematic Layout of the Model Structure to Calculate Oxidation Rate for a Pavement Layer

Sample Calculation of Oxidation Rates of Pavement US82 at Lubbock, TX

To demonstrate the calculation process further, yearly oxidation rates as a function of depth for US82 in Lubbock, Texas, were calculated. Four pavement layers at depth of 0.01, 0.02, 0.03, and 0.04 m were selected. The asphalt binder used for this pavement is Alon 76-22; oxidation and hardening kinetics of this binder were obtained from separate experiments prior to use in the model.

To start with, yearly climate data at Lubbock, Texas, were collected and used as inputs for the pavement temperature model to calculate a one-year pavement history at each studied pavement depth. Figure IV-13 shows a sample calculation for a short summer period of pavement temperature calculated at several depths in the pavement. Here, daily temperature cycles for a period of 20 days are plotted. The amplitude of each cycle decreases with depth, with about a 10 ^{o}C difference in amplitude between the first layer at 0.01 m below the surface and the fourth layer at 0.04 m below the surface.

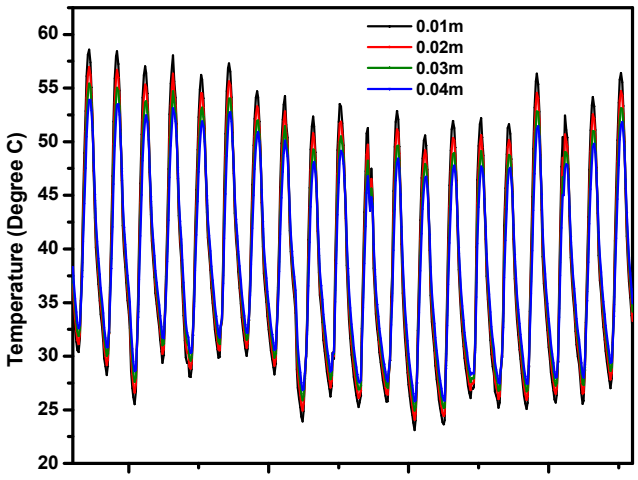

Figure IV-13 Pavement Temperature of US82 at Different Depths over a 20-day Summer Period (July 1st to July 20th, 1994).

Additionally, a surface layer of a two inch pavement core specimen was collected in the field and used for X-ray CT scanning and image processing. Final black-and-white

image slices of accessible air voids after image processing at each depth were analyzed for air void distribution and total air voids. From these measurements, an average air void radius (r_i), number of air voids (N_i), and shell distance ($r_{NFB,i}$) were determined for each pavement core layer and for each range of air void radius, as shown in Table IV-1~3. The air void ranges were from 0~0.2 mm, 0.2~0.5 mm, 0.5~1 mm, 1~2 mm, and 2~3 mm. Note that the average air void radius for each range does not show very much variation from layer to layer. However, both the number of air voids and the average shell distance show variations with depth and their values are interdependent.

Table IV-1. Average Air Void Radius Calculated for Each Air Void Range at Different Pavement Layers

Depth	Average Air Void Radius r_i (mm)				
	0~0.2 mm	0.2~0.5 mm	0.5~1 mm	1~2 mm	2~3 mm
0.01 m	0.140	0.351	0.727	1.360	2.377
0.02 m	0.142	0.350	0.722	1.358	2.400
0.03 m	0.144	0.348	0.725	1.337	2.306
0.04 m	0.141	0.351	0.720	1.361	2.405

Table IV-2. Number of Air Voids Calculated for Each Air Void Range at Different Pavement Layers

Depth	Number of Air Voids				
	0~0.2 mm	0.2~0.5 mm	0.5~1 mm	1~2 mm	2~3 mm
0.01 m	17	99	130	87	17
0.02 m	13	87	105	57	8
0.03 m	13	89	106	55	6
0.04 m	14	85	104	72	13

Then, with the air void radius (r_i) and shell distance ($r_{NFB,i}$) pair at each size range in each layer, a vertical transport model was used to calculate oxygen pressure profiles (P_{av}), both upper and lower limits, as a function of depth. P_{av} values at such corresponding layer are summarized in Table IV-4. The assumption of convection dominated transport process established the upper limits, a constant oxygen pressure at 0.2 atm throughout the air void channel that is independent of depth in pavement. The assumption of vertical oxygen transport through the pores by diffusion only provided the lower limit and a decrease of oxygen concentration away from surface of the pavement.

Table IV-3. Shell Distance Calculated for Each Air Void Range at Different Pavement Layers

Depth	Average Shell Distance r_{NFB} (mm)				
	0~0.2 mm	0.2~0.5 mm	0.5~1 mm	1~2 mm	2~3 mm
0.01 m	12.567	12.567	12.567	12.567	12.567
0.02 m	14.314	14.314	14.314	14.314	14.314
0.03 m	14.369	14.369	14.369	14.369	14.369
0.04 m	13.891	13.891	13.891	13.891	13.891

The amount that the lower limit P_{av} decreases with distance away from pavement surface varies according to the size of the air voids. According to the model calculations, for air voids ranging in size from 2~3 mm, there is practically no oxygen pressure drop in any of the layers. For air voids ranging in size from 0.5 mm to 1 mm, the oxygen pressure drops significantly from 0.2 atm at the surface to 0.198 atm at 0.01 m below the pavement surface, and to 0.192 atm at 0.04 m below the surface. For the smallest air void sizes, from 0~0.2 mm, oxygen pressure drops very significantly, from 0.2 atm at the surface to 0.14 atm at 0.01 m below the surface, and oxygen is completely depleted at 0.04 m below the surface.

This small pore versus large pore phenomenon is explained by considering the balance between oxygen transport through the pores and the oxygen consumption rate in

the adjoining asphalt binder-aggregate matrix. Because the oxygen flux by diffusion is theoretically independent of pore size, the larger pores, with their larger cross-sectional area, can supply oxygen at a higher rate than the smaller pores, while the oxygen consumption rate in the surrounding matrix stays largely the same for all sizes of air voids (as long as the shell distance is nearly the same). Thus, oxygen is more easily depleted inside smaller air voids than inside the larger ones.

Table IV-4. P_{av} Calculated for Each Air Void Range at Different Pavement Layers

		P_{av} (atm)				
Depth	**Condition**	**0~0.2 mm**	**0.2~0.5 mm**	**0.5~1 mm**	**1~2 mm**	**2~3 mm**
0.01 m	Upper	0.2	0.2	0.2	0.2	0.2
	Lower	0.141	0.192	0.198	0.199	0.200
0.02 m	Upper	0.2	0.2	0.2	0.2	0.2
	Lower	0.084	0.184	0.196	0.199	0.200
0.03 m	Upper	0.2	0.2	0.2	0.2	0.2
	Lower	0.030	0.176	0.194	0.198	0.200
0.04 m	Upper	0.2	0.2	0.2	0.2	0.2
	Lower	0.000	0.169	0.192	0.197	0.199

With a known pavement temperature profile, the upper and lower P_{av} values corresponding to an air void radius (r_i) and shell distance ($r_{NFB,i}$) pair, and the air void radius (r_i) and the shell distance ($r_{NFB,i}$) values themselves, the horizontal diffusion and reaction model was used to calculate a higher limiting oxidation rate and a lower limiting oxidation rate for air voids in each size range at a given depth. The bulk yearly oxidation rate for each pavement layer was also estimated with Equation IV-8 with known oxidation rates for each air void size range and number of air voids in each size range. Figure IV-14 shows the bulk carbonyl growth for the one-year period for these four studied pavement layers. Table IV-5 summarizes yearly oxidation rates calculated for each air void size range and the bulk oxidation rates for each layer.

The effect of air void size on oxidation rates is clearly observed. Taking layer 1 as an example, the highest oxidation rate increases from 0.0281 CA/year to 0.0394 CA/year with an increase of air void size range from 0~0.2 mm to 2~3 mm. Even though the air in the voids is assumed to be instantaneously resupplied by convection, the smaller pores must supply oxygen to a larger asphalt binder-aggregate matrix, thereby increasing the effect of diffusion resistance in this matrix. This difference becomes greater when the lowest oxidation rates are compared, in which case the effect of air void size on vertical diffusion is combined with the diffusion resistance in the asphalt binder (from 0.0256 CA/year to 0.0326 CA/year).

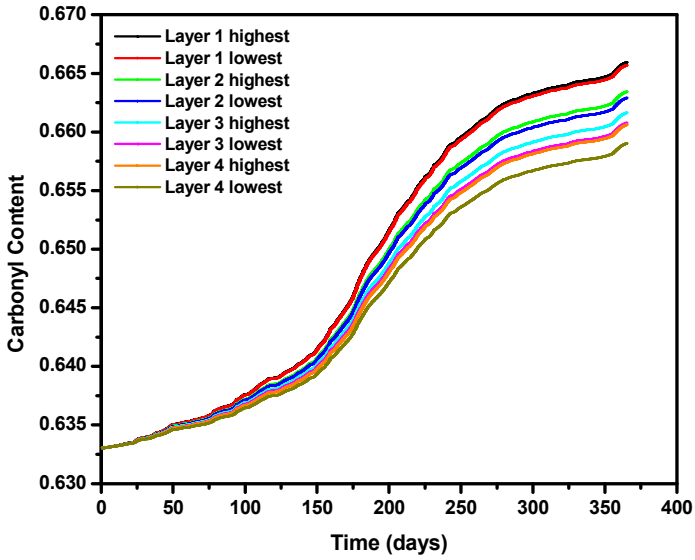

Figure IV-14 Bulk Carbonyl Growth Rates (Oxidation Rates) of US82 for One Year Period at Different Pavement Layers

The effect of pavement temperature on oxidation rates is observed by comparing oxidation rates calculated for a single air void size range or the overall bulk oxidation rates for the various pavement layers. Taking the overall bulk oxidation rates as an example, oxidation rates decrease with pavement depth, from 0.0329 CA/year at 0.01 m below the surface to 0.0276 CA/year at 0.04 m below the surface if the highest oxidation

rates are compared. In addition, the temperature effect also is shown in Figure IV-14, as the oxidation rates were slow during spring and winter, and increased significantly during the summer due to higher pavement temperatures, as would be expected.

Table IV-5. Oxidation Rates Calculated for Each Air Void Range at Different Pavement Layers

		r_{O2} (CA/year)					
Depth	**Condition**	**0~0.2 mm**	**0.2~0.5 mm**	**0.5~1 mm**	**1~2 mm**	**2~3 mm**	**Bulk**
0.01 m	Highest	0.0281	0.0301	0.0328	0.0359	0.0394	0.0329
	Lowest	0.0256	0.0297	0.0326	0.0359	0.0394	0.0326
0.02 m	Highest	0.0262	0.0281	0.0306	0.0335	0.0368	0.0304
	Lowest	0.0208	0.0275	0.0304	0.0335	0.0369	0.0298
0.03 m	Highest	0.0248	0.0266	0.0289	0.0317	0.0347	0.0286
	Lowest	0.0148	0.0256	0.0286	0.0317	0.0347	0.0277
0.04 m	Highest	0.0236	0.0253	0.0275	0.0302	0.0331	0.0276
	Lowest	0.0000	0.0241	0.0272	0.0301	0.0331	0.0259

The highest and lowest oxidation rates are shown in both Figure IV-14 and Table IV-5. Their values are calculated by using the upper and lower limits of P_{av} separately. In each pavement layer, because the difference the upper and lower limit of P_{av} is smaller for the larger air void sizes, and greater for the smaller air void sizes, it is not surprising to see that the highest and lowest oxidation rates calculated at the larger air void size are rather close, and their differences become more and more obvious with a decrease of air void size, as shown in Table IV-5. By contrast, for some air void sizes at different pavement layers, the lower limit P_{av} decreases away from pavement surface. So, the difference between highest and lowest oxidation rates becomes greater deeper into the pavement, as was observed in Figure IV-14 from the bulk oxidation rates.

Conclusions

Transport through an air void channel and transport and reaction within the asphalt binder-aggregate matrix associated with an air void channel were modeled separately to calculate an oxidation rate for an asphalt binder-aggregate layer associated with an air void channel with known air void radius (r_0) and shell distance (r_{NFB}).

To extend the model from one air void channel to entire pavements, pavement air voids were characterized with X-ray CT scanning and image analysis techniques. From it, three air void parameters, including air void radius ($r_{0,i}$), average shell distance ($r_{NFB,i}$), and number of air voids (N_i), were obtained, which are utilized in the model directly.

This oxygen transport and reaction model, along with known pavement temperature and asphalt binder oxidation and hardening kinetics, successfully calculates layer-by-layer asphalt oxidation rates in a pavement.

The importance of this study is to develop an improved oxidation model for predicting asphalt oxidation in pavements. Such a model is a critically important tool for pavement design and improvement and for maintenance scheduling.

CHAPTER V
MODEL VALIDATION WITH FIELD OXIDATION RATES

Introduction

Oxidation is an ongoing process throughout a pavement's service life and within the entire depth of the pavement.[6] The effect of asphalt binder oxidation in pavements can be very negative as far as pavement durability is concerned. With asphalt binder oxidation and subsequent hardening, pavements become less flexible and more susceptible to cracking under repeated traffic loading and severe environmental conditions.[5,6] The previous chapter developed a fundamentals-based oxygen transport and reaction model to predict asphalt binder oxidation rates in pavements with model elements including pavement temperature, air voids in pavements, asphalt binder oxidation kinetics, and oxygen diffusivity in asphalt binders. However, fundamental principles are not sufficient, calibration and verification of the pavement oxidation model is required.

Asphalt binder oxidation and hardening rates in pavements have been measured in several studies.[6,25,38] These measurements normally involve collecting pavement cores over time, cutting core specimen into thin slices, extracting and recovering asphalt binders in each slice, and measuring recovered asphalt binder properties including carbonyl content and viscosity. From these measurements, asphalt binder oxidation or hardening rates at different depths in a pavement is determined. Results from these studies suggest that asphalt binder oxidation rates in pavements is largely determined by the temperature as a function of time and position (depth) in the pavement, provided the accessible air voids are sufficiently high (4% or greater), and that when the accessible air voids in pavements are sufficiently low (2 % or less) the hardening rate of asphalt binders is significantly reduced. [6,38]

In this chapter, field oxidation rates for a number of pavements in Texas and Minnesota were measured and compared with model calculations to validate and further

improve the model if necessary. In addition, the effect of model elements including pavement temperature, air voids properties, and asphalt binder oxidation kinetics on field oxidation rates are discussed by comparing field oxidation rates at these different pavement sites.

Materials and Methodology

Overview of Experimental Design

Field oxidation rates for a number of pavements in Texas and Minnesota were measured and compared with model calculations to validate and further improve the model if necessary. In addition, the effect of pavement temperature, air voids properties, and asphalt binder oxidation kinetics on field oxidation rates are also discussed.

Materials and Pavement Validation Sites

Table V-1 summarized seven pavement sites selected in this study from Texas and Minnesota.

The Texas sites range from Amarillo in the north to Laredo in the south, and to the Lufkin in the east. Most of the field cores were taken from top surface layers of the pavements, but also from layers far below the surface on IH35 #5 in Waco and IH35 #4 in Laredo, specifically. IH35 #5 in Waco is a 4-inch rich bottom layer (high asphalt binder content), sited on 6-inches of flex base at a depth of 16 inch below the pavement surface. IH35 #4 in Laredo is a 2-inch rich bottom layer (high asphalt binder content) on 6-inches of flex base at a depth of 14 inch below the pavement surface. Here the number after the name of the highway indicates the pavement layers studied. Unless specified in Table V-1, the surface payment layer is used. The thicknesses of the various pavement layers ranged from 2 to 4 inches but. The Bryan district pavement (US290) contained unmodified asphalt binders, while other pavements are polymer modified. Oxidation and

hardening kinetics for all the asphalt binders were measured separately with either recovered binders from the field or the same binders obtained from the manufacturer. Additionally, IH35 #4 in Laredo had the lowest accessible air voids of 2.01%, while US290 in Bryan had accessible air voids as high as 12.44 %. Most of the other pavement layers had intermediate values from 5.86 % to 7.91 %. The ages of the pavements range from new construction (US277) to 6 years old (Amarillo US54) for the first coring date. Coring at two times allowed a calculation of the actual field oxidation rates.

Table V-1 List of Field Sites Studied

District (State)	Highway	Thickness (inch)	PG (modifier)	Binder Supplier	AAV (%)	Cons.	1st Coring	2nd Coring
Laredo (TX)	US277	2.5	70-22 (SBS)	Valero-C	7.27	2008	07/2008	09/2009
Lufkin (TX)	US69	2	70-22 (SBS)	Marlin	7.91	2003	02/2005	06/2008
Bryan (TX)	US290	2.5	64-22 (Un)	Eagle	12.44	2002	10/2005	08/2008
Waco (TX)	IH35 #5	3	70-22 (SBS)	Alon	5.86	2003	10/2005	08/2008
Amarillo (TX)	US54	2.5	70-28 (SBS)	Alon	7.33	1998	12/2004	07/2008
Laredo (TX)	IH35 #4	2	70-22 (SBS)	Valero-C	2.01	2007	--	06/2008
Metro Area (MN)	I-94	4.5	AC-120(Un)	--	4.81	1993	11/2004	11/2008

Cores also were included in the study from Cell 1 from the Minnesota Road test site in Minnesota. The thickness of the core layer is 4.5 inches, taken from the pavement surface. Oxidation reaction kinetic parameters were measured with recovered binders from the field. Accessible air voids content for this pavement layer was 4.81%. Cell 1 constructed in 1993, and cores were obtained from the MnRoad site in November of 2004 and in November of 2008.

This collection of pavement cores covers a large variety of key elements that affect pavement oxidation and provided data that could be used to assess the effects of pavement temperature (Texas versus Minnesota; surface layer versus bottom layer), air void properties (low accessible air voids of 2.01% versus high accessible air void of 12.44%), and asphalt binder oxidation and hardening kinetics (with a variety of asphalt binders) on measured or modeled oxidation rates.

Methodology

Cores taken from the field were analyzed for interconnected air voids (by X-ray CT) and total and accessible air voids (by CoreLok or SSD) first, and then sliced into 0.5-inch layers for binder extraction and recovery from each layers. The recovered asphalt binder were analyzed for oxidation by infrared spectroscopy (FT-IR) and for physical properties by dynamic shear rheometry (DSR) to provide data on asphalt binder oxidation and hardening rates in pavements. In addition, binders recovered from cores or similar asphalt binders from manufacturers (when core samples were not sufficient for kinetic measurement) were oxidized in pressure oxidation vessels (POVs) at controlled temperatures (3~5 temperatures) and pressure (1 atm air pressure) to measure oxidation and hardening kinetics of the asphalt binders.

X-ray CT Scanning and Image Processing

X-ray CT imaging were used to characterize air voids in the pavements. Final black and white images of total air voids and accessible air voids after image processing were quantified to get air void distribution and number of air void in each pavement slice, which were used as model inputs. Detailed information on X-ray CT techniques and image processing is reported in Chapter VI.

Air Void Measurement with CoreLok

Total air voids content and accessible air voids content of the cores were measured using the CoreLok® method. The details of such measurements have been described in several standards.35,36,37

Binder Extraction and Recovery

Extraction and recovery of the asphalt binder in the core specimens was conducted based on the procedures outlined by Burr et al. [59] These procedures provide for a thorough wash and therefore extraction of the asphalt binder from the aggregate but with minimal hardening or softening of the asphalt binder in the solvent and with care taken to assure complete solvent removal during the recovery process with a Rotovap device.[60,61] The extraction process uses washes in toluene followed by a 15 percent ethanol in toluene solvent mixture and size exclusion chromatography to assure removal of the solvent from the recovered asphalt binder.

Carbonyl Content Measurements with FTIR

FTIR measurement were conducted for recovered asphalt binders and also asphalt binders aged in POVs for kinetics studies. A Nicolet 6700 Fourier Transform Infrared Spectroscopy (FT-IR) spectrometer was used to analyze the carbonyl content. Growth in the area under the FTIR spectrum from 1650 to 1820 cm^{-1} in arbitrary units, the carbonyl area (CA), was used to monitor the progress of the asphalt binder oxidation.

Gel Permeation Chromatography (GPC)

After the asphalt binder was extracted and recovered, the GPC were used to ensure complete solvent removal.[59] Tests samples were prepared by dissolving 0.2 g of binder in 10 mL of Tetrahydrofuran (THF). The sample of interest was then sonicated to ensure complete dissolution. The sonicated sample was then filtered through a 0.45-µm syringe filter. Samples of 100 µL were injected into 1000, 500, and 50-Å columns in

series with Tetrahydrofuran (THF) carrier solvent flowing at 1.0 mL/min. Incomplete solvent removal results in a positive peak located at 38 minutes on the chromatogram.

Dynamic Shear Rheometer (DSR)

The rheological properties of the asphalt binder were determined using a Carimed CSL 500 controlled stress dynamic shear rheometer (DSR). The rheological properties of interest were the complex viscosity ηo* measured at 60°C and the storage modulus (G′) and the dynamic viscosity (η′), both measured at 44.7 °C and 10 rad/s in the time-sweep mode. A 2.5-cm composite parallel plate geometry was used with a 500-μm gap between the plates.

Asphalt Binder Oxidation and Hardening Kinetics Measurement

Knowing oxidation and hardening kinetic parameters of asphalt binders used in these field sites are essential for model calculations and evaluation of their impact on field oxidation rates. These parameters include activation energy, pre-exponential factor in the Arrenius equation of asphalt binder oxidation rate, and viscosity hardening susceptibility and m value in the linear correlation between carbonyl content growth and increasing of log low shear limiting viscosity.

Binders recovered from cores or similar asphalt binders from manufacturers were oxidized in thin films in pressure oxidation vessels (POVs) at controlled temperatures and pressure (1 atm air pressure). In the case where original asphalt binder and recovered asphalt binder were not available, interpolation strategies were used. Oxidation rates were measured at a minimum of three temperatures (60, 80, and 100 °C), and up to five temperatures (60, 70, 80, 90, 98 °C). From these data, activation energy and the pre-exponential factor were estimated. Additionally, zero shear limiting viscosity of each recovered asphalt binder at different oxidation levels (carbonyl content) were measured. From which, viscosity hardening susceptibility and *m* value (intercept) was obtained.

Table V-2 summarizes these oxidation and hardening kinetic parameters determined for each asphalt binder used in the selected pavement sites.

Table IV-2 Constant-rate Oxidation and Hardening Kinetic Parameters of Binders Recovered from Field Sites

Asphalt	Oxidation and Hardening Parameters			
	AP^{α} ln(CA/day)	E (kJ/Mol)	HS (1/CA)	m **(poise)**
Val-C 70-22 (US277)[a]	21.559	75.183	3.970	8.144
Marlin 70-22 (US69)[b]	24.783	84.841	6.890	3.940
Marlin 64-22 (US290)[a]	24.783	84.841	7.931	2.697
Alon 70-22 (IH35-Waco)[c]	22.399	77.512	4.490	6.758
Alon 70-28 (US54)[a]	21.686	54.947	4.950	7.409
Val-C 70-22 (IH35-LRD)[a]	23.044	72.970	7.550	4.970
AC-120 (I-94)[d]	22.289	77.411	3.290	5.513

a: Oxidation Kinetics parameters measured with recovered binders.
b: Oxidation kinetics parameters of base binder Marlin 64-22 were used, assuming polymer modification does not affect oxidation kinetics.
c: Oxidation kinetics parameters were interpolated from kinetics parameters of Alon 64-22 and Alon 76-22; Their AP^{α} and E of are21.905 and 76.256 for Alon 64-22 and 22.642 and 78.769 for Alon 76-22.
d: Average values of oxidation kinetics parameters from two separate measurements of oxidation kinetic parameters of recovered binders are used.

Results and Discussion

Measured Pavement Oxidation Rates in the Field

Oxidation of the asphalt binders in these pavements in the form of the carbonyl content growth is summarized in Figure V-1, showing the bulk carbonyl content of the recovered asphalt binder for each pavement core versus the corresponding service age.

Among the six pavements, distinct oxidation rates were obtained. Texas pavements on US277, US290, and US54 have relatively high oxidation rates from 0.0635 to 0.0935 CA/year, while Texas pavements on IH35-Waco and US69 and Minnesota pavement Cell 1 have low carbonyl growth rates of 0.0256 to 0.0334 CA/year.

At first glance, there appears to be a great deal of disorganization of the data. However, when considered in detail and evaluated from the perspective of the key elements that affect asphalt binder oxidation in pavements including pavement temperature, pavement air voids properties, and asphalt binder oxidation kinetics, the results are, in fact, quite consistent. Texas has higher pavement temperatures compared with Minnesota, it is expected that in general oxidation rates in Texas should be greater than in Minnesota. In fact, for a Texas pavement (US277) with slightly high air voids content and similar values of activation energy as compared Minnesota Cell 1, the oxidation rate is nearly two-fold that of Minnesota Cell 1. Oxidation rates for US290 is further accelerated by extremely high air voids content of 12.44%, and oxidation rates for US54 is increased by an exceptionally low value of activation energy of 54.95 kJ/mol.

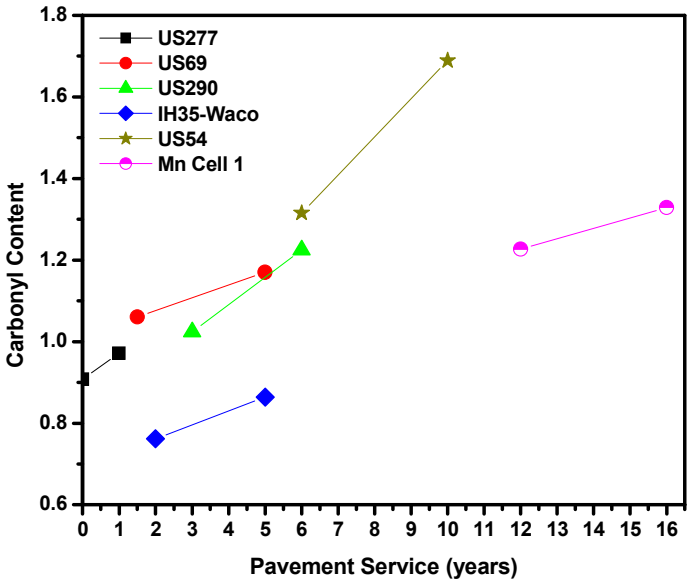

Figure V-1 Measured Oxidation Rates of Asphalt Binders in Various Pavements

Exceptions in Texas pavements are IH35-Waco and US69 that have oxidation rates comparable to Minnesota Cell 1. IH35-Waco is a 4-inch rich bottom layer that is 16 inches below the pavement surface. At this depth, the amplitude of daily temperature

fluctuation attenuates to a great deal that causes the oxidation rate to decrease drastically compared with that for surface layers. For US69, there is no apparent explanation of the low oxidation rate. The low oxidation rate is apparently caused by a combination of pavement temperature, air voids parameters, and asphalt binder oxidation kinetics.

Modeled Pavement Oxidation Rates in the Field

Although measured field oxidation rates provide some insights on variables that affect asphalt binder oxidation and values of asphalt binder oxidation rates in pavements, the data are not detailed enough to serve as a prediction model to pavement engineers. A fundamentals-based oxygen transport and reaction model for predicting asphalt binder oxidation in pavements was developed in Chapter IV. However, calibration and verification of the pavement oxidation model is required. In this section, pavement temperature, air void properties, and asphalt binder oxidation kinetics are carefully characterized for pavement cores (sites) listed in Table V-1 plus one additional pavement site of IH35-LRD, From these sites, yearly oxidation rates are modeled as a function of time and depths in the pavement cores.

The thickness of validation cores ranges from 2 to 4 inches. In this study, each pavement core was divided into 0.5 inch layers, and designated as Layer 1 (top layer), Layer 2, Layer 3 etc…. Representative pavement temperature (Chapter II), air void parameters (Chapter IV), and values of P_{av} (Chapter IV) for each core layer were determined and used to calculate oxidation rates for those pavement layers.

Temperature Profile for the Pavements

Climate inputs including hourly solar radiation, hourly air temperature, and daily wind speed in hourly format at these pavement sites were collected or interpolated. Annual pavement temperature profiles as a function of depth for these locations were generated using climate data inputs coupled with the pavement temperature prediction

model. Temperature history for the pavement core is a function of the depths in the core, and representative pavement temperatures for each 0.5-inch thick pavement layer are calculated with a given depth for each layer.

Figure V-2 shows a demonstration of the pavement temperature profile calculated for the top layer of the selected pavement cores for a period of 15 days in winter and summer. Annual temperature profile of these pavements as different pavement core layers is reported in Appendix C1.

As shown in Figure V-2, there is a great deal of difference in these temperature profiles for each pavement core in terms of daily temperature fluctuations and daily average temperatures. These profiles could be categorized into three groups: 1) Minnesota Cell 1, with daily average pavement temperature much lower than other pavements in winter and summer; 2) rich bottom layer of IH35-Waco and IH35-LRD, with nearly no daily temperature fluctuations in winter and slight fluctuations in summer; and 3) all other Texas pavements. Because pavement temperatures are heavily influenced by climate and depths in the pavements, it is not difficult to point out that the difference between Group 1 and other pavements is mainly caused by the cold climate in Minnesota, and that the difference between Group 2 and other pavements is induced by effect of depth in the pavement structure.

Even among the four Texas pavements in Group 3, there is also a significant variation of daily temperature fluctuations and daily average temperatures that follows climatic trend. Climates of these pavement sites change from dry-cold in Amarillo, to wet-warm in Lufkin, and to dry-warm in Laredo, with the climate in Bryan in the middle. Corresponding to that, US277 in Laredo has the highest daily average temperature with US69 in Lufkin second, while US54 in Amarillo and US290 in Bryan have relative lower daily average temperatures. A similar observation follows the daily temperature fluctuations.

The above discussion compares the temperature of the top layer of the selected pavement cores, and similar observation follow for comparison of temperatures of other

core layers. Of course, it is expected that daily temperature fluctuation decreases deeper into each pavement cores, while the average daily temperature do not change too much.

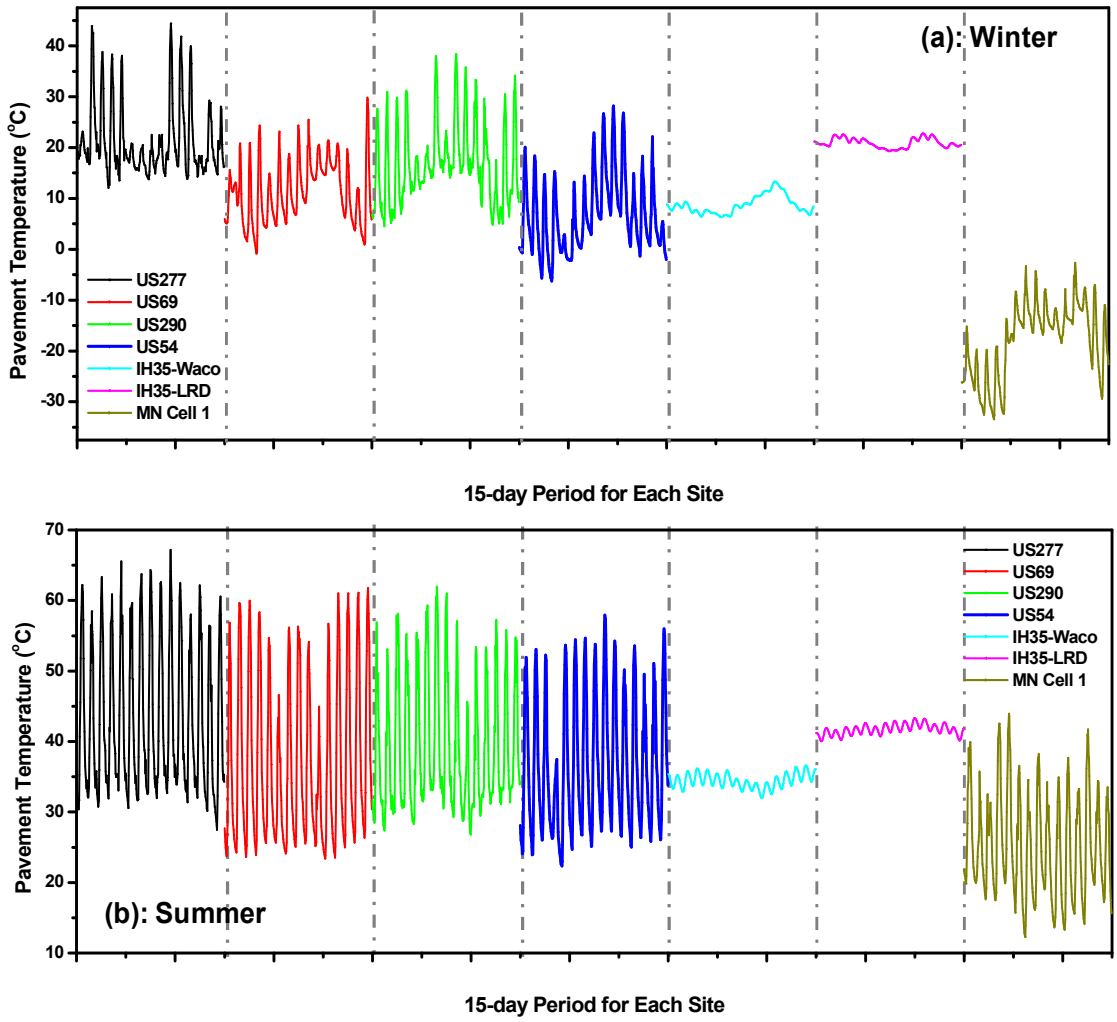

Figure V-2 Temperature Profiles of Top Layer of Validation Pavement Core at (a): Winter from January 15th to January 30th, 1994, and (b): Summer from July 1st to July 15th, 1994.

Characterization of Pavement Air Voids

Pavement cores were collected from these validation sites and scanned with X-ray CT for interior air voids structure. A sequence of grey scale images slices were generated with 1-mm intervals in depths. These original grey scale images were then converted to black and white images of total air voids after calibration and interconnected air voids after image processing. Figure V-3 shows a collection of representative black and white images of total air void after calibration.

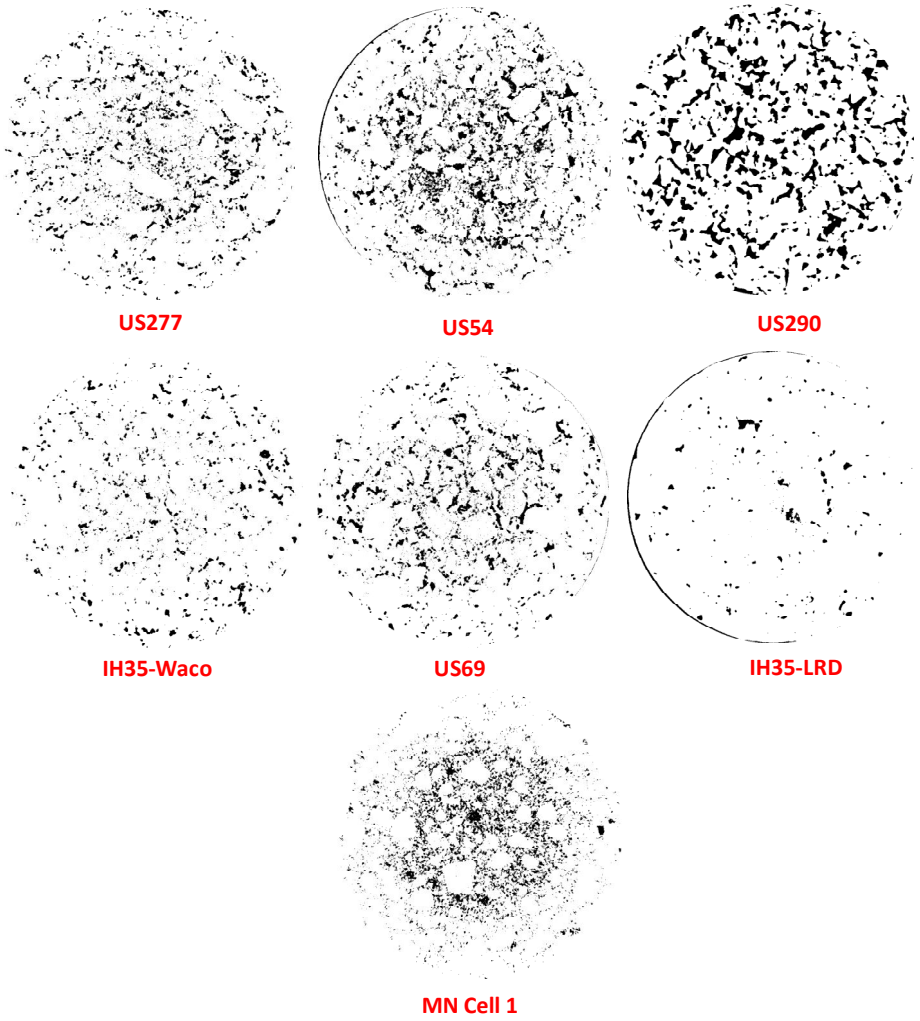

Figure V-3 Collection of Representative Images of Total Air Void for Each Field Cores

Each core does exhibit some unique air voids properties in terms of air void size, number of air voids, and air void distribution. For example, most of the air voids in the US290 field core have larger air voids than these in other pavement cores, while the number of air voids is less than most of the other cores; and air voids in the IH35-LRD field core are much less than in other field cores.

From these black and white images of total air voids, model required air void parameters including average air void radius (r_i), number of air voids (N_i), and shell distance ($r_{NFB,i}$) for each layer of field cores were determined following procedures described in Chapter IV. Images slices obtained in each 0.5-inch thick core layer were combined to analyze air void distribution and total number of air voids in such layer.

Table V-3 summarizes air voids parameters for the top layer of the selected pavement cores. It provides quantitative comparison of average air void radius (r_i) and number of air voids in each air void size range, shell distance (r_{NFB}), and total number of air voids of the selected pavement cores. More detailed air voids data for each pavement core at different pavement layers is reported in Appendix C2.

Table V-3 Summary of Air Void Parameters in the Top Layer of Pavement Cores

r_i (mm) / # *of AV*		US277	US69	US54	US290	IH35 (Waco)	IH35 (LRD)	MN (Cell 1)
AV Size (mm)	0~0.2	0.140/34	0.144/52	0.145/40	0.144/20	0.144/23	0.140/8	0.144/95
	0.2~0.5	0.332/672	0.336/407	0.332/436	0.352/92	0.340/309	0.350/80	0.327/909
	0.5~1	0.697/211	0.700/240	0.736/246	0.736/128	0.702/242	0.713/92	0.679/327
	1~2	1.338/83	1.342/84	1.359/117	1.414/129	1.305/85	1.308/31	1.336/97
	2~3	2.400/14	2.663/12	2.423/27	2.455/40	2.276/5	2.407/2	2.470/18
r_{NFB} (mm)		8.931	8.470	8.163	11.924	9.182	16.128	6.226
Total # of AV		1014	795	866	409	664	213	1446

As observed in Table V-3, air voids properties of each pavement core vary from one to another. Total number of air voids in these seven pavement cores changes from 213 for IH35-LRD to 1446 for Minnesota Cell 1, while average shell distance value changes from 6.226 to 16.128mm. There is also a noteworthy difference in air void size distribution among these cores. For example, the majority of air voids in US290 have radius larger than 0.5 mm, whereas in US277, the majority of air void radius fall between 0.2~0.5 mm.

This discussion is based on air voids in the top layer of pavement cores, and the dissimilarity of air voids properties among these field cores at other core layers are also observed. For each pavement core, the number of air voids varying with depths while the air void size distribution remains almost the same.

Calculation of P_{av} and Asphalt Binder Oxidation Rates

For each air void radius (r_i) and shell distance ($r_{NFB,i}$) pair at a given air void size range, the vertical transport model is used to calculate oxygen pressure profiles (P_{av}), both upper and lower limits, as a function of depths; and P_{av} values at corresponding depths is then read from the plot. The assumption of convection dominated transport process established the upper limit, a constant oxygen pressure at 0.2 atm throughout the air void channel. The assumption of oxygen transport by diffusion only provided the lower limit, a profile of decreasing of oxygen pressure away from surface of the pavement. P_{av} values at corresponding depths for each pavement core layer is summarized and reported in Appendix C2.

With known temperature profiles, the upper and lower P_{av} values for each air void radius (r_i) and shell distance ($r_{NFB,i}$) pair, the air void radius (r_i) and the shell distance ($r_{NFB,i}$), and asphalt binder oxidation and hardening kinetics parameters at constant reaction period; the horizontal diffusion and reaction model was used to calculate a highest oxidation rate and a lowest oxidation rate for air voids in each given size range at different core layers. The bulk oxidation rate for each core layer was

estimated from Equation IV-8 with known oxidation rates for each air void size range and number of air voids in each size range. Oxidation rates calculated for each air void size range as well as bulk oxidation rates at each core layer for these validation cores is reported in the Appendix C3.

Table V-4 summarizes yearly maximum and minimum oxidation rates for different layers of the selected pavement cores. Detailed data of modeled oxidation rates for each pavement cores are reported in Appendix C3. As reported in Table V-4, the yearly oxidation rates could reach as high as 0.1198 CA/year (Pavement US54 at the top layer), and go as low as 0.0182 CA/year (Minnesota Cell 1 at Layer 6). The ranking of pavements in order of calculated oxidation rates are US54, US290, US277, IH35-LRD, US69, IH35-Waco, and Minnesota Cell 1 from high to low. This ranking is, in fact, quite consistent from the perspective of the key elements that affect asphalt binder oxidation in pavements including pavement temperature, pavement air voids properties, and asphalt binder oxidation kinetics.

Table V-4 Summary of Maximum and Minimum Oxidation Rates Calculated for Each Pavement Core Layers

Oxidation rate (CA/year)		US277	US69	US54	US290	IH35 (Waco)	IH35 (LRD)	MN (Cell 1)
Layer 1	Highest	0.0526	0.0296	0.1198	0.0771	0.0268	0.0384	0.0239
	Lowest	0.0524	0.0294	0.1174	0.0761	0.0253	0.0281	0.0238
Layer 2	Highest	0.0489	0.0267	0.1151	0.0697	0.0266	0.0382	0.0226
	Lowest	0.0480	0.0264	0.1061	0.0674	0.0243	0.0257	0.0224
Layer 3	Highest	0.0460	0.0243	0.1119	0.0639	0.0264	0.0384	0.0215
	Lowest	0.0447	0.0239	0.0976	0.0610	0.0240	0.0221	0.0212
Layer 4	Highest	0.0437	0.0227	0.1075	0.0593	0.0263	0.0384	0.0206
	Lowest	0.0420	0.0223	0.0918	0.0550	0.0240	0.0221	0.0202
Layer 5	Highest	0.0411	--	0.1040	0.0557	0.0262	--	0.0192
	Lowest	0.0382	--	0.0839	0.0506	0.0240	--	0.0188
Layer 6	Highest	--	--	--	--	0.0263	--	0.0187
	Lowest	--	--	--	--	0.0242	--	0.0182

Minnesota Cell 1 has the lowest oxidation rate calculated among these seven pavement sites, primarily caused by the cold climate in Minnesota. As shown in Figure V-1, the daily average temperature for Minnesota cell 1 is much lower than that for the other Texas pavements. Among the Texas pavements, the asphalt binder in US54 has an exceptionally low value of activation energy of 54.95 kJ/mol. As a result, the oxidation rate is much higher compared with other asphalt binders under the same oxygen pressure. For US290, the air voids content is extremely high (12.44%); and the majority of air voids has air void radius larger than 0.5 mm. Because of that, it is not surprising to see a higher oxidation rate for US290. Texas pavement US277 has intermediate air voids content and an intermediate values of activation energy compared to other Texas pavements, and a maximum oxidation rate of 0.0526 CA/year was calculated. Exceptions in Texas pavements are IH35-LRD, IH35-Waco and US69 that have oxidation rates comparable to Minnesota Cell 1. IH35-LRD and IH35-Waco are rich bottom layers that are 12 to 16 inches below the pavement surface. The amplitude of daily temperature fluctuation attenuates to a great deal at these depths, as shown in Figure V-1, and causes oxidation rates to decrease drastically compared with these for surface layers. Although for US69, it seems the low oxidation rate is caused by the combination of high activation energy of asphalt binders, less favorable air voids distribution, and relatively low pavement temperature.

For each pavement core, oxidation rates decrease away from the surface. Taking US277 as an example, maximum oxidation decreases from 0.0526 CA/year at the top layer to 0.0411 CA/year in the layer 5. These differences in oxidation rate with pavement depth are mainly caused by temperature differences, because all model inputs are almost the same in the calculation of maximum oxidation rates at different core layers except pavement temperature. Similarly, a decrease of minimum oxidation rate away from the pavement surface is observed, but at a greater degree. In this case, the decrease of oxidation is not only influenced by pavement temperature, but also pressure in air voids (P_{av}), that also decreases away from the pavement surface.

Measured Oxidation Rates versus Modeled Oxidation Rates

Because of the limited number of cores that was obtained, the relatively short time between corings (due to the project length relative to the slow field oxidation rate), and the inherent variability that tends to exist between cores, the ability to make layer-by-layer comparisons of these field oxidation measurements, especially considering the fairly modest layer-by-layer differences indicated by the model calculations, is necessarily limited. Consequently, the overall binder oxidation rates for each pavement core (rather than slice by slice comparisons) were compared using the field measurements and model calculations.

Table V-5 2 summarizes yearly oxidation rates (in terms of carbonyl growth) measured for these six validation cores. Maximum and minimum oxidation rates calculated from the model are also reported. The visual comparison is shown in Figure V-4.

Table V-5 Comparison of Measured and Modeled Field Oxidation Rates

STATES	Site	Oxidation rate modeled (CA/year)		Bulk oxidation rate measured (CA/year)
		Maximum	Minimum	
MN	Cell 1	0.0200	0.0195	0.0256
TX	US277-LRD	0.0465	0.0451	0.0705
	US69-LFK	0.0258	0.0255	0.0370
	IH35-LRD #4	0.0384	0.0245	---
	US290-BRY	0.0651	0.0620	0.0671
	IH35-WAC #4	0.0264	0.0243	0.0340
	US54-AMR	0.1117	0.0994	0.0935

The ranking of predicted oxidation rates from high to low is the same as the ranking established by field measurement except for US277 and the oxidation rates measured in the field can be quite close to the range of predicted oxidation rates that

were established by the maximum and minimum oxidation rates. For example, the measured oxidation rate is only 3% higher than the maximum oxidation rate calculated for US290, and for US54 the measured oxidation rate is 6 percent lower than the minimum oxidation rate predicted.

There are also exceptions. For example, for pavements from US277, US69, IH35-Waco, and Minnesota Cell 1; the respective measured oxidation rates are 34, 30, 22, and 21% higher than the maximum oxidation rates predicted.

A possible explanation of these higher rates is that these pavements were all newly constructed pavements, at least relative to their oxidation rates; at the time of their first core, the Texas pavement's respective service lives were 0, 1.5, and 2 years. For Minnesota Cell 1, the first core was taken after 11 years in the road. Oxidation of a neat asphalt binder is characterized by an initial rapid rate period that declines over time until a constant-rate period is reached. It has been estimated that the fast oxidation rate period can last as long as 2~3 years for Texas pavements, and 12 years or longer for Minnesota pavements. Thus, the asphalt binder oxidation for these pavement cores was most likely dominated by the initial rapid oxidation period, rather than the slower constant-rate reaction regime. However, in the model calculations, only the slower constant-rate reaction kinetics parameters were used to calculate the field oxidation rates, thereby likely providing a significant underestimation of the oxidation rates. The reaction rate for the constant rate period can generally be described using an Arrhenius expression for temperature variation and pressure dependence, while the reaction mechanisms are still not fully understood for the initial rapid rate period. An extensive understanding of oxidation mechanisms and oxidation kinetics in this rapid oxidation period is essential to incorporating the fast reaction period into this model and to providing a more accurate prediction of oxidation rates during the first several years of service for newly constructed pavements.

In spite of this disagreement of model predictions for pavements that are largely in the fast rate oxidation period, in general this fundamentals-based model provides a

good match with field measurements, suggesting that it captures the critical elements that affect asphalt binder oxidation in pavements.

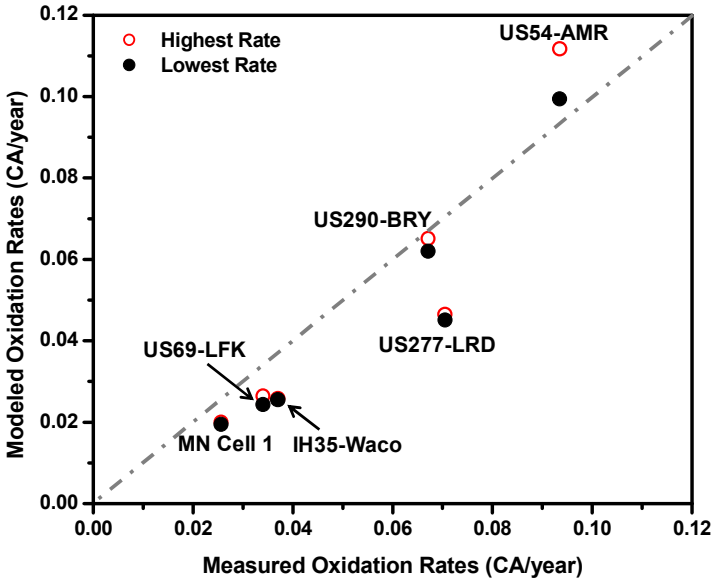

Figure V-4. Comparison of Measured and Modeled Field Oxidation Rates

Conclusions

Asphalt oxidation rates for six pavements with distinct temperature profiles, air voids properties, asphalt binder oxidation kinetics, and years in service were measured and compared with model calculations. Measured bulk oxidation rates of pavement cores vary from 0.0935 CA/year for US54 in Amarillo, Texas, to 0.0256 CA/year for Minnesota Cell 1.

Measured oxidation rates among these pavements are largely consistent with key elements that affect asphalt binder oxidation in pavements including pavement temperature, pavement air voids properties, and asphalt binder oxidation kinetics. In general, asphalt binders with high activation energy results in a low oxidation rate in the field; high pavement temperatures lead to an increased oxidation rate (Texas pavements

versus Minnesota pavement; surface cores versus rich bottom cores); and large air void pore radius and small shell distance produce a higher oxidation rate.

Pavement temperature and air voids parameters for these pavement cores were also collected as model inputs to predict field oxidation rates for these validation pavement cores. The ranking of predicted oxidation rates was exactly the same as the ranking established by field measurement except for US277; and oxidation rates measured in the field, in general, fell in between or close to the range of predicted oxidation rates established by the maximum and minimum oxidation rates with a few exceptions. The exceptions were newly constructed pavements where asphalt binder oxidation rates most likely are still governed by the initial rapid oxidation period, rather than the slower constant reaction rate regime used in the model calculations, thus significantly underestimating the oxidation rates for these new pavements.

An extensive understanding of oxidation mechanisms and oxidation kinetics in this rapid oxidation period is essential to incorporating the fast reaction period into this model to provide more accurate prediction of oxidation of newly constructed pavements.

CHAPTER VI
SUMMARY, CONCLUSIONS, AND RECOMMENDATIONS

Summary and Conclusions

To pavement engineers, the ability to predict chemical and physical changes of asphalt binder over time with oxidation in pavements is critical to design a new pavement with better performance or to schedule an appropriate maintenance treatment for existing pavements. In this dissertation, a fundamentals-based oxygen transport and reaction model was developed to quantitatively assess asphalt binder oxidation in pavements.

The success of such a model calculation relies heavily on accurate representation of pavement temperature, understanding of oxygen diffusivity in asphalt binders and mastics, and characterization of air voids in pavements. Therefore, these key model elements were studied accordingly. In the meanwhile, a fundamentals-based oxygen transport and reaction model was developed to incorporate these model elements to predict asphalt binder oxidation for a number of Texas and Minnesota pavements. These model calculations of field oxidation rates were further validated with field measurement. Research findings and a summary for each individual task follows.

Pavement Temperature Modeling

To obtain accurate prediction of pavement temperature nationwides as a function of depth and time, an improved one-dimensional model was developed based on heat transfer fundamentals. The model employs commonly recorded hourly solar radiation, daily average wind speed in hourly format, and interpolated hourly air temperature as climate input data. Three key site-specific model parameters were identified including albedo, difference between emissivity and absorption coefficient, and absorption coefficient. National distribution of their values correlates with climatic patterns,

enabling interpolation of these model parameters based on climate. The temperature model, proposed data sources, and interpolated model parameters provided model calculation that agreed well with experimental measurements.

Oxygen Diffusivity in Asphalt Binders and Mastics

Estimates of oxygen diffusivity in asphalt binders were made based on laboratory oxidation experiments in asphalt binder films of known reaction kinetics. Comparing the oxidation rates at the binder surface and at a solid-binder interface at the film depth was used to estimate oxygen diffusivity based on a thin film oxygen diffusion and reaction model.

For asphalt binders, oxygen diffusivities ($\mathcal{D}_{O_2}$) ranged from10^{-10} to 10^{-11} m^2/s, varying with temperature (T) and asphalt binder low shear rate limiting viscosity (η_o*); $\log(\mathcal{D}_{O_2}/T)$ varied linearly with $\log(\eta_o^*)$ for both base asphalt binders and polymer modified asphalt binders according to:

$$\frac{\mathcal{D}_{O_2}}{T} = 2.51\times10^{-11}\left(\eta_0^*\right)^{-0.55} \qquad \text{(VI-1)}$$

For asphalt mastics, oxygen diffusivity was observed to decrease as filler volume fraction increased. Quantitatively, this effect follows a theoretical estimate of the effect of a dilute suspension of spherical inclusions on diffusivity.

Characterization of Air Void in Pavements

Air void structure in pavements was studied with X-ray CT and image analysis techniques to examine the internal microstructure including air void distribution and interconnectivity. The final images after imaging process are black and white images of total air voids and interconnected air voids of each slice of the pavement core specimen.

A macro in image-J to analyze particle size and to count particle number is then used to quantify air void distribution from these final black and white images from X-ray CT. Information obtained from this analysis included total air voids, size of each air void, and average shell distance. These air voids parameters were used as inputs for model calculations.

One critical issue encountered when using X-ray CT for pavement air void characterization is undetected air voids smaller than 0.2 mm in size due to the equipment resolution limit. To obtain a complete profile of air void distribution that cannot be fully measured by X-ray CT, log-normal distribution functions were used to predict the complete air void size distribution with the available size distribution measured with X-ray CT as an input.

Development of an Oxygen Transport and Reaction Model

Oxygen transport and reaction in pavements is described as two interlinked steps: 1) diffusion and/or flow of oxygen from the atmosphere above the pavement into the interconnected air voids in the pavement; and 2) diffusion of oxygen from those air voids into the adjoining asphalt-aggregate matrix where it reacts with the asphalt binder. Based on this model concept, vertical transport through an air void channel and horizontal transport and reaction within the asphalt-aggregate matrix layer associated with an air void channel were modeled mathematically to calculate oxidation rate for this finite asphalt-aggregate matrix layer for each air void with known air voids parameters including air void radius (r_i) and shell distance ($r_{NFB,i}$), pavement temperature, oxygen diffusivity, and asphalt binder oxidation kinetics. The bulk oxidation rate for a pavement layer was calculated as the average of oxidation rates calculated for each air void.

Model Validation with Field Measurement

Asphalt binder oxidation rates of six pavements with distinct temperature profiles, air voids properties, asphalt binder oxidation kinetics, and years in service were measured and compared with model calculations. Measured bulk oxidation rates of pavement cores vary from 0.0935 CA/year for US54 in Amarillo, Texas, to 0.0256 CA/year for Minnesota Cell 1. This ranking of measured oxidation rates among these pavements is consistent from the perspective of the key elements that affect asphalt binder oxidation in pavements including pavement temperature, pavement air voids properties, and asphalt binder oxidation kinetics.

Pavement temperature and air voids parameters for these pavement cores were collected as model inputs to predict field oxidation rates for these validation pavement cores. The ranking of predicted oxidation rates from high to low is the same as the ranking established by field measurement except for US277, and the oxidation rates measured in the field can be quite close to the range of predicted oxidation rates that were established by the maximum and minimum oxidation rates. The exceptions are newly constructed pavements where asphalt binder oxidation rate most likely are still governed by the initial rapid oxidation period, rather than the slower constant reaction rate regime used in the model calculations, which will significantly underestimate the oxidation rates for these new pavements.

An extensive understanding of oxidation mechanisms and oxidation kinetics in this rapid oxidation period is essential to incorporate the fast reaction period into this model to provide more accurate prediction of oxidation of newly constructed pavements.

Recommendations

Determination of Asphalt Binder Oxidation Kinetics

Asphalt binder oxidation kinetics is an important element in the oxygen transport and reaction model. The determination of oxidation kinetics for a given asphalt binder

requires extensive measurements of oxidation rates of thin asphalt binder film, at controlled temperatures (at least three different temperatures) and pressure (1 atm air pressure). From these data, activation energy and pre-exponential factor is estimated based on the Arrhenius equation of asphalt binder oxidation rate. The entire testing time could be rather time-consuming, from 1 to 3 months depending on oxidation temperatures, which inhibits the application of this oxidation model. Therefore, there is a great need for a fast aging test that is capable of predicting asphalt binder oxidation kinetic parameters based upon relatively rapid laboratory experiments.

Accelerated oxidation conditions at higher oxidation pressure (20 atm air pressure in the PAV, for example) could be used to greatly reduce the required oxidation time at 1 atm air pressure, from several months to several days. However, oxidation kinetic parameters measured at this accelerated condition are totally different than the values obtained at 1 atmosphere air pressure. There might exist a possible correlation that links the oxidation kinetic parameters obtained at these two conditions within a reasonable accuracy.

High Resolution X-ray CT Scanning

Pavement air voids are characterized with X-ray CT techniques in this dissertation to obtain model required air void parameters including air void radius, shell distance, and number of air voids for each pavement layer. One critical issue encountered when using X-ray CT is the resolution limit that fails to detect air voids smaller than 0.2 mm in size. A log-normal distribution function of air voids in pavements is assumed to predict these undetected air voids with measured air voids using X-ray CT as an input. However, there is no direct support for this assumption. High resolution X-ray CT scanning of pavement cores should be evaluated to provide more conclusive information.

Oxidation Kinetics at Fast Reaction Period

Although the reaction kinetics of asphalt binder oxidation during the constant-rate period has been studied extensively, the early-time, fast-rate period reaction kinetics are not fully understood, providing a source of error when comparing model predictions with field measurements of asphalt binder oxidation in Chapter V. It has been estimated that it takes two to three years for Texas pavements to past the fast-rate period in the field. An extensive understanding of oxidation mechanisms and oxidation kinetics in this rapid oxidation period is essential to provide more accurate prediction of oxidation of newly constructed pavements.

A two parallel reactions scheme has been suggested for asphalt binder oxidation in the literature, one a first-order reaction with respect to phenol and the other a zero-order reaction with respect to aromatics. The combined effect of these two reactions was an early time fast (but declining) rate period of oxygen absorption, followed by a later-time constant-rate period after the first reaction terminated due to depletion of phenol, the limiting reactant. From this perspective, asphalt binder oxidation kinetics in this fast reaction period could also be determined by oxidizing asphalt binder thin films at different temperatures.

Further Model Calibration and Validation

The calibration and validation of the asphalt binder oxidation model in pavements is still an ongoing process. In this dissertation, a very limited number of pavement cores and coring times for each validation site were used to estimate asphalt binder oxidation rates. These field measurements might not provide a very accurate measure of field oxidation rates, and more sophisticated comparison of asphalt binder oxidation rates as a function of pavement depth is not included in this study because of that. Therefore, field oxidation rates in these pavements need to be monitored and

reported continuously to further validate the model with additional data of asphalt binder oxidation in pavements.

LITERATURE CITED

1 Liu M, Lunsford KM, Davison RR, Glover CJ, Bullin JA. The kinetics of carbonyl formation in asphalt. *AIChE Journal*. 1996. 42(4):1069-1076.

2 Domke CH, Davison RR, Glover CJ. Effect of oxygen pressure on asphalt oxidation kinetics. *Ind. Eng. Chem. Res.* 2000. 39(3):592-598.

3 Lin MS, Lunsford KM, Glover CJ, Davison RR, Bullin JA. The effects of asphaltenes on the chemical and physical characteristics of asphalts. *Asphaltenes: Fundamentals and Applications*. New York: Plenum Press, 1995. 155-176.

4 Lau CK, Lunsford KM, Glover CJ, Davison RR, Bullin JA. Reaction rates and hardening susceptibilities as determined from POV aging of asphalts. *Transportation Research Record*: *Journal of the Transportation Research Board*. 1992. 1342(50):50-57.

5 Al-Azri NA, Jung SH, Lunsford KM, Ferry A, Bullin JA, Davison RR, Glover CJ. Binder oxidative aging in Texas pavements: hardening rates, hardening susceptibilities, and the impact of pavement depth. *Transportation Research Record*: *Journal of the Transportation Research Board*. 2006. 1962:12-20.

6 Woo WJ, Ofori-Abebresse E, Chowdhury A, Hilbrich J, Kraus Z, Martin AE, Glover CJ. Polymer modified asphalt durability in pavements. *Report FHWA/TX-07/0-4688-1*. College Station, TX, Texas Transportation Institute, 2007.

7 Al-Omari A, Tashman L, Masad E, Cooley Jr. LA, Harman T. Proposed methodology for predicting HMA permeability. *Journal of the Association of Asphalt Paving Technologist.,* 2002. 71:30-58.

8 Masad E, Arambula E, Ketcham R, Abbas A, Martin AE. Nondestructive measurements of moisture transport in asphalt mixtures. *Asphalt Paving Technology.* 2007. 76:919-952.

9 Dempsey, BJ. "A heat transfer model for evaluating frost action and temperature related effects in multilayered pavement systems". *Highway Research Record*, 1970. 342: 39–56.

10 Rumney, TN, and Jimenez, RA. Pavement temperatures in the southwest. *Highway Research Record*, 1969. 361: 1–13.

11 Solaimanian, M, and Kennedy TW. Predicting maximum pavement surface Temperature using maximum air temperature and hourly solar radiation. In *Transportation Research Record*: *Journal of the Transportation Research Board,*

Washington, DC, Transportation Research Board of the National Academies, 1993. 1417: 1–11.

12 Lytton, RL, Pugahl, DE, Michalak, CH, Liang, HS, and Dempsey, BJ. An integrated model of the climatic effects on pavements. *Report FHWA-RD-90-033*, College Station, TX, Texas Transportation Institute, 1989.

13 Liang, RY, S. Rabab'ah, and Al-Akhras, K. Validation of enhanced integrated climatic model prediction over different drainable base materials. *Transportation Research Board Annual Meeting*. 2006 CD-ROM.

14 Ahmed, Z, Marukic, I, Zaghloul, S, Vitillo, N. Validation of enhanced intergrated climatic model predictions with New Jersey Seasonal Monitoring Data. In *Transportation Research Record*: *Journal of the Transportation Research Board,* Washington, DC, Transportation Research Board of the National Academies, 2005. 1913: 148–161.

15 Hermansson, A. Simulation model for calculating pavement temperatures, including maximum temperature. In *Transportation Research Record*: *Journal of the Transportation Research Board.* Washington, DC, Transportation Research Board of the National Academies, 2000. 1699: 134–141.

16 Hermansson, A. Mathematical model for paved surface summer and winter temperature: comparison of calculated and measured temperatures. *Cold Regions Science and Technology*, 2004. 40: 1-17.

17 Gui, J, Phelan, PE, Kaloush, KE, Golden, JS. Impact of pavement thermophysical properties on surface temperature. *Journal of Materials in Civil Engineering*, 2007. 19: 683-690.

18 Petersen, JC, Branthaver, JF, Robertson, RE, Harnsberger, PM, Duvall, JJ, Ensley, EK. Effects of physicochemical factors on asphalt oxidation kinetics. *Transp. Res. Rec*., 1993. 1391: 1-9.

19 Lee, DY, and Huang, RJ. Weathering of asphalts as characterized by infrared multiple internal reflection spectra. *Anal. Chem*., 1973. 46: 2242-2248.

20 Lin, MS, Chaffin, JM, Liu, M, Glover, CJ, Davison, RR, Bullin, JA. The effect of asphalt composition on the formation of asphaltenes and their contribution to asphalt viscosity. *Fuel Sci. and Technol. Intl.*, 1996. 14 (1&2):139-162.

21 Lin, MS, Chaffin, JM, Davison, RR, Glover, CJ, Bullin, JA. A new suspension viscosity model and its application to asphaltene association. *Structures and Dynamics of Asphaltene*, New York: Plenum Press, 1998. 267-302.

22 Martin, KL, Davison, RR, Glover, CJ, Bullin, JA. Asphalt aging in Texas roads and test sections. *Transp. Res. Rec*., 1990. 1269: 9-19.

23 Domke, C.H., Davison, RR, Glover, CJ. Effect of oxidation pressure on asphalt hardening susceptibility. *Transp. Res. Rec*., 1999. 1661: 114-121.

24 Lunsford, KM. The effect of temperature and pressure on laboratory oxidized asphalt flms with comparision to field aging. Ph.D. Dissertation, 1994. Texas A&M University, College Station, TX.

25 Glover, CJ., Davison, RR, Domke, CH, Ruan, Y, Juristyarini, P, Knorr, DB, Jung, SH. Development of a New Method for Assessing Asphalt Binder Durability with Field Validation. Report FHWA/TX-03/1872-2, 2005. Texas Transportation Institute, College Station, TX.

26 Ruan Y, Davison RR, Glover CJ. An investigation of asphalt durability: relationships between ductility and rheological properties for unmodified asphalts. *Pet. Sci. & Tech.*, 2003;21(1-2):231-254.

27 Vallerga BA, Halstead WJ. Effects of field aging on fundamental properties of paving asphalts. *Highway Research Record*. 1971;361:71-92.

28 Clark, RC. Practical results of asphalt hardening on pavement life. *Proc. Assoc. Asphalt Paving Technol*. 1958. 27: 196-208.

29 Doyle, PC. Cracking characteristic of asphalt cement. *Proc. Assoc. Asphalt Paving Technol*. 1958. 27: 581-597.

30 Halstead, W.J. The relation of asphalt ductility to pavement performance. *Proc. Assoc. Asphalt Paving Technol*. 1963. 32: 247-270.

31 Kanhal, PS, and Wenger, ME. Asphalt properties in relation to pavement performance. *Transp. Res. Rec*. 1975. 544: 1-13.

32 Kandhal, PS. Low-temperature ductility in relation to pavement performance. In C.R. Marek (Ed.) *ASTM STP 628: Low-Temperature Properties of Bituminous Materials and Compacted Bituminous Paving Mixtures*, Philadelphia, PA, American Society for Testing and Materials, 1977. pp. 95-106.

33 Kandhal, PS, and Koehler, WC. Significant studies on asphalt durability: Pennsylvania experience. *Transp. Res. Rec*. 1984. 999:41-50.

34 Coons RF, Wright PH. An investigation of the hardening of asphalt recovered from pavements of various ages. Journal of Association of Asphalt Paving Technologists. 1968;37:510-528.

35 ASTM D 2041, Standard test method for theoretical maximum specific gravity and density of bituminous paving mixtures. *2003 Annual Book of ASTM Standards, 04.03,* West Conshohocken, PA, ASTM, 2003.

36 ASTM D 6752, Standard test methods for bulk specific gravity and density of compacted bituminous mixtures using automatic vacuum sealing method. *2004 Annual Book of ASTM Standards, 04.03*, West Conshohocken, PA, ASTM, 2004.

37 ASTM D 6857, Standard test methods for maximum specific gravity and density of bituminous paving mixtures using automatic vacuum sealing method. *2003 Annual Book of ASTM Standards, 04.03*, West Conshohocken, PA, ASTM, 2003.

38 Woo WJ, Chowdhury A, Glover CJ. Field aging of unmodified asphalt binder in three Texas long-term performance pavements. *Transportation Research Record: Journal of the Transportation Research Board*. 2008. 2051: 11-22.

39 Masad E. X-Ray Computed tomography of aggregates and asphalt mixes. *Materials Evaluation*. 2004. 62:775-783.

40 Bird, RB, Stewart, WE, and Lightfoot, EN. *Transport phenomena*. 2nd ed. Hoboken, NJ. John Wiley & Sons. 2001.

41 NCHRP. Guide for mechanistic-empirical design of new and rehabilitated pavement structures. Final NCHRP Report 1-37A., Part 2. Design Inputs, Chapter 2. Material Characterization. www.trb.org/mepdg/Part2_Chapter2_Materials.pdf. Accessed July 05, 2007.

42 Prapaitrakul, N, Han, R, Jin, X, Glover, CJ. A transport model of asphalt binder oxidation in pavements. *Road Materials and Pavement Design.* 2009. 10/SI: 95-113.

43 Prapaitrakul, N. Towards an improved model of asphalt binder oxidation in pavements. Ph.D. Dissertation, 2009. Texas A&M University, College Station, TX.

44 Perez, R, Ineichen, P, Moore, K, Kmiecik, M, Chain, C, George, R, Vignola, F. A new operational model for satellite-derived irradiances: description and validation. *Solar Energy*, 2002. 73:307-317.

45 Maxwell, EL. METSTAT: The solar radiation model used in the production of the national solar radiation data base (NSRDB). *Solar Energy*, 1998. 62:263-279.

46 Brockwell, PJ, and Davis, RA. *Introduction to time series and forecasting*. 2nd ed. New York. Springer-Verlag, 2002.

47 Highter, WH, and Wall, DJ. "Thermal properties of some asphalt concrete mixes". *Transportation Research Record*. 1984. 968: 38-45.

48 Mrawire, DM, Luca, J. Effect of aggregate type, gradation, and compaction level on thermal properties of hot-mix asphalts. *Can. J. Civ. Eng*. 2006. 33: 1410-1417.

49 Luca, J, and Mrawira, DM. New measurement of thermal properties of superpave asphalt concrete. *Journal of Materials in Civil Engineering*. 2005. 17: 72-79.

50 Klein, AG, and Julienne, S. Development and validation of a snow albedo algorithm for the MODIS instrument. *Annals of Glaciology*, 2002. 34: 45-52.

51 National Climatic Data Center (NCDC). Climate Maps of United States-Mean Snow Depth. 2005. <http://cdo.ncdc.noaa.gov/cgi-bin/climaps/climaps.pl>. (Mar. 1, 2008).

52 Viswanadham, Y, and Ramanadham, R. Estimation of long wave radiation by an empirical method. *Pure and Applied Geophysics*, 1970. 81: 272-278.

53 National Climatic Data Center (NCDC). Climate Maps of United States-Mean Relative Humidity. 2005. <http://cdo.ncdc.noaa.gov/cgi-bin/climaps/climaps.pl>. (Mar. 1, 2008).

54 Petersen, JC. Quantitative function group analysis of asphalts using differential infrared spectrometry and selective chemical reaction-theory and applications. *Transportation Research Record*. 1986. 1096: 1-11.

55 Dickinson, EJ. The diffusion controlled reaction of oxygen with films of bituminous binders. *Australian Road Research*. 1984. 14: 121-132.

56 Liu, M, Ferry, MA, Davison, RR, Glover, CJ, Bullin, JA. Oxygen uptake as correlated to carbonyl growth in aged asphalts and asphalt Corbett fractions. *Ind. Eng. Chem. Res.* 1998. 37:4669-4674.

57 Han, R, Jin, X, Glover, CJ. Modeling of pavement temperature history for use in binder oxidation models and pavement performance prediction. *Journal of Materials in Civil Engineering*. In press.

58 Torres AC. Probabilistic analysis of air void structure and its relationship to permeability and moisture damage of hot mix asphalt. 2004. M.S. thesis. Texas A&M University, College Station, TX.

59 Burr BL, Glover CJ, Davison RR, Bullin JA. New apparatus and procedure for the extraction and recovery of asphalt binder from pavement mixtures. *Transportation Research Record: Journal of the Transportation Research Board*. 1993; 1391:20-29.

60 Burr BL, Davison RR, Jemison HB, Glover CJ, Bullin JA. Asphalt hardening in extraction solvents. *Transportation Research Record: Journal of the Transportation Research Board*. 1991; 1323:70-76.

61 Burr BL, Davison RR, Glover CJ, Bullin JA. Softening of asphalts in dilute solutions at primary distillation conditions. *Transportation Research Record: Journal of the Transportation Research Board*. 1994; 1436:47-53.

APPENDIX A

CARBONYL CONTENT AT ES AND SI: EXPERIMENTAL MEASUREMENT VERSUS MODEL CALCULATION

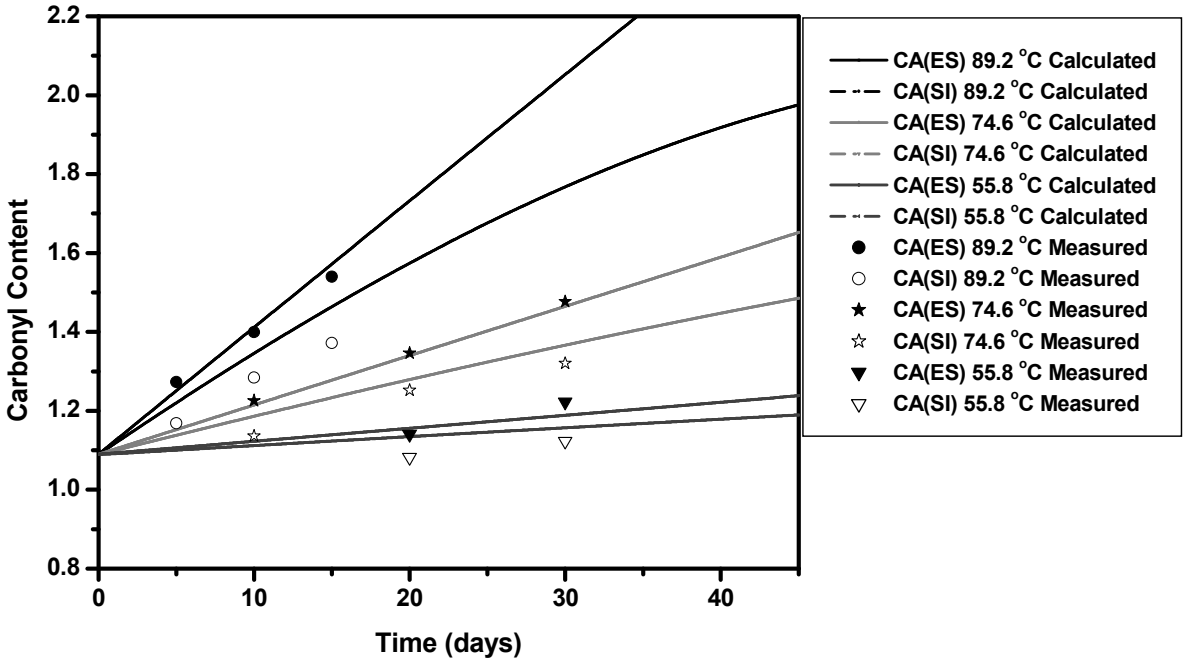

Figure A-1. Carbonyl Growth at ES and SI of Asphalt Film of Valero-Houston 64-22: Experimental Measurement versus Model Calculation

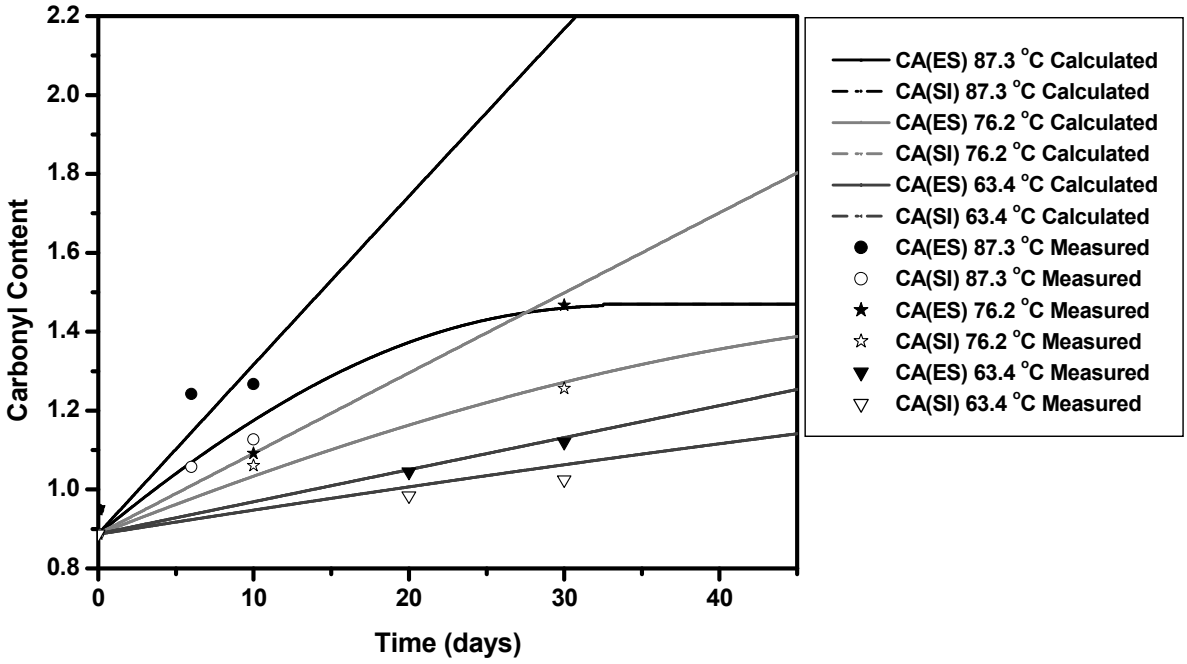

Figure A-2. Carbonyl Growth at ES and SI of Asphalt Film of Martin 64-22: Experimental Measurement versus Model Calculation

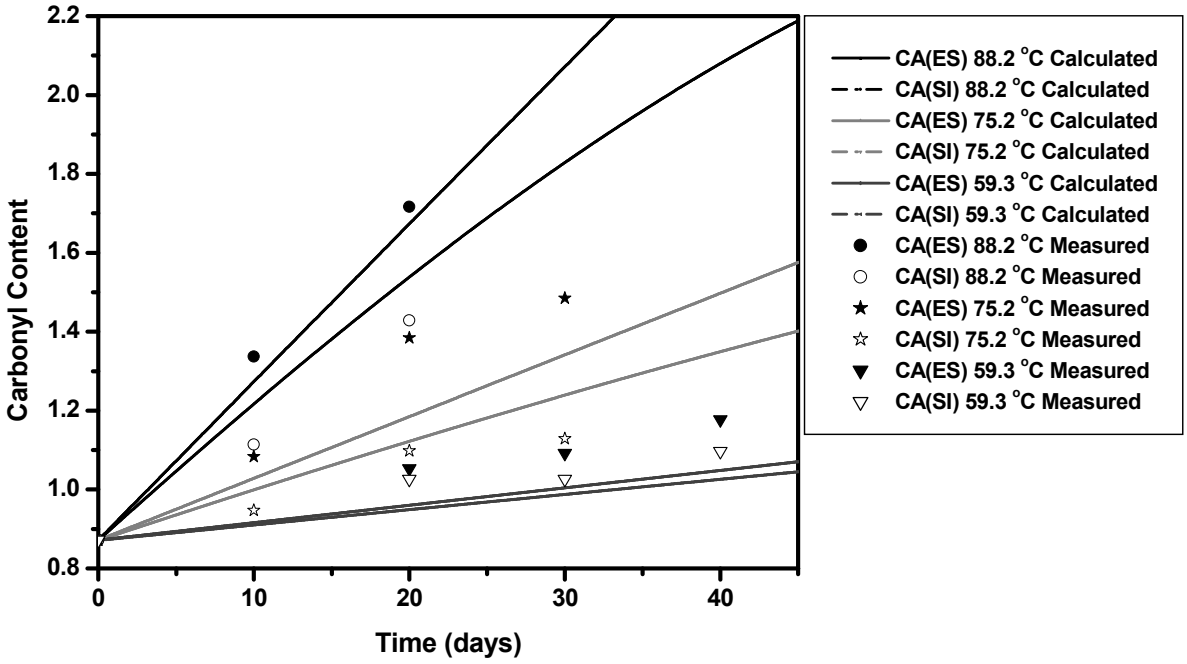

Figure A-3. Carbonyl Growth at ES and SI of Asphalt Film of Alon 64-22: Experimental Measurement versus Model Calculation

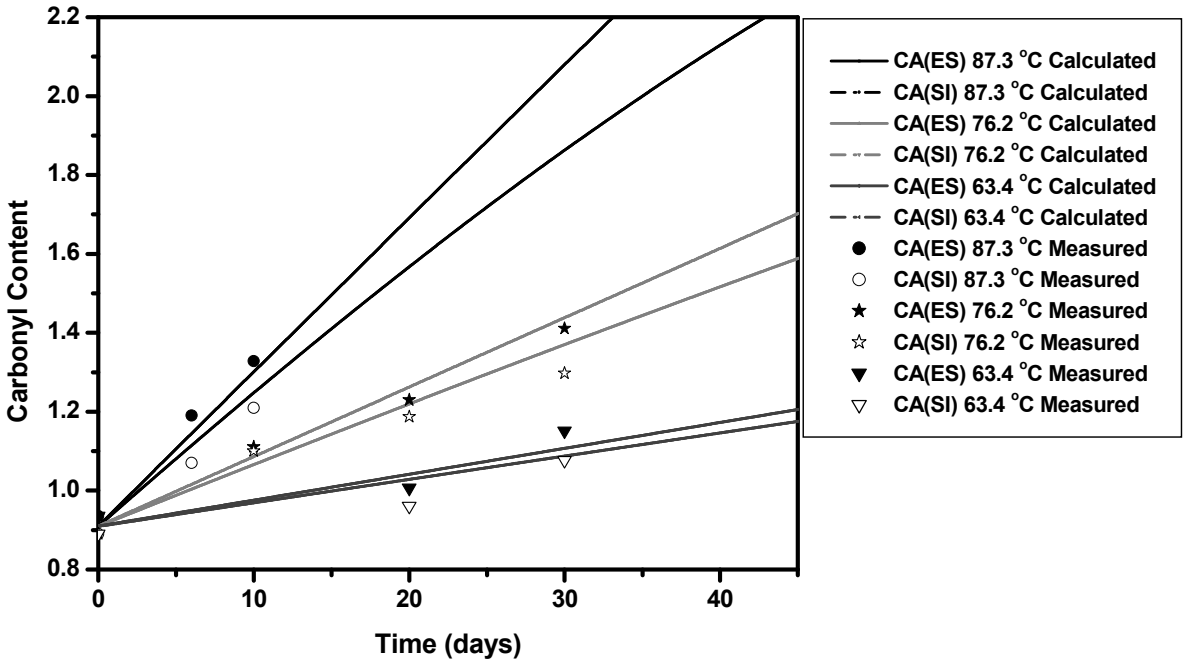

Figure A-4. Carbonyl Growth at ES and SI of Asphalt Film of Alon 76-22: Experimental Measurement versus Model Calculation

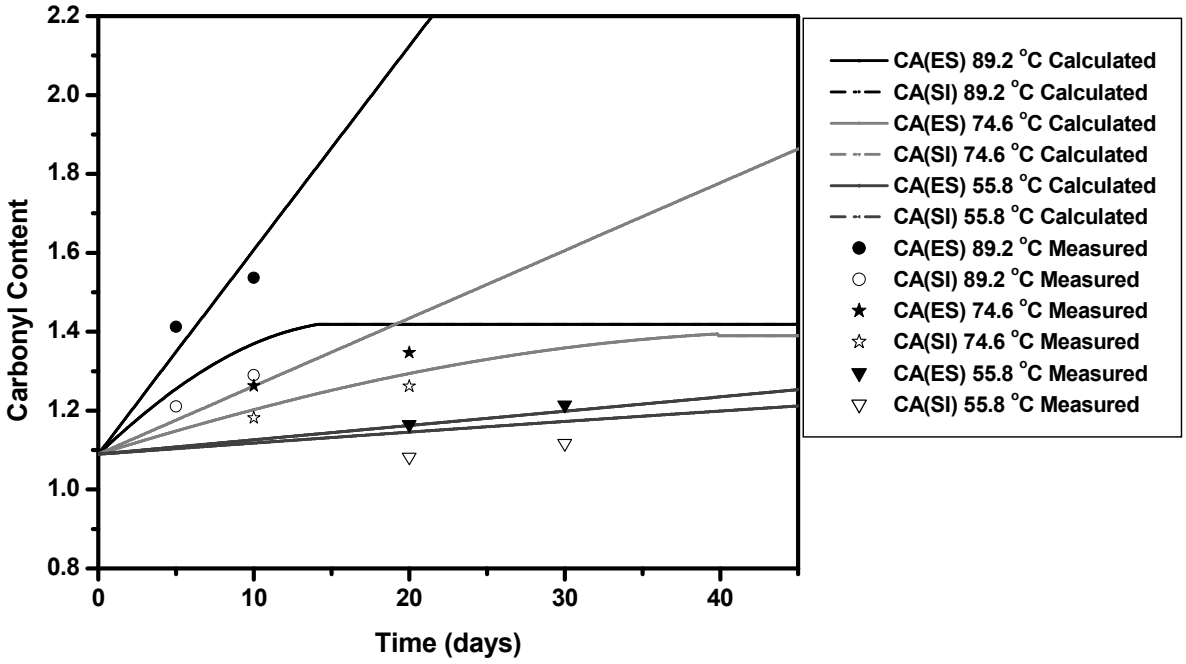

Figure A-5. Carbonyl Growth at ES and SI of Asphalt Film of Lion 64-22: Experimental Measurement versus Model Calculation

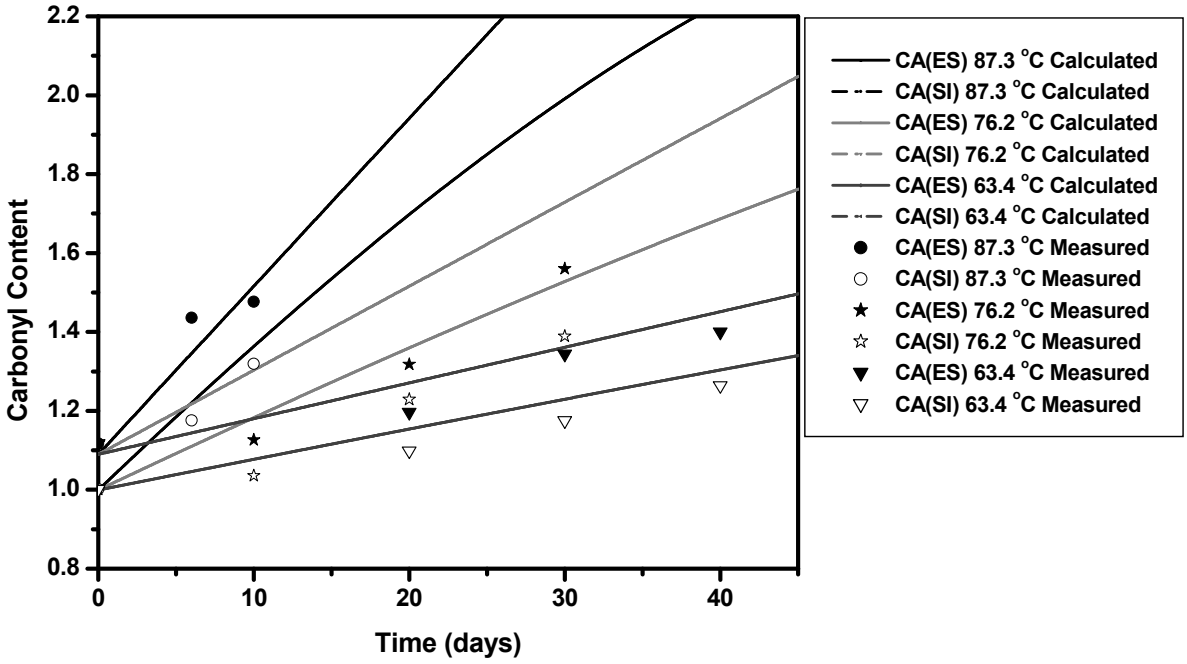

Figure A-6. Carbonyl Growth at ES and SI of Asphalt Film of Lion 70-22: Experimental Measurement versus Model Calculation

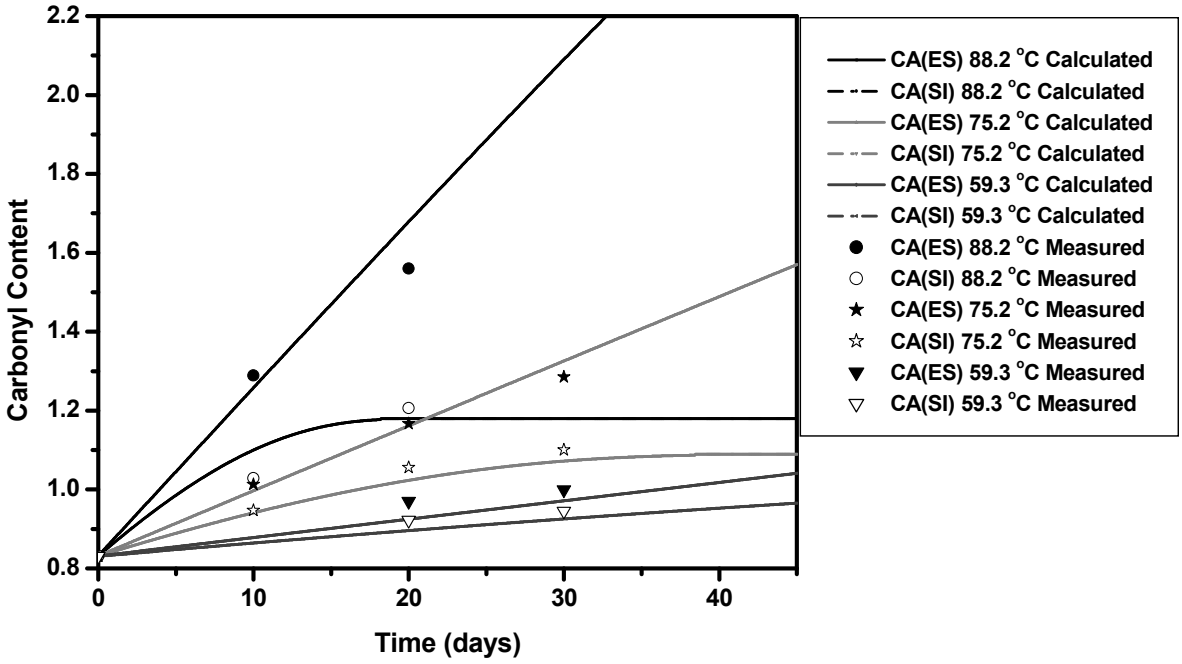

Figure A-7. Carbonyl Growth at ES and SI of Asphalt Film of SEM 70-22: Experimental Measurement versus Model Calculation

APPENDIX B

AIR VOID SIZE DISTRIBUTION IN PAVEMENTS (B1) AND CALCULATION OF AIR VOID DISTRIBUTION WITH LOG-NORMAL DISTRIBUTION (B2)

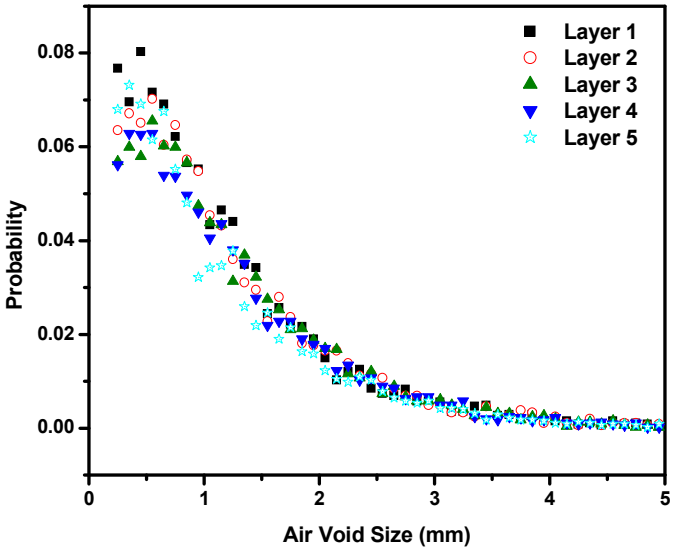

Figure B1-1. Air Void Distribution at Different Layers of Pavement US290

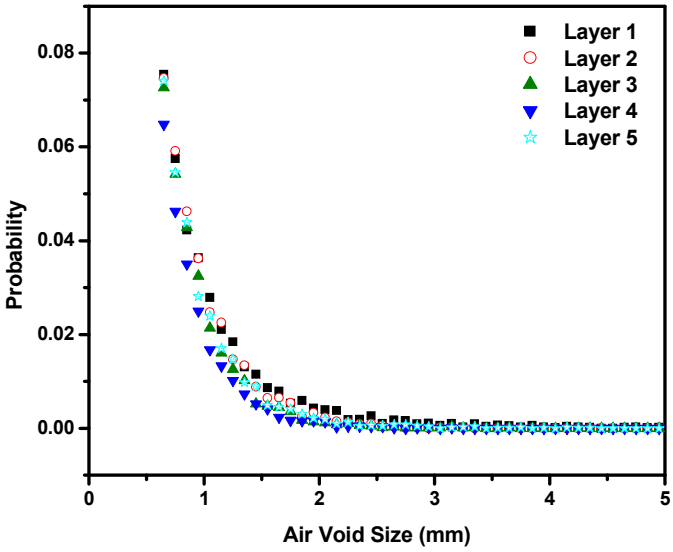

Figure B1-2. Air Void Distribution at Different Layers of Pavement US277

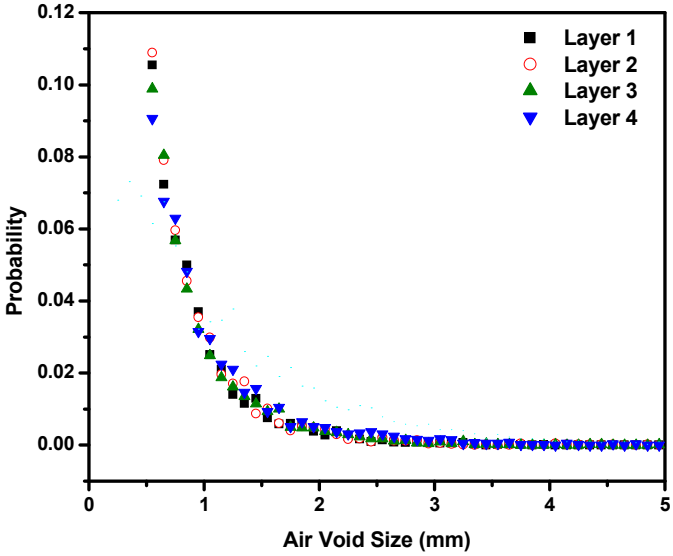

Figure B1-3. Air Void Distribution at Different Layers of Pavement US69

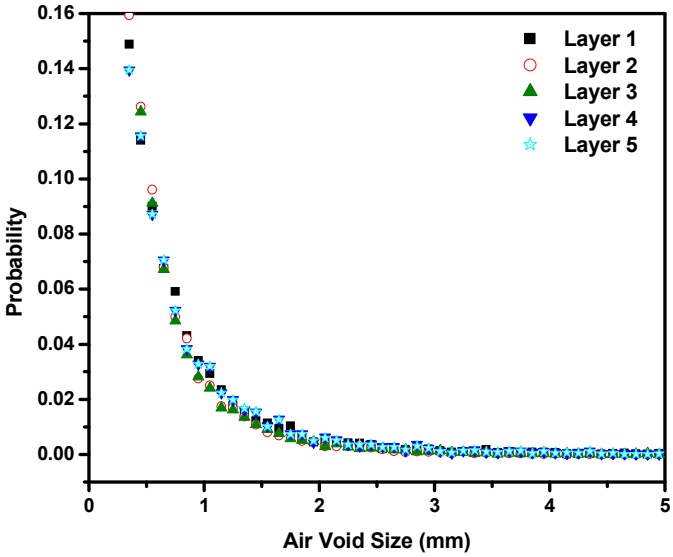

Figure B1-4. Air Void Distribution at Different Layers of Pavement US54

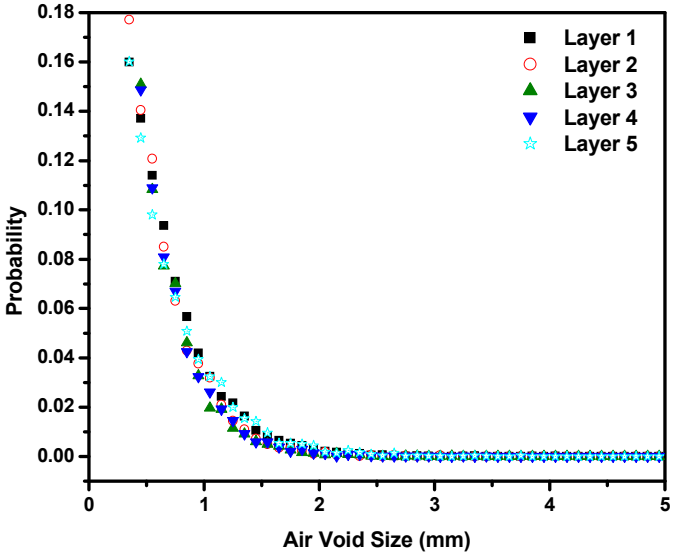

Figure B1-5. Air Void Distribution at Different Layers of Pavement IH35-Waco

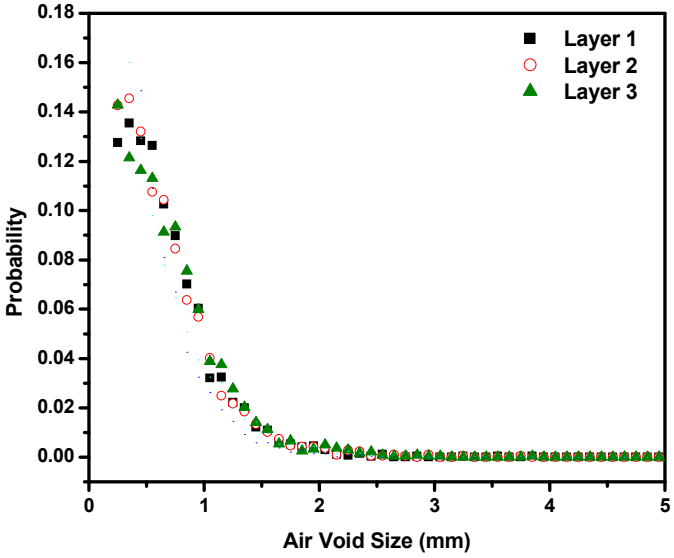

Figure B1-6. Air Void Distribution at Different Layers of Pavement IH35-LRD

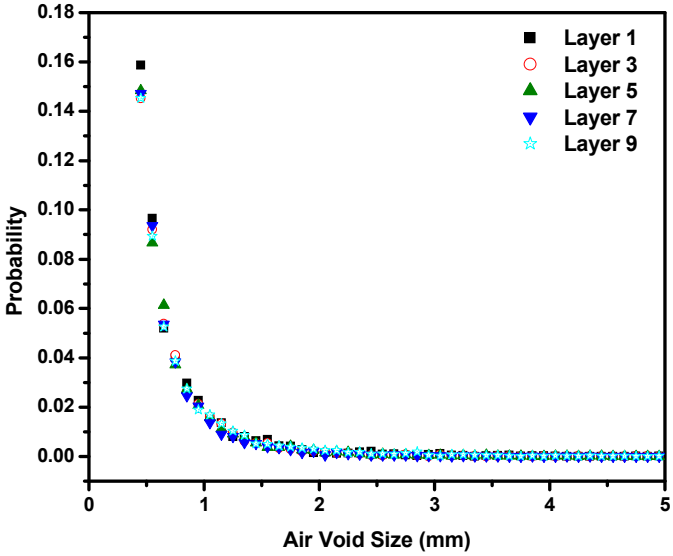

Figure B1-7. Air Void Distribution at Different Layers of Pavement Minnesota Cell1

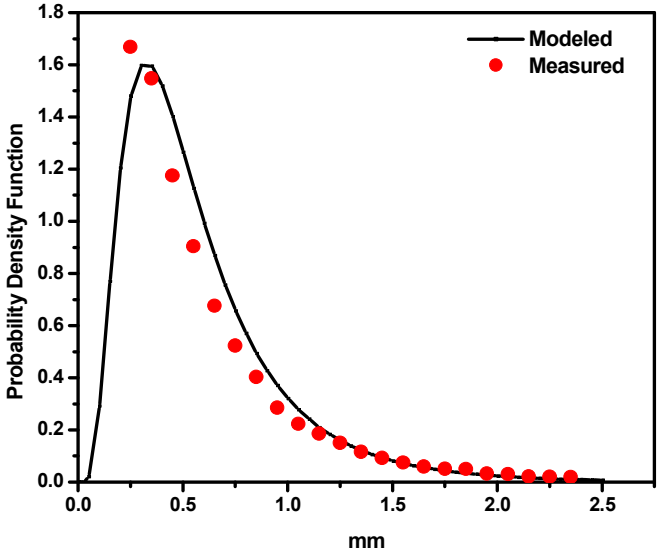

Figure B2-1. Calculation of Air Void Distribution with a Log-normal Distribution Function for Pavement SH59

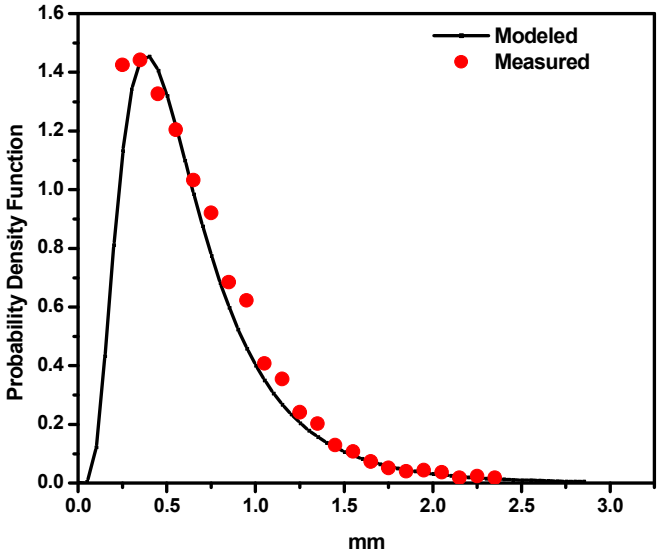

Figure B2-2. Calculation of Air Void Distribution with a Log-normal Distribution Function for Pavement IH35-LRD

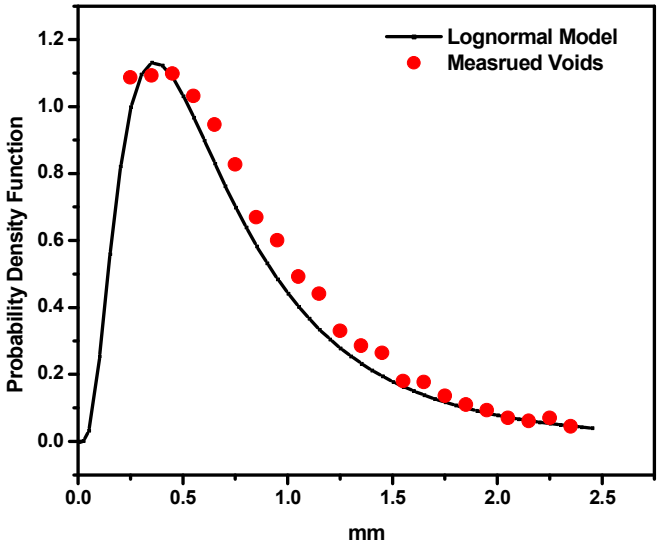

Figure B2-3. Calculation of Air Void Distribution with a Log-normal Distribution Function for Pavement US82

APPENDIX C

PAVEMENT TEMPERATURE (C1), AIR VOID CHARACTERIZATION (C2), AND CALCULATED FIELD OXIDATION RATES (C3) OF FIELD VALIDATION SITES

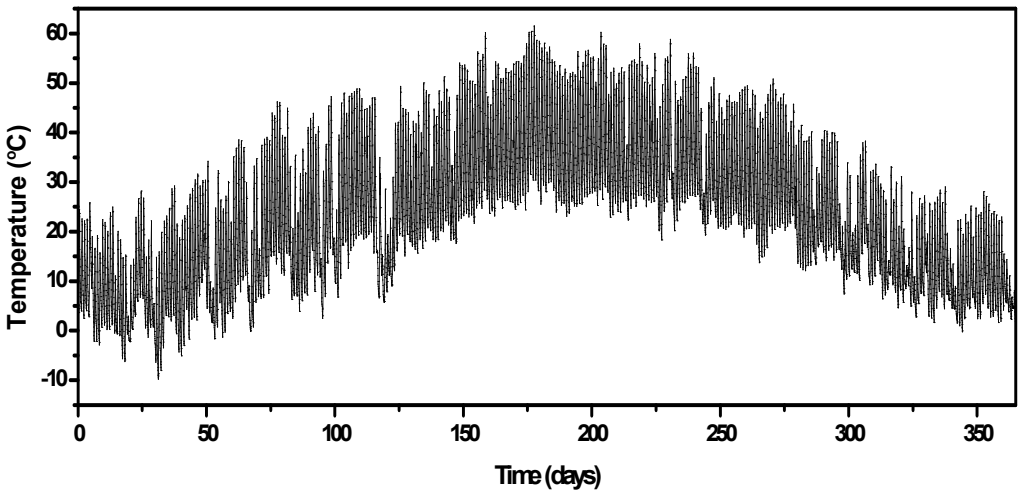

Figure C1-1 Pavement Temperature of US290 at Layer 1

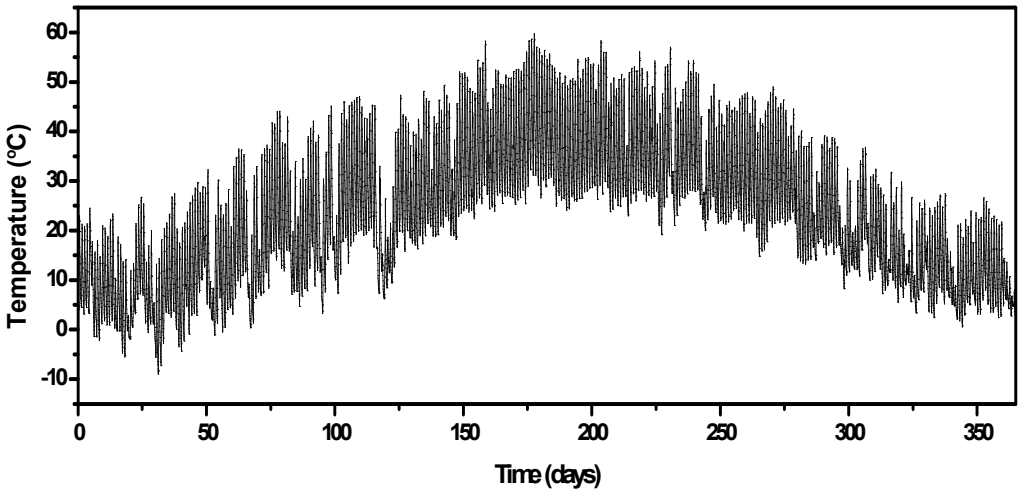

Figure C1-2 Pavement Temperature of US290 at Layer 2

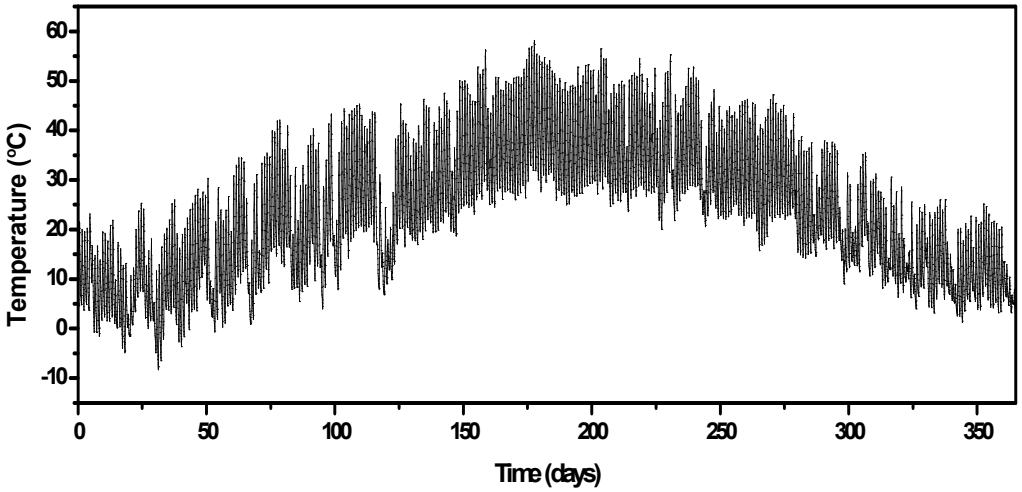

Figure C1-3 Pavement Temperature of US290 at Layer 3

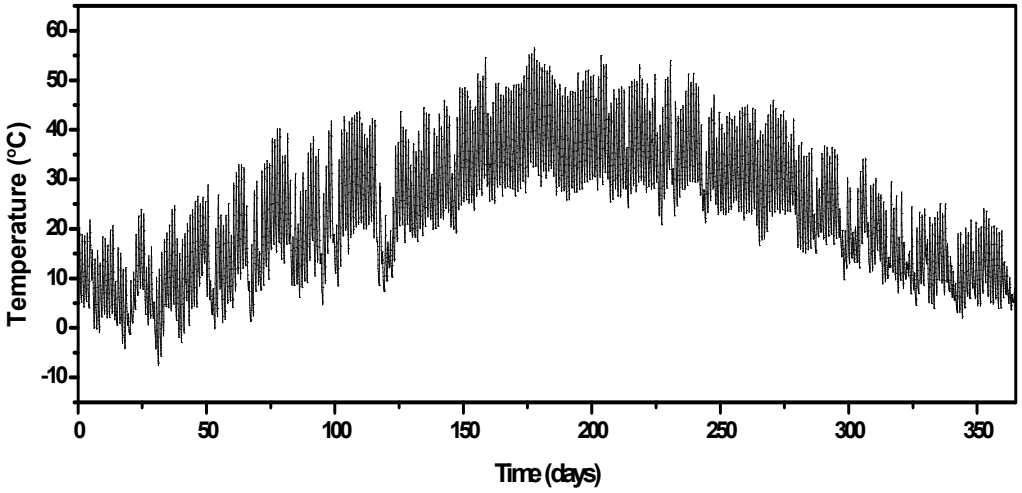

Figure C1-4 Pavement Temperature of US290 at Layer 4

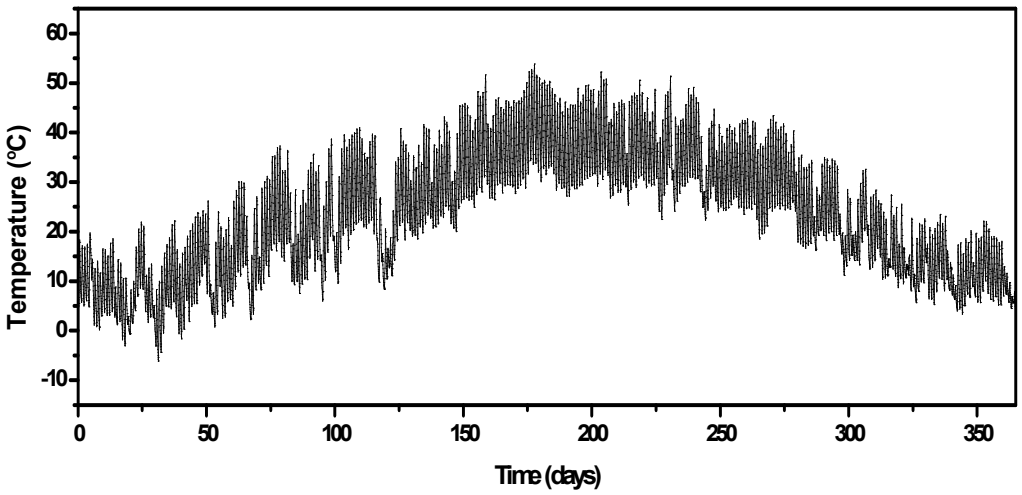

Figure C1-5 Pavement Temperature of US290 at Layer 5

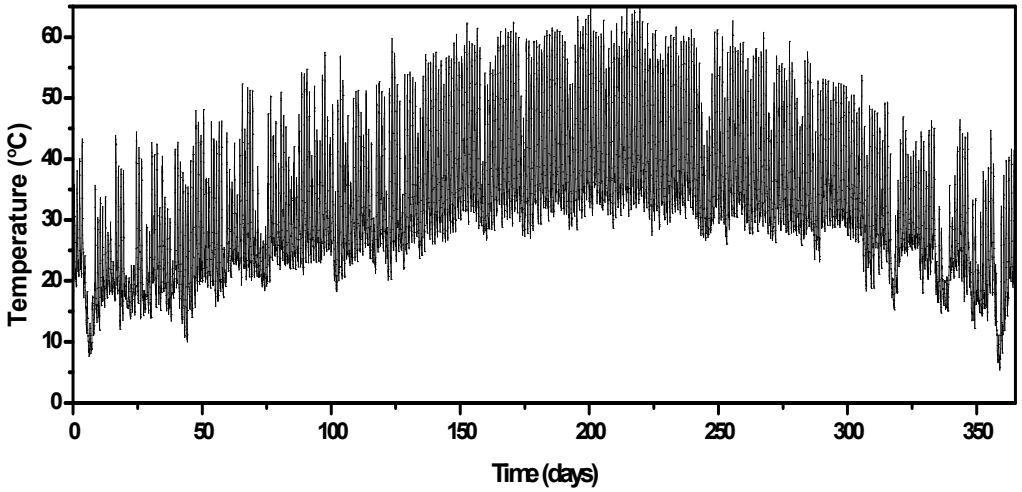

Figure C1-6 Pavement Temperature of US277 at Layer 1

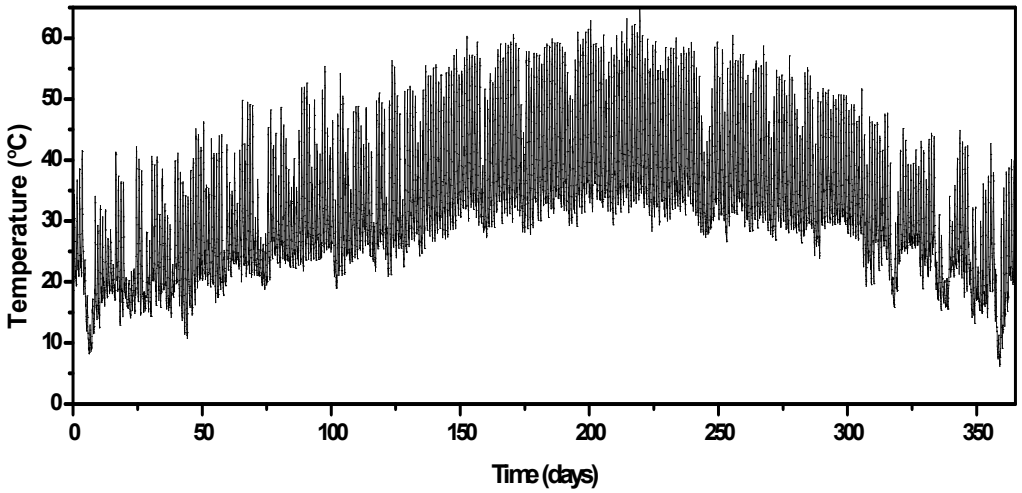

Figure C1-7 Pavement Temperature of US277 at Layer 2

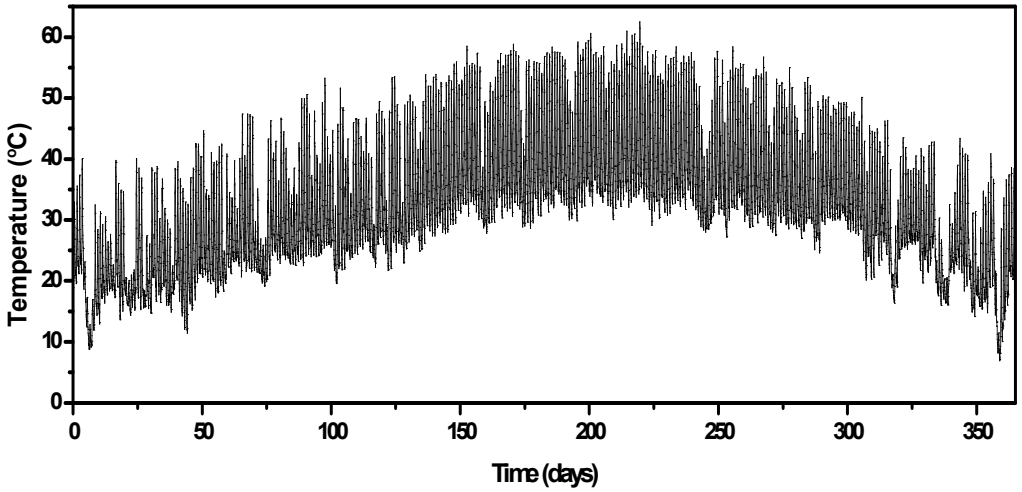

Figure C1-8 Pavement Temperature of US277 at Layer 3

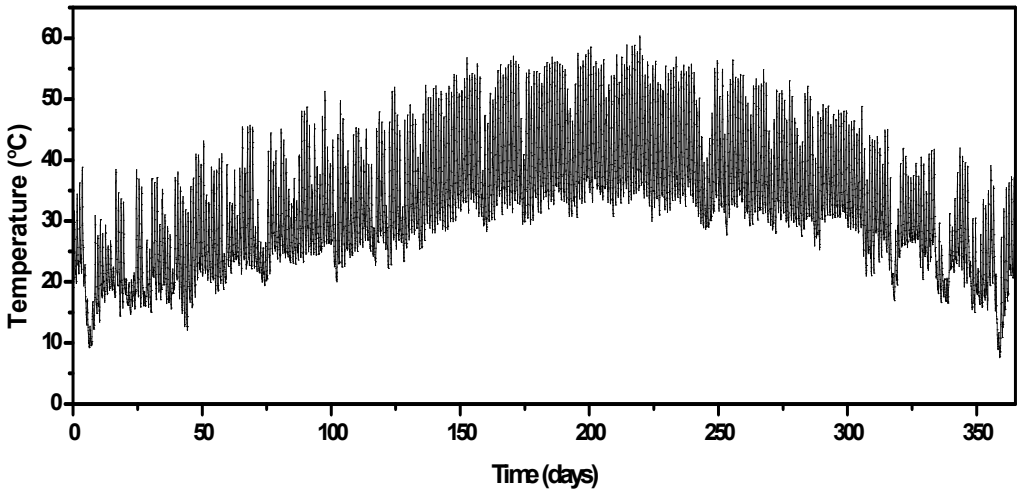

Figure C1-9 Pavement Temperature of US277 at Layer 4

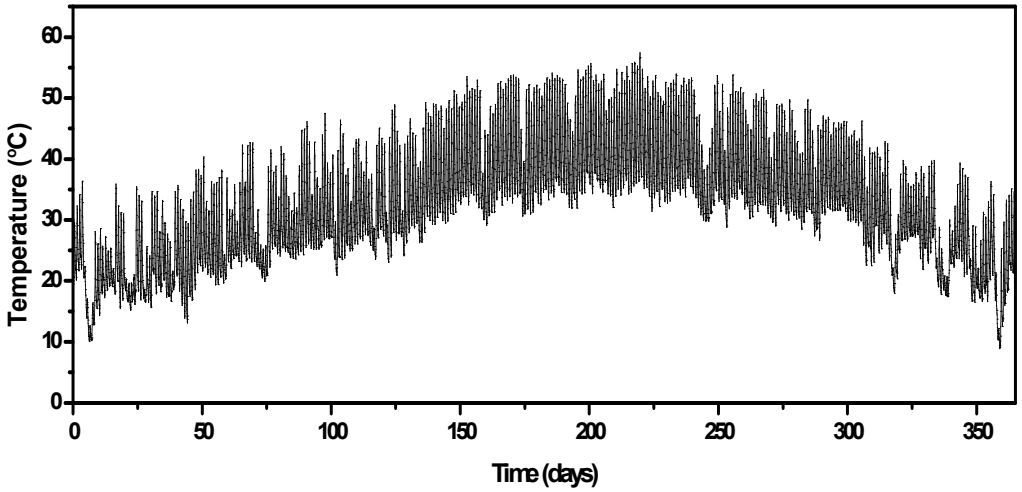

Figure C1-10 Pavement Temperature of US277 at Layer 5

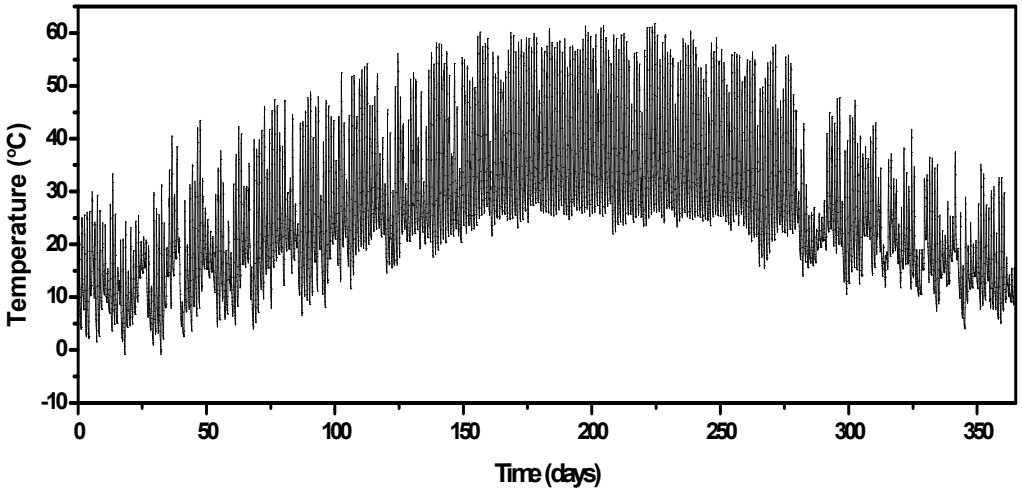

Figure C1-11 Pavement Temperature of US69 at Layer 1

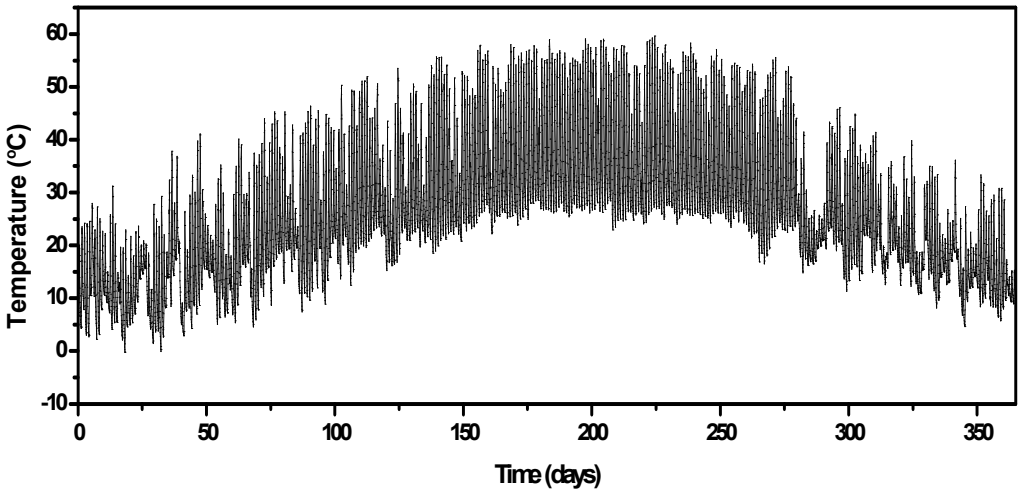

Figure C1-12 Pavement Temperature of US69 at Layer 2

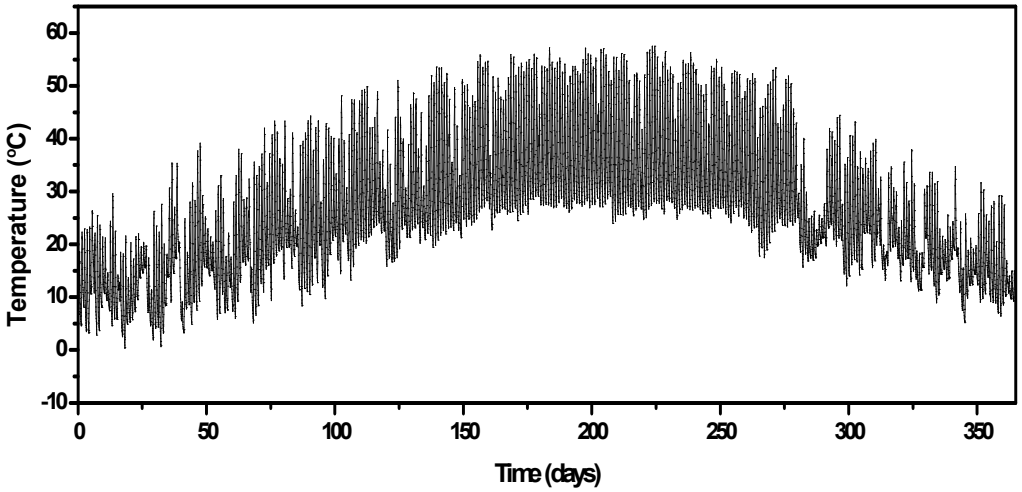

Figure C1-13 Pavement Temperature of US69 at Layer 3

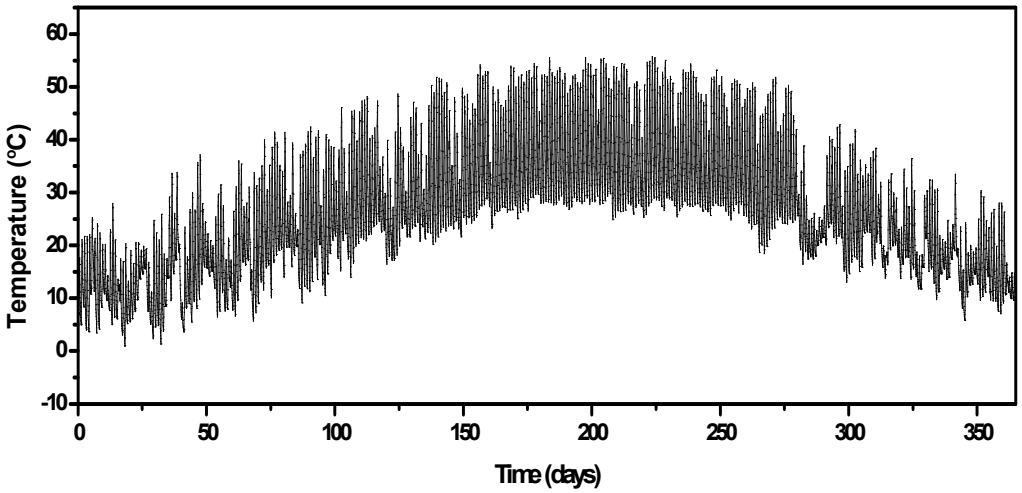

Figure C1-14 Pavement Temperature of US69 at Layer 4

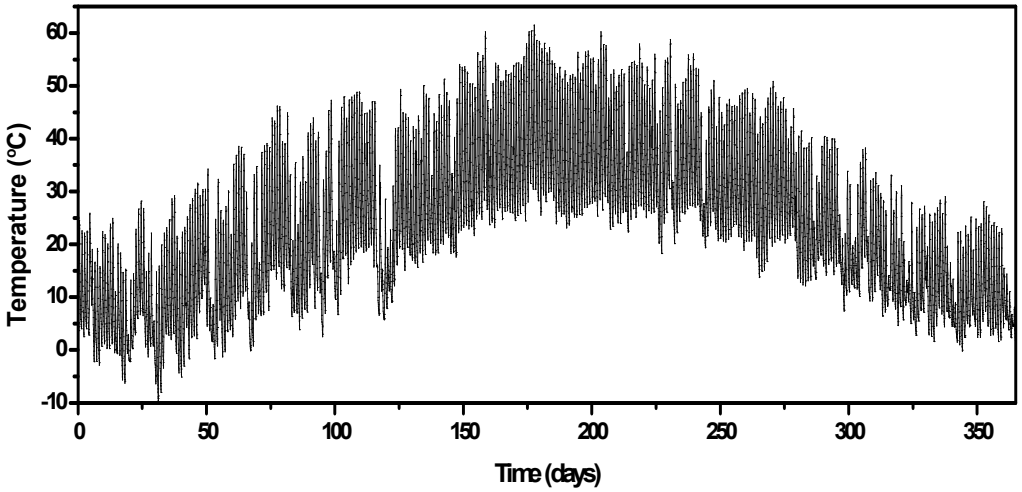

Figure C1-15 Pavement Temperature of US54 at Layer 1

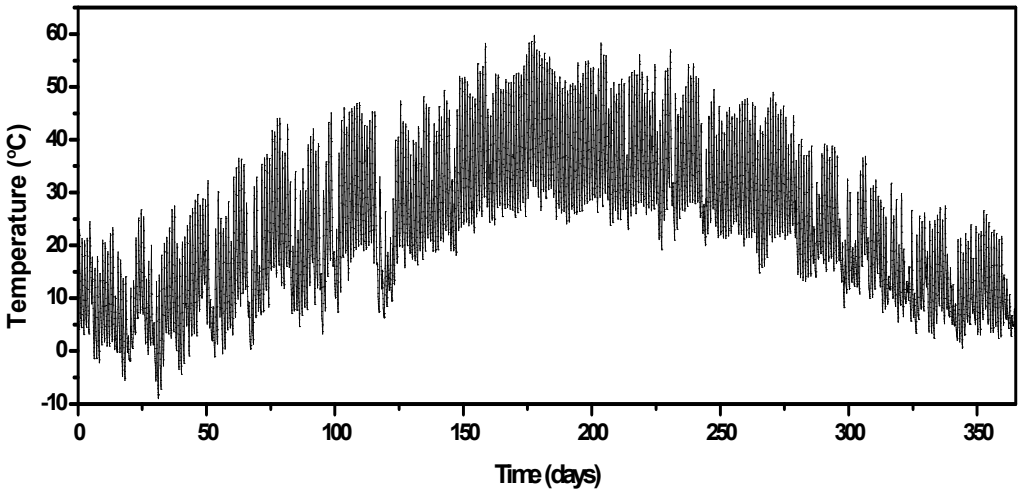

Figure C1-16 Pavement Temperature of US54 at Layer 2

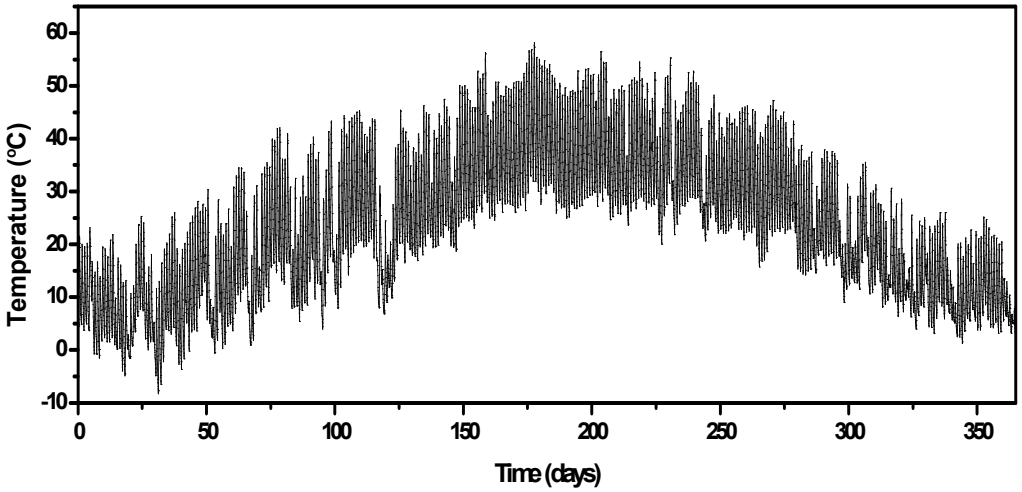

Figure C1-17 Pavement Temperature of US54 at Layer 3

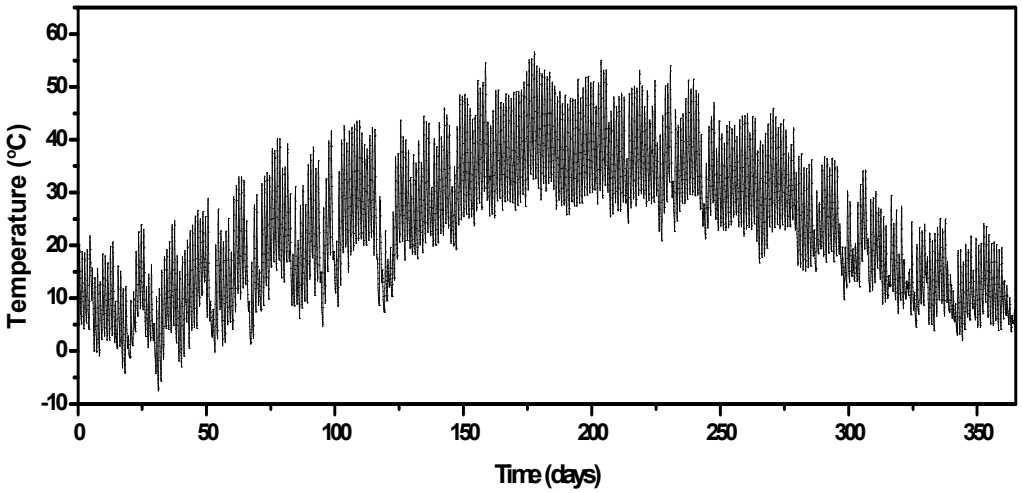

Figure C1-18 Pavement Temperature of US54 at Layer 4

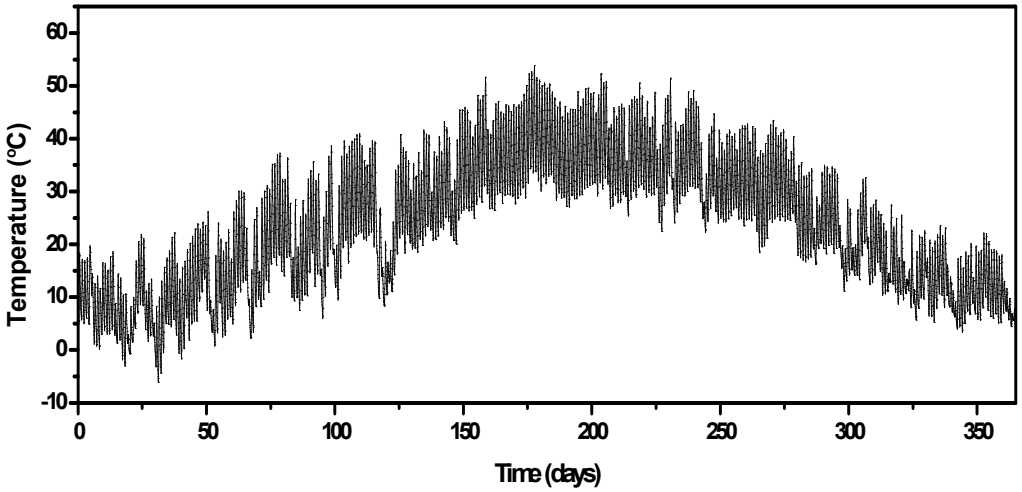

Figure C1-19 Pavement Temperature of US54 at Layer 5

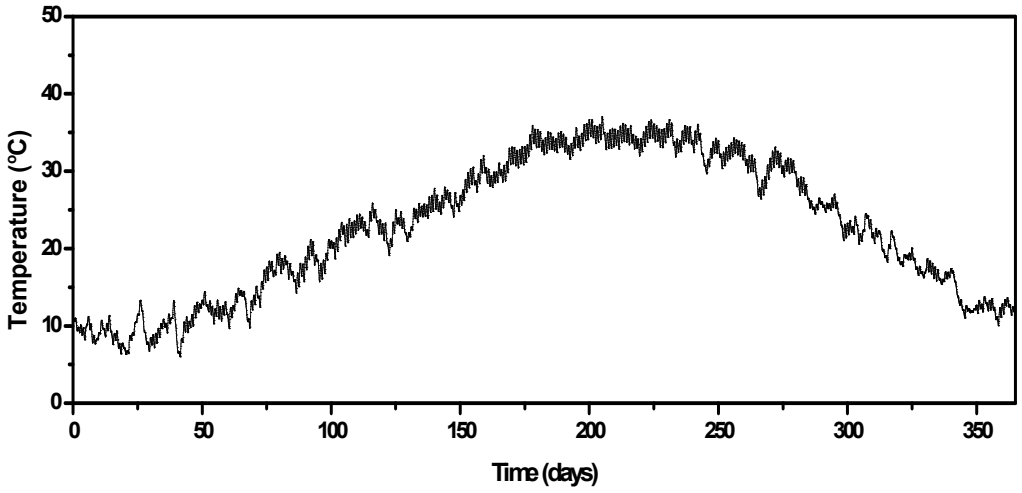

Figure C1-20 Pavement Temperature of IH35-Waco at Layer 1

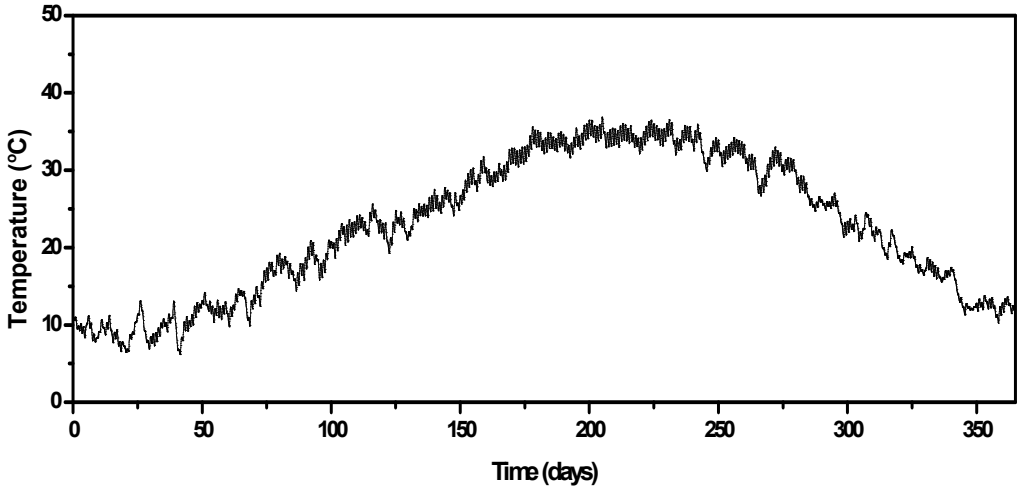

Figure C1-21 Pavement Temperature of IH35-Waco at Layer 2

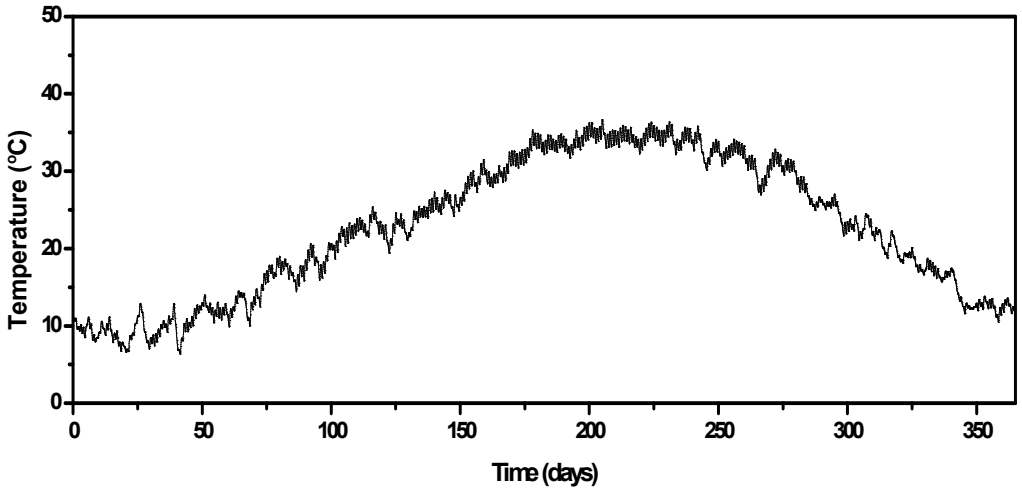

Figure C1-22 Pavement Temperature of IH35-Waco at Layer 3

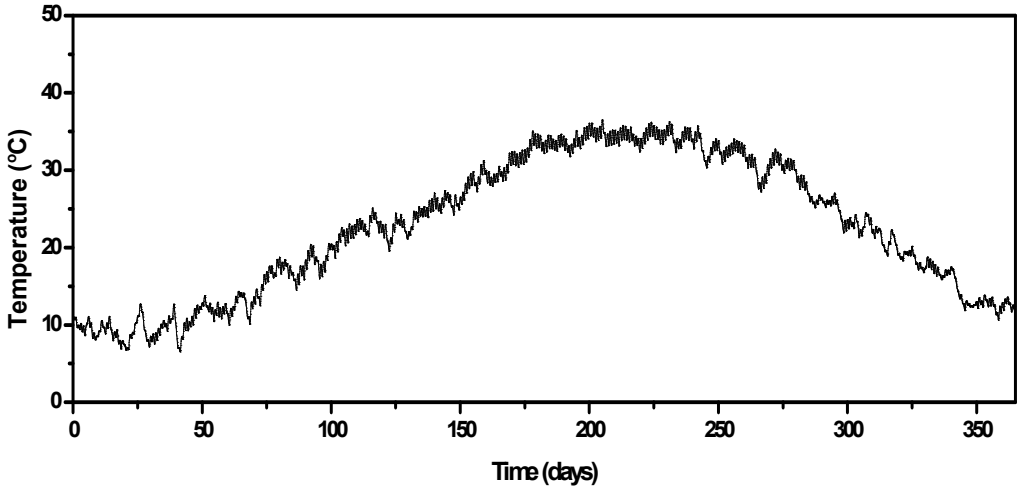

Figure C1-23 Pavement Temperature of IH35-Waco at Layer 4

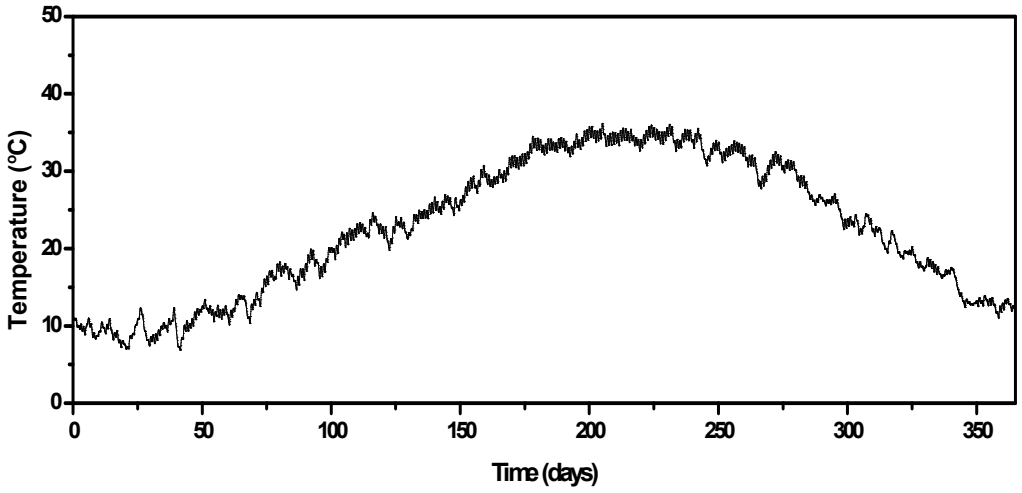

Figure C1-24 Pavement Temperature of IH35-Waco at Layer 5

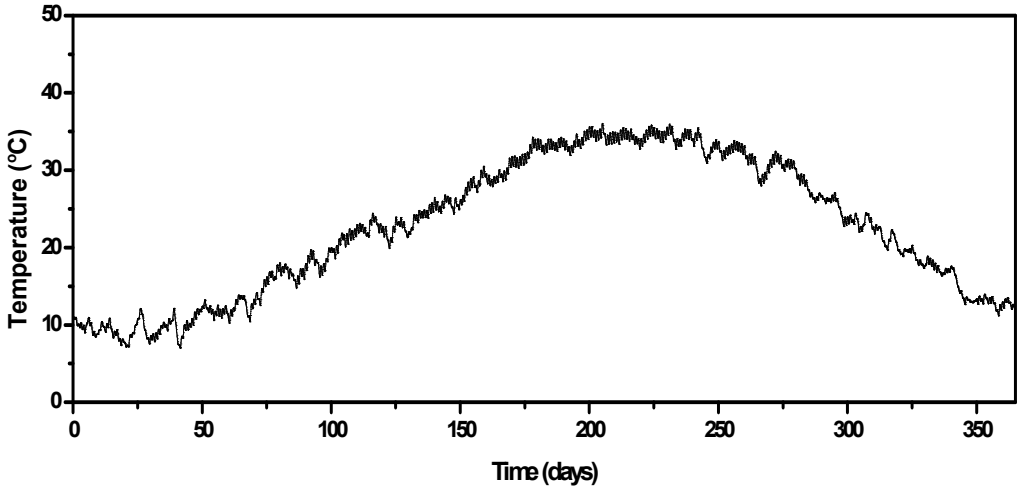

Figure C1-25 Pavement Temperature of IH35-Waco at Layer 6

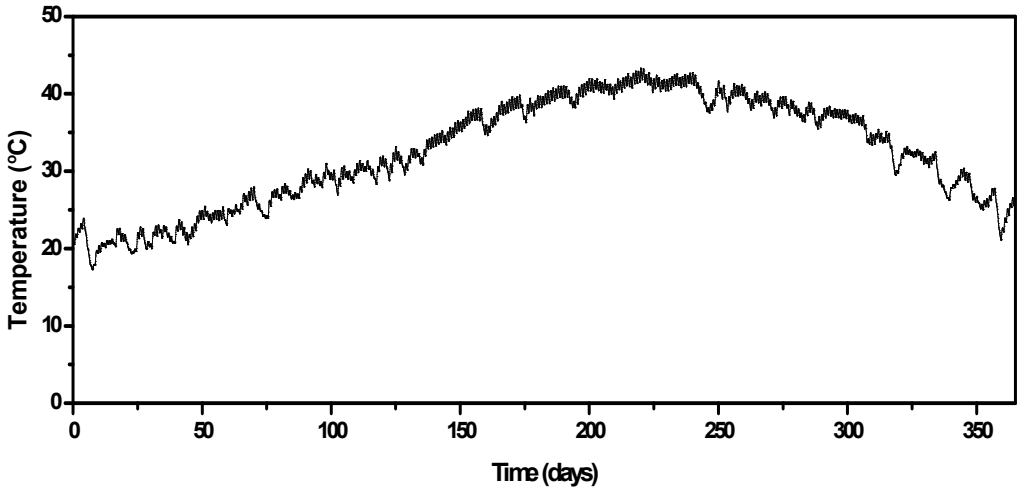

Figure C1-26 Pavement Temperature of IH35-LRD at Layer 1

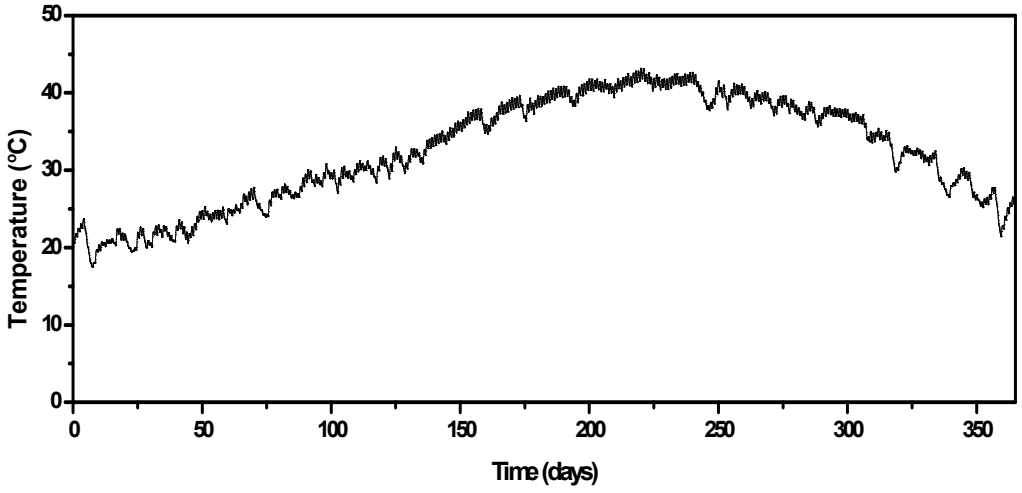

Figure C1-27 Pavement Temperature of IH35-LRD at Layer 2

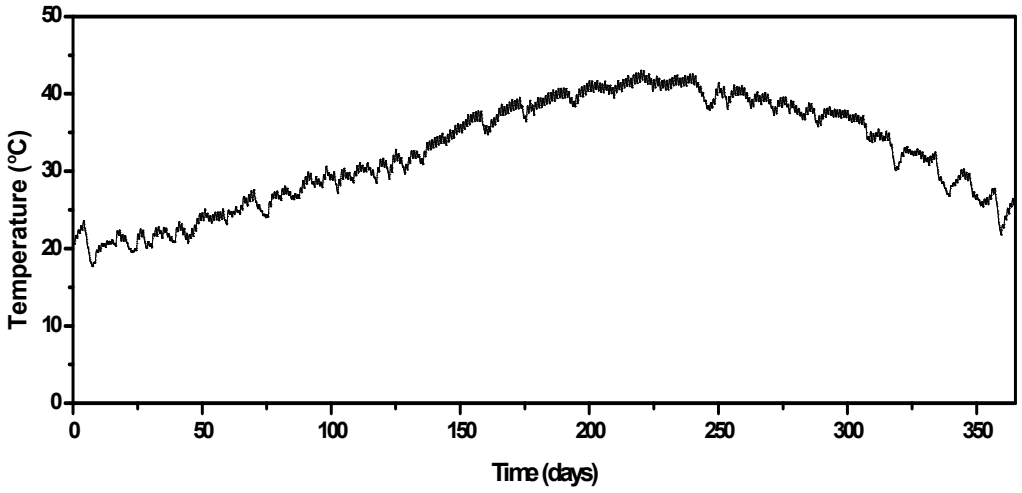

Figure C1-28 Pavement Temperature of IH35-LRD at Layer 3

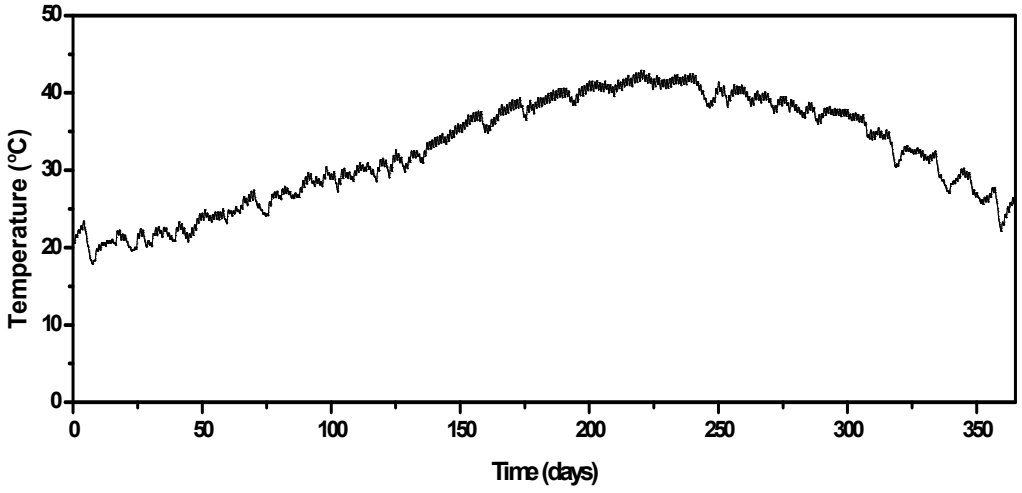

Figure C1-29 Pavement Temperature of IH35-LRD at Layer 4

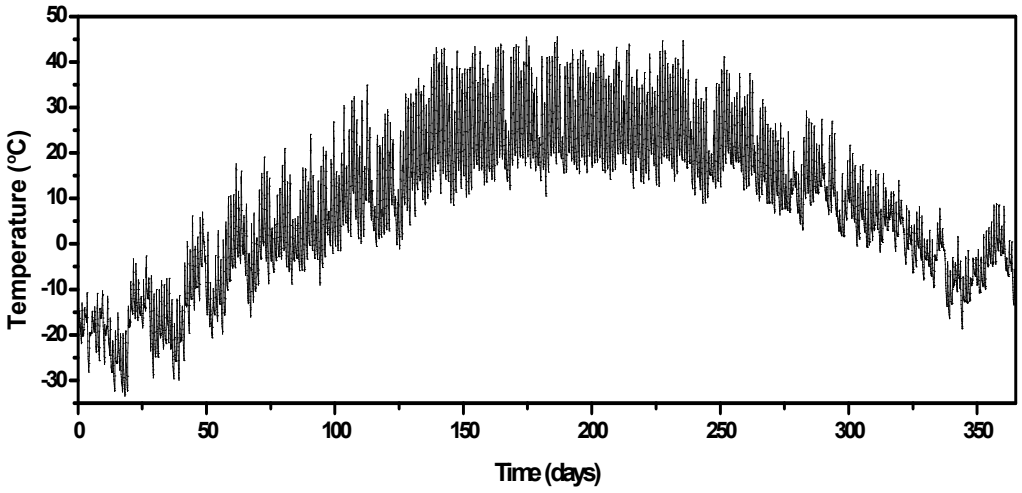

Figure C1-30 Pavement Temperature of MN CELL 1 at Layer 1

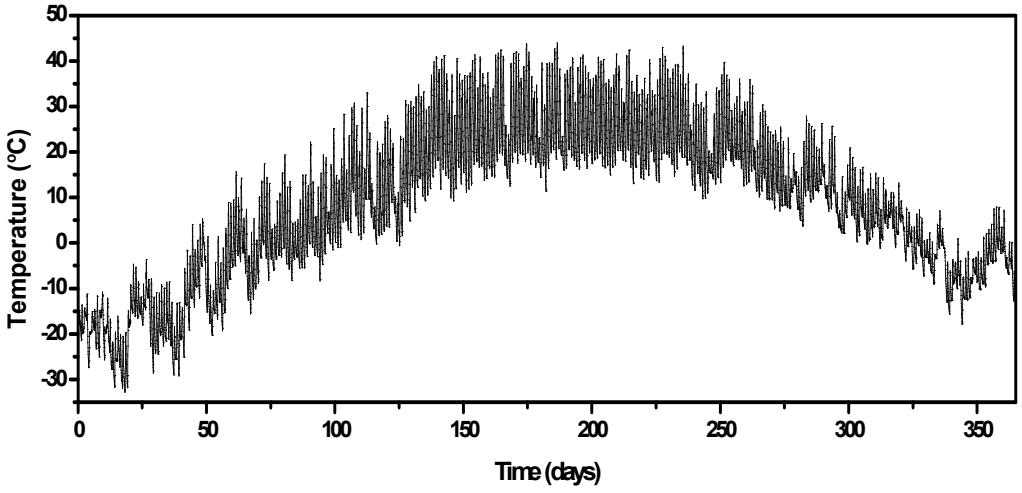

Figure C1-31 Pavement Temperature of MN CELL 1 at Layer 2

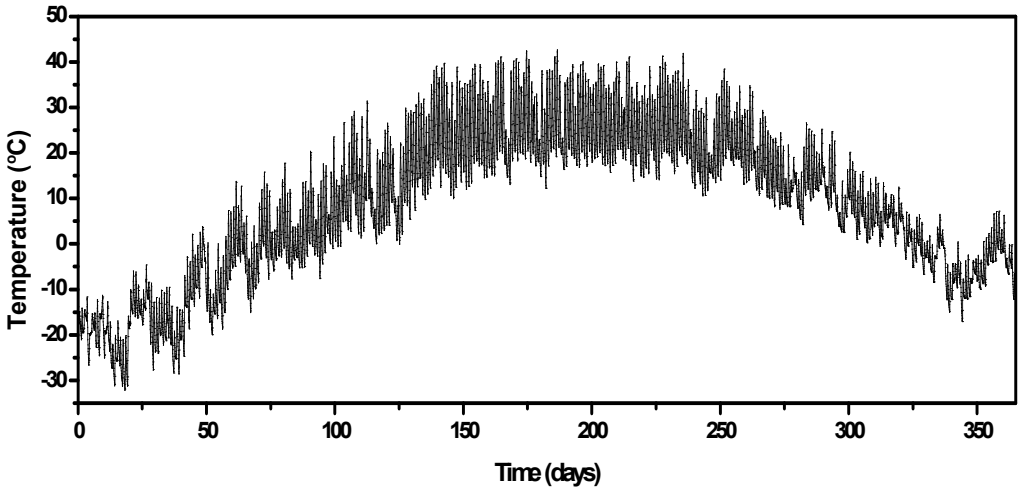

Figure C1-32 Pavement Temperature of MN CELL 1 at Layer 3

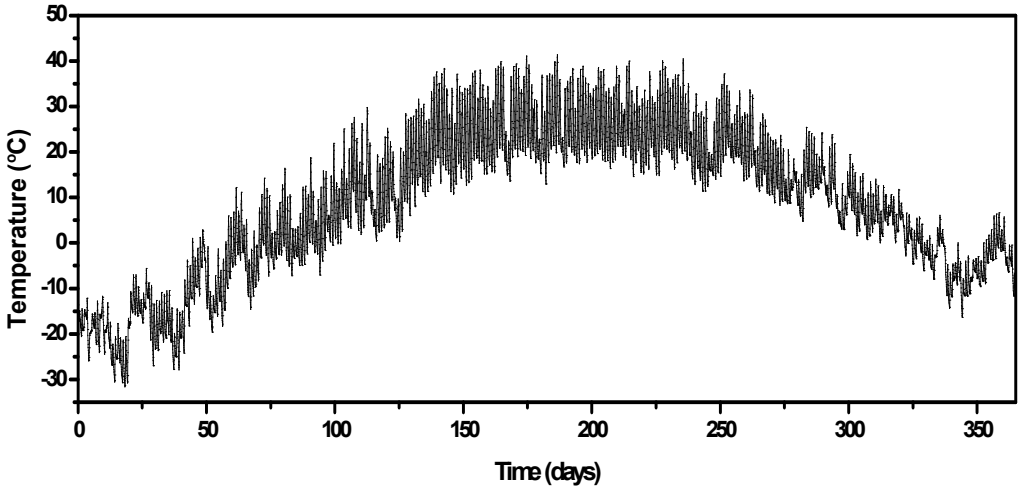

Figure C1-33 Pavement Temperature of MN CELL 1 at Layer 4

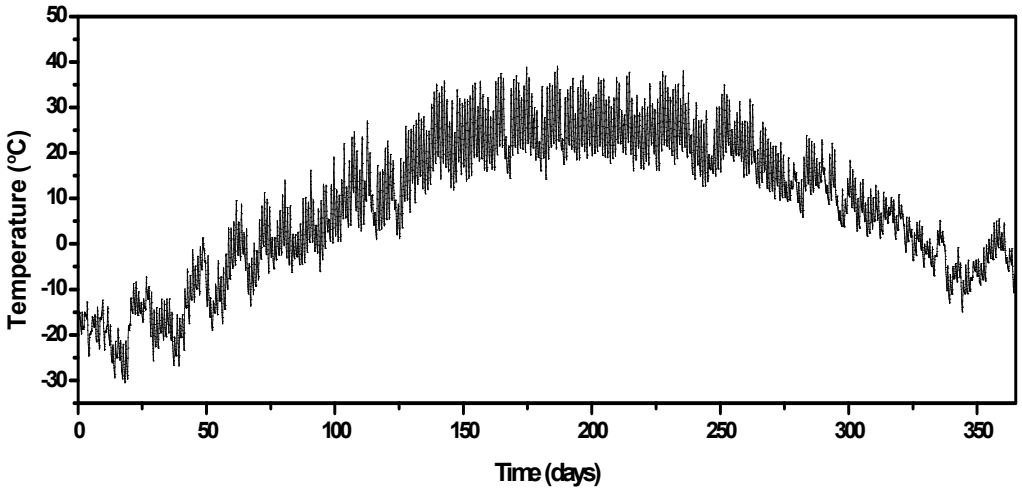

Figure C1-34 Pavement Temperature of MN CELL 1 at Layer 5

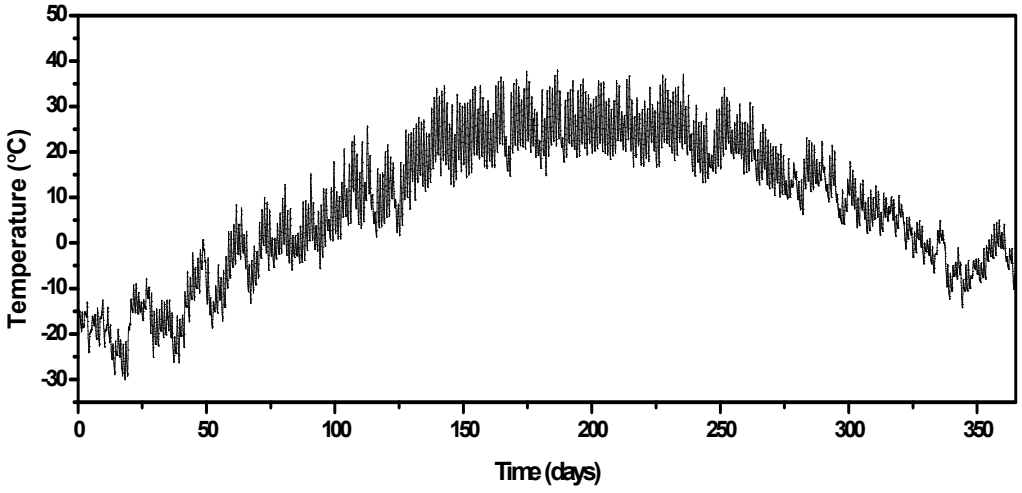

Figure C1-35 Pavement Temperature of MN CELL 1 at Layer 6

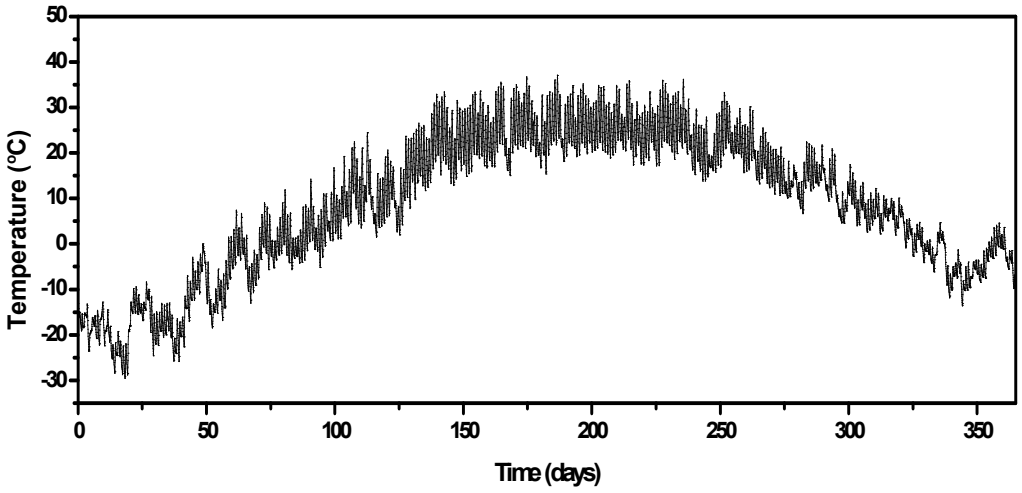

Figure C1-36 Pavement Temperature of MN CELL 1 at Layer 7

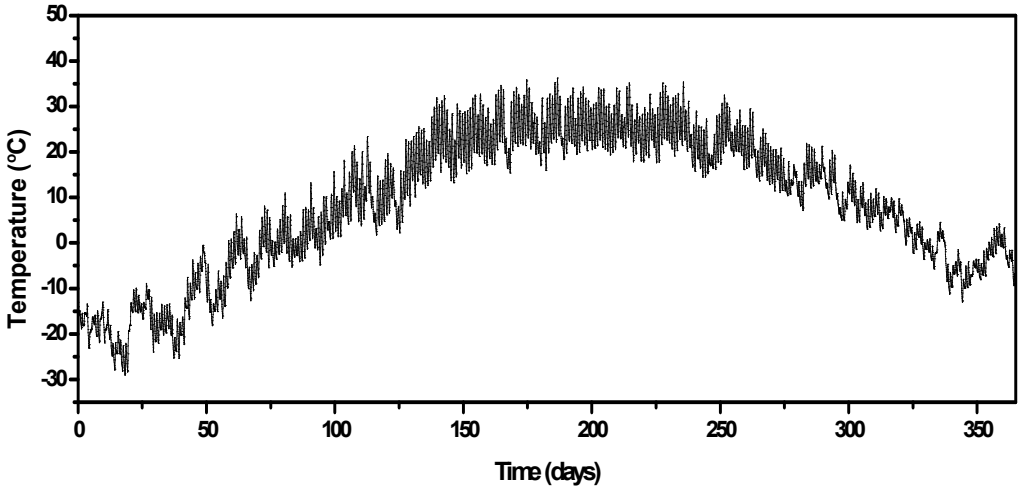

Figure C1-37 Pavement Temperature of MN CELL 1 at Layer 8

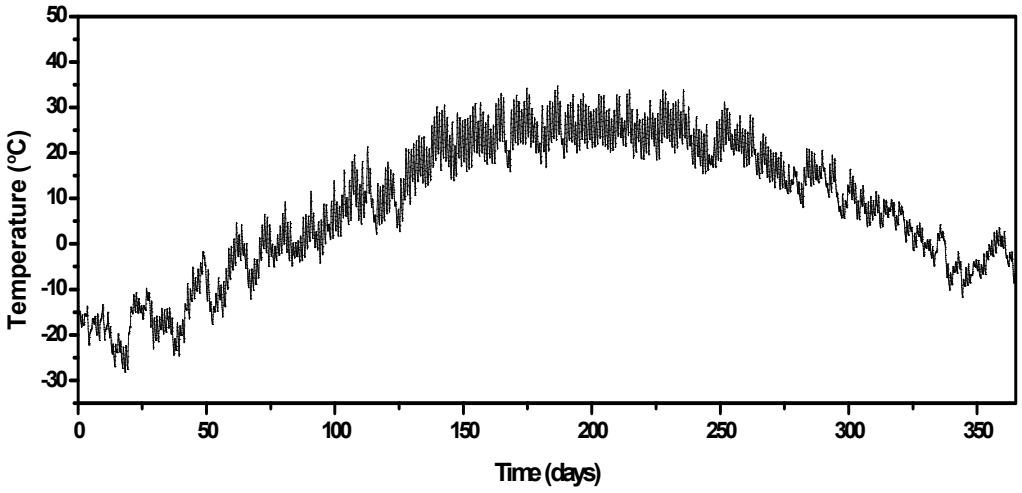

Figure C1-38 Pavement Temperature of MN CELL 1 at Layer 9

Table C2-1 Average air void radius at different pavement layers of US290

Depth	Average Air Void Radius r_i (mm)				
	0~0.2 mm	0.2~0.5 mm	0.5~1 mm	1~2 mm	2~3 mm
Layer 1	0.144	0.352	0.736	1.414	2.455
Layer 2	0.143	0.351	0.739	1.415	2.428
Layer 3	0.145	0.351	0.736	1.422	2.433
Layer 4	0.142	0.353	0.736	1.415	2.443
Layer 5	0.142	0.351	0.721	1.422	2.453

Table C2-2 Number of air voids at different pavement layers of US290

Depth	Number of Air Voids				
	0~0.2 mm	0.2~0.5 mm	0.5~1 mm	1~2 mm	2~3 mm
Layer 1	20	92	128	129	40
Layer 2	19	76	119	115	44
Layer 3	19	66	109	113	41
Layer 4	20	71	104	113	41
Layer 5	18	74	94	89	32

Table B1-3 Shell distance at different pavement layers of US290

Depth	Average Shell Distance r_{NFB} (mm)				
	0~0.2 mm	0.2~0.5 mm	0.5~1 mm	1~2 mm	2~3 mm
Layer 1	11.924	11.924	11.924	11.924	11.924
Layer 2	12.210	12.210	12.210	12.210	12.210
Layer 3	12.421	12.421	12.421	12.421	12.421
Layer 4	12.197	12.197	12.197	12.197	12.197
Layer 5	12.805	12.805	12.805	12.805	12.805

Table C2-4 P_{av} calculated for each air void range at different pavement layers of US290

		P_{av} (atm)				
Depth	**Condition**	**0~0.2 mm**	**0.2~0.5 mm**	**0.5~1 mm**	**1~2 mm**	**2~3 mm**
Layer 1	Upper	0.2	0.2	0.2	0.2	0.2
	Lower	0.107	0.185	0.197	0.199	0.2
Layer 2	Upper	0.2	0.2	0.2	0.2	0.2
	Lower	0.025	0.171	0.193	0.198	0.198
Layer 3	Upper	0.2	0.2	0.2	0.2	0.2
	Lower	0.008	0.158	0.190	0.197	0.197
Layer 4	Upper	0.2	0.2	0.2	0.2	0.2
	Lower	0.000	0.145	0.187	0.196	0.197
Layer 5	Upper	0.2	0.2	0.2	0.2	0.2
	Lower	0.000	0.121	0.183	0.195	0.196

Table C2-5 Average air void radius at different pavement layers of US277

Depth	Average Air Void Radius r_i (mm)				
	0~0.2 mm	0.2~0.5 mm	0.5~1 mm	1~2 mm	2~3 mm
Layer 1	0.140	0.332	0.697	1.338	2.400
Layer 2	0.142	0.331	0.700	1.314	2.290
Layer 3	0.138	0.326	0.695	1.289	2.306
Layer 4	0.141	0.326	0.682	1.284	2.290
Layer 5	0.142	0.330	0.688	1.303	2.385

Table C2-6 Number of air voids at different pavement layers of US277

Depth	Number of Air Voids				
	0~0.2 mm	0.2~0.5 mm	0.5~1 mm	1~2 mm	2~3 mm
Layer 1	34	672	211	83	14
Layer 2	37	744	237	81	6
Layer 3	36	710	216	58	4
Layer 4	37	737	203	47	3
Layer 5	39	781	242	73	7

Table C2-7 Shell distance at different pavement layers of US277

Depth	Average Shell Distance r_{NFB} (mm)				
	0~0.2 mm	0.2~0.5 mm	0.5~1 mm	1~2 mm	2~3 mm
Layer 1	8.931	8.931	8.931	8.931	8.931
Layer 2	8.487	8.487	8.487	8.487	8.487
Layer 3	8.686	8.686	8.686	8.686	8.686
Layer 4	8.530	8.530	8.530	8.530	8.530
Layer 5	8.280	8.280	8.280	8.280	8.280

Table C2-8 P_{av} calculated for each air void range at different pavement layers of US277

		P_{av} (atm)				
Depth	**Condition**	**0~0.2 mm**	**0.2~0.5 mm**	**0.5~1 mm**	**1~2 mm**	**2~3 mm**
Layer 1	Upper	0.2	0.2	0.2	0.2	0.2
	Lower	0.159	0.193	0.199	0.199	0.200
Layer 2	Upper	0.2	0.2	0.2	0.2	0.2
	Lower	0.112	0.186	0.197	0.199	0.200
Layer 3	Upper	0.2	0.2	0.2	0.2	0.2
	Lower	0.082	0.179	0.195	0.199	0.200
Layer 4	Upper	0.2	0.2	0.2	0.2	0.2
	Lower	0.047	0.172	0.194	0.198	0.200
Layer 5	Upper	0.2	0.2	0.2	0.2	0.2
	Lower	0.000	0.161	0.192	0.197	0.199

Table C2-9 Average air void radius at different pavement layers of US69

Depth	Average Air Void Radius r_i (mm)				
	0~0.2 mm	0.2~0.5 mm	0.5~1 mm	1~2 mm	2~3 mm
Layer 1	0.144	0.336	0.700	1.342	2.663
Layer 2	0.144	0.332	0.695	1.328	2.458
Layer 3	0.145	0.330	0.695	1.354	2.625
Layer 4	0.144	0.331	0.704	1.346	2.711

Table C2-10 Number of air voids at different pavement layers of US69

Depth	Number of Air Voids				
	0~0.2 mm	0.2~0.5 mm	0.5~1 mm	1~2 mm	2~3 mm
Layer 1	52	407	240	84	12
Layer 2	49	369	230	86	13
Layer 3	50	390	222	85	15
Layer 4	45	337	194	91	20

Table C2-11 Shell distance at different pavement layers of US69

Depth	Average Shell Distance r_{NFB} (mm)				
	0~0.2 mm	0.2~0.5 mm	0.5~1 mm	1~2 mm	2~3 mm
Layer 1	8.470	8.470	8.470	8.470	8.470
Layer 2	8.742	8.742	8.742	8.742	8.742
Layer 3	8.660	8.660	8.660	8.660	8.660
Layer 4	9.100	9.100	9.100	9.100	9.100

Table C2-12 P_{av} calculated for each air void range at different pavement layers of US69

		P_{av} (atm)				
Depth	**Condition**	**0~0.2 mm**	**0.2~0.5 mm**	**0.5~1 mm**	**1~2 mm**	**2~3 mm**
Layer 1	Upper	0.2	0.2	0.2	0.2	0.2
	Lower	0.193	0.196	0.198	0.200	0.2
Layer 2	Upper	0.2	0.2	0.2	0.2	0.2
	Lower	0.189	0.192	0.196	0.199	0.2
Layer 3	Upper	0.2	0.2	0.2	0.2	0.2
	Lower	0.184	0.188	0.194	0.199	0.2
Layer 4	Upper	0.2	0.2	0.2	0.2	0.2
	Lower	0.181	0.185	0.192	0.199	0.2

Table C2-13 Average air void radius at different pavement layers of US54

Depth	Average Air Void Radius r_i (mm)				
	0~0.2 mm	0.2~0.5 mm	0.5~1 mm	1~2 mm	2~3 mm
Layer 1	0.145	0.322	0.736	1.359	2.423
Layer 2	0.143	0.322	0.693	1.349	2.413
Layer 3	0.145	0.320	0.692	1.355	2.443
Layer 4	0.141	0.323	0.700	1.355	2.432
Layer 5	0.141	0.322	0.700	1.356	2.431

Table C2-14 Number of air voids at different pavement layers of US54

Depth	Number of Air Voids				
	0~0.2 mm	0.2~0.5 mm	0.5~1 mm	1~2 mm	2~3 mm
Layer 1	40	436	246	117	27
Layer 2	45	537	265	108	20
Layer 3	44	542	251	105	21
Layer 4	29	315	172	91	22
Layer 5	29	315	172	91	22

Table C2-15 Shell distance at different pavement layers of US54

Depth	Average Shell Distance r_{NFB} (mm)				
	0~0.2 mm	0.2~0.5 mm	0.5~1 mm	1~2 mm	2~3 mm
Layer 1	8.163	8.163	8.163	8.163	8.163
Layer 2	7.722	7.722	7.722	7.722	7.722
Layer 3	7.763	7.763	7.763	7.763	7.763
Layer 4	9.543	9.543	9.543	9.543	9.543
Layer 5	9.543	9.543	9.543	9.543	9.543

Table C2-16 P_{av} calculated for each air void range at different pavement layers of US54

		P_{av} (atm)				
Depth	**Condition**	**0~0.2 mm**	**0.2~0.5 mm**	**0.5~1 mm**	**1~2 mm**	**2~3 mm**
Layer 1	Upper	0.2	0.2	0.2	0.2	0.2
	Lower	0.113	0.181	0.196	0.199	0.200
Layer 2	Upper	0.2	0.2	0.2	0.2	0.2
	Lower	0.004	0.163	0.193	0.198	0.199
Layer 3	Upper	0.2	0.2	0.2	0.2	0.2
	Lower	0.000	0.146	0.190	0.197	0.199
Layer 4	Upper	0.2	0.2	0.2	0.2	0.2
	Lower	0.000	0.129	0.186	0.196	0.199
Layer 5	Upper	0.2	0.2	0.2	0.2	0.2
	Lower	0.000	0.099	0.182	0.195	0.199

Table C2-17 Average air void radius at different pavement layers of IH35-Waco

Depth	Average Air Void Radius r_i (mm)				
	0~0.2 mm	0.2~0.5 mm	0.5~1 mm	1~2 mm	2~3 mm
Layer 1	0.144	0.340	0.702	1.305	2.276
Layer 2	0.145	0.334	0.690	1.258	2.335
Layer 3	0.145	0.335	0.696	1.284	2.250
Layer 4	0.143	0.334	0.692	1.272	2.315
Layer 5	0.144	0.331	0.706	1.311	2.341
Layer 6	0.144	0.333	0.720	1.351	2.379

Table C2-18 Number of air voids at different pavement layers of IH35-Waco

Depth	Number of Air Voids				
	0~0.2 mm	0.2~0.5 mm	0.5~1 mm	1~2 mm	2~3 mm
Layer 1	23	309	242	85	5
Layer 2	21	287	185	53	3
Layer 3	19	280	161	39	2
Layer 4	19	265	153	42	2
Layer 5	19	248	159	68	5
Layer 6	20	210	177	97	17

Table C2-19 Shell distance at different pavement layers of IH35-Waco

Depth	Average Shell Distance r_{NFB} (mm)				
	0~0.2 mm	0.2~0.5 mm	0.5~1 mm	1~2 mm	2~3 mm
Layer 1	9.182	9.182	9.182	9.182	9.182
Layer 2	10.121	10.121	10.121	10.121	10.121
Layer 3	10.600	10.600	10.600	10.600	10.600
Layer 4	10.820	10.820	10.820	10.820	10.820
Layer 5	10.610	10.610	10.610	10.610	10.610
Layer 6	10.366	10.366	10.366	10.366	10.366

Table C2-20 P_{av} calculated for each air void range at different pavement layers of IH35-Waco

		P_{av} (atm)				
Depth	Condition	0~0.2 mm	0.2~0.5 mm	0.5~1 mm	1~2 mm	2~3 mm
Layer 1	Upper	0.2	0.2	0.2	0.2	0.2
	Lower	0.039	0.125	0.185	0.195	0.199
Layer 2	Upper	0.2	0.2	0.2	0.2	0.2
	Lower	0.000	0.123	0.185	0.195	0.199
Layer 3	Upper	0.2	0.2	0.2	0.2	0.2
	Lower	0.000	0.120	0.184	0.195	0.199
Layer 4	Upper	0.2	0.2	0.2	0.2	0.2
	Lower	0.000	0.119	0.184	0.195	0.199
Layer 5	Upper	0.2	0.2	0.2	0.2	0.2
	Lower	0.000	0.117	0.184	0.194	0.199
Layer 6	Upper	0.2	0.2	0.2	0.2	0.2
	Lower	0.000	0.113	0.183	0.194	0.199

Table C2-21 Average air void radius at different pavement layers of IH35-LRD

Depth	Average Air Void Radius r_i (mm)				
	0~0.2 mm	0.2~0.5 mm	0.5~1 mm	1~2 mm	2~3 mm
Layer 1	0.140	0.350	0.713	1.308	2.407
Layer 2	0.144	0.347	0.716	1.302	2.434
Layer 3	0.145	0.343	0.722	1.285	2.301
Layer 4	0.144	0.344	0.723	1.188	2.305

Table C2-22 Number of air voids at different pavement layers of IH35-LRD

Depth	Number of Air Voids				
	0~0.2 mm	0.2~0.5 mm	0.5~1 mm	1~2 mm	2~3 mm
Layer 1	8	80	92	31	2
Layer 2	7	70	70	25	2
Layer 3	7	71	81	31	3
Layer 4	7	72	82	33	2

Table C2-23 Shell distance at different pavement layers of IH35-LRD

Depth	Average Shell Distance r_{NFB} (mm)				
	0~0.2 mm	0.2~0.5 mm	0.5~1 mm	1~2 mm	2~3 mm
Layer 1	16.128	16.128	16.128	16.128	16.128
Layer 2	17.826	17.826	17.826	17.826	17.826
Layer 3	16.891	16.891	16.891	16.891	16.891
Layer 4	17.001	17.001	17.001	17.001	17.001

Table C2-24 P_{av} calculated for each air void range at different pavement layers of IH35-LRD

		P_{av} (atm)				
Depth	**Condition**	**0~0.2 mm**	**0.2~0.5 mm**	**0.5~1 mm**	**1~2 mm**	**2~3 mm**
Layer 1	Upper	0.2	0.2	0.2	0.2	0.2
	Lower	0.000	0.012	0.135	0.181	0.194
Layer 2	Upper	0.2	0.2	0.2	0.2	0.2
	Lower	0.000	0.004	0.132	0.181	0.194
Layer 3	Upper	0.2	0.2	0.2	0.2	0.2
	Lower	0.000	0.000	0.130	0.180	0.194
Layer 4	Upper	0.2	0.2	0.2	0.2	0.2
	Lower	0.000	0.000	0.129	0.180	0.194

Table C2-25 Average air void radius at different pavement layers of MN Cell 1

Depth	Average Air Void Radius r_i (mm)				
	0~0.2 mm	0.2~0.5 mm	0.5~1 mm	1~2 mm	2~3 mm
Layer 1	0.144	0.327	0.679	1.336	2.470
Layer 2	0.143	0.323	0.675	1.311	2.340
Layer 3	0.145	0.322	0.678	1.316	2.394
Layer 4	0.142	0.324	0.676	1.313	2.401
Layer 5	0.142	0.321	0.679	1.334	2.407
Layer 6	0.143	0.320	0.678	1.331	2.462
Layer 7	0.142	0.320	0.674	1.320	2.417
Layer 8	0.146	0.320	0.683	1.326	2.423
Layer 9	0.146	0.322	0.677	1.339	2.428

Table C2-26 Number of air voids at different pavement layers of MN Cell 1

Depth	Number of Air Voids				
	0~0.2 mm	0.2~0.5 mm	0.5~1 mm	1~2 mm	2~3 mm
Layer 1	95	909	327	97	18
Layer 2	94	921	321	84	8
Layer 3	91	894	305	87	12
Layer 4	93	916	310	83	12
Layer 5	93	911	309	87	14
Layer 6	95	953	309	79	13
Layer 7	92	921	302	73	10
Layer 8	77	748	263	68	10
Layer 9	73	707	238	77	16

Table C2-27 Shell distance at different pavement layers of MN Cell 1

Depth	Average Shell Distance r_{NFB} (mm)				
	0~0.2 mm	0.2~0.5 mm	0.5~1 mm	1~2 mm	2~3 mm
Layer 1	6.226	6.226	6.226	6.226	6.226
Layer 2	6.273	6.273	6.273	6.273	6.273
Layer 3	6.357	6.357	6.357	6.357	6.357
Layer 4	6.301	6.301	6.301	6.301	6.301
Layer 5	6.296	6.296	6.296	6.296	6.296
Layer 6	6.224	6.224	6.224	6.224	6.224
Layer 7	6.337	6.337	6.337	6.337	6.337
Layer 8	6.926	6.926	6.926	6.926	6.926
Layer 9	7.089	7.089	7.089	7.089	7.089

Table C2-28 P_{av} for each air void range at different pavement layers of MN Cell 1

		P_{av} (atm)				
Depth	**Condition**	**0~0.2 mm**	**0.2~0.5 mm**	**0.5~1 mm**	**1~2 mm**	**2~3 mm**
Layer 1	Upper	0.2	0.2	0.2	0.2	0.2
	Lower	0.184	0.197	0.199	0.2	0.2
Layer 2	Upper	0.2	0.2	0.2	0.2	0.2
	Lower	0.168	0.194	0.199	0.2	0.2
Layer 3	Upper	0.2	0.2	0.2	0.2	0.2
	Lower	0.154	0.191	0.198	0.2	0.2
Layer 4	Upper	0.2	0.2	0.2	0.2	0.2
	Lower	0.140	0.188	0.198	0.2	0.2
Layer 5	Upper	0.2	0.2	0.2	0.2	0.2
	Lower	0.120	0.185	0.197	0.199	0.2
Layer 6	Upper	0.2	0.2	0.2	0.2	0.2
	Lower	0.101	0.181	0.197	0.199	0.2
Layer 7	Upper	0.2	0.2	0.2	0.2	0.2
	Lower	0.088	0.178	0.196	0.199	0.2
Layer 8	Upper	0.2	0.2	0.2	0.2	0.2
	Lower	0.073	0.175	0.196	0.198	0.2
Layer 9	Upper	0.2	0.2	0.2	0.2	0.2
	Lower	0.066	0.173	0.196	0.198	0.2

Table C3-1 Oxidation rates calculated at different pavement layers of US290

		r_{O2} (CA/year)					
Depth	**Condition**	**0~0.2 mm**	**0.2~0.5 mm**	**0.5~1 mm**	**1~2 mm**	**2~3 mm**	**Bulk**
Layer 1	Highest	0.0723	0.0741	0.0765	0.0793	0.0820	0.0771
	Lowest	0.0611	0.0726	0.0760	0.0792	0.0820	0.0761
Layer 2	Highest	0.0651	0.0667	0.0689	0.0715	0.0740	0.0697
	Lowest	0.0371	0.0639	0.0682	0.0713	0.0738	0.0674
Layer 3	Highest	0.0596	0.0611	0.0632	0.0656	0.0679	0.0639
	Lowest	0.0250	0.0573	0.0623	0.0652	0.0676	0.0610
Layer 4	Highest	0.0554	0.0568	0.0587	0.0610	0.0632	0.0593
	Lowest	0.0000	0.0520	0.0576	0.0607	0.0629	0.0550
Layer 5	Highest	0.0520	0.0534	0.0553	0.0574	0.0595	0.0557
	Lowest	0.0000	0.0466	0.0539	0.0570	0.0592	0.0506

Table C3-2 Oxidation rates calculated at different pavement layers of US277

		r_{O2} (CA/year)					
Depth	**Condition**	**0~0.2 mm**	**0.2~0.5 mm**	**0.5~1 mm**	**1~2 mm**	**2~3 mm**	**Bulk**
Layer 1	Highest	0.0450	0.0500	0.0566	0.0636	0.0709	0.0526
	Lowest	0.0420	0.0497	0.0565	0.0636	0.0709	0.0524
Layer 2	Highest	0.0420	0.0467	0.0529	0.0595	0.0700	0.0489
	Lowest	0.0356	0.0457	0.0526	0.0594	0.0700	0.0480
Layer 3	Highest	0.0398	0.0442	0.0500	0.0562	0.0696	0.0460
	Lowest	0.0357	0.0428	0.0498	0.0562	0.0696	0.0447
Layer 4	Highest	0.0380	0.0422	0.0478	0.0537	0.0693	0.0437
	Lowest	0.0263	0.0405	0.0473	0.0535	0.0693	0.0420
Layer 5	Highest	0.0355	0.0394	0.0446	0.0501	0.0689	0.0411
	Lowest	0.0000	0.0370	0.0441	0.0496	0.0689	0.0382

Table C3-3 Oxidation rates calculated at different pavement layers of US69

		r_{O2} (CA/year)					
Depth	**Condition**	**0~0.2 mm**	**0.2~0.5 mm**	**0.5~1 mm**	**1~2 mm**	**2~3 mm**	**Bulk**
Layer 1	Highest	0.0252	0.0277	0.0312	0.0352	0.0391	0.0296
	Lowest	0.0247	0.0275	0.0311	0.0352	0.0391	0.0294
Layer 2	Highest	0.0226	0.0249	0.0280	0.0316	0.0351	0.0267
	Lowest	0.0219	0.0246	0.0278	0.0316	0.0351	0.0264
Layer 3	Highest	0.0206	0.0228	0.0256	0.0288	0.0320	0.0243
	Lowest	0.0197	0.0224	0.0254	0.0288	0.0320	0.0239
Layer 4	Highest	0.0191	0.0211	0.0237	0.0267	0.0297	0.0227
	Lowest	0.0181	0.0206	0.0234	0.0267	0.0297	0.0223

Table C3-4 Oxidation rates calculated at different pavement layers of US54

		r_{O2} (CA/year)					
Depth	**Condition**	**0~0.2 mm**	**0.2~0.5 mm**	**0.5~1 mm**	**1~2 mm**	**2~3 mm**	**Bulk**
Layer 1	Highest	0.1050	0.1145	0.1226	0.1323	0.1408	0.1198
	Lowest	0.0946	0.1114	0.1219	0.1321	0.1408	0.1174
Layer 2	Highest	0.1069	0.1108	0.1186	0.1280	0.1362	0.1151
	Lowest	0.0691	0.1048	0.1039	0.1276	0.1362	0.1061
Layer 3	Highest	0.1040	0.1079	0.1154	0.1246	0.1324	0.1119
	Lowest	0.0000	0.0991	0.0977	0.1239	0.1323	0.0976
Layer 4	Highest	0.0983	0.1034	0.1094	0.1168	0.1242	0.1075
	Lowest	0.0000	0.0919	0.0901	0.1161	0.1241	0.0918
Layer 5	Highest	0.0952	0.1001	0.1058	0.1129	0.1200	0.1040
	Lowest	0.0000	0.0828	0.0807	0.1121	0.1198	0.0839

Table C3-5 Oxidation rates calculated at different pavement layers of IH35-Waco

	r_{O2} (CA/year)						
Depth	**Condition**	**0~0.2 mm**	**0.2~0.5 mm**	**0.5~1 mm**	**1~2 mm**	**2~3 mm**	**Bulk**
Layer 1	Highest	0.0251	0.0262	0.0272	0.0280	0.0304	0.0268
	Lowest	0.0171	0.024	0.0266	0.0277	0.0304	0.0253
Layer 2	Highest	0.0249	0.0260	0.0270	0.0278	0.0302	0.0266
	Lowest	0.0000	0.0239	0.0264	0.0275	0.0302	0.0243
Layer 3	Highest	0.0248	0.0259	0.0269	0.0277	0.0301	0.0264
	Lowest	0.0000	0.0237	0.0263	0.0275	0.0301	0.0240
Layer 4	Highest	0.0247	0.0258	0.0268	0.0276	0.0300	0.0263
	Lowest	0.0000	0.0237	0.0262	0.0274	0.0300	0.0240
Layer 5	Highest	0.0244	0.0256	0.0265	0.0273	0.0297	0.0262
	Lowest	0.0000	0.0235	0.0259	0.0271	0.0297	0.0240
Layer 6	Highest	0.0243	0.0255	0.0264	0.0272	0.0296	0.0263
	Lowest	0.0000	0.0234	0.0257	0.0271	0.0296	0.0242

Table C3-6 Oxidation rates calculated at different pavement layers of IH35-LRD

		r_{O2} (CA/year)					
Depth	**Condition**	**0~0.2 mm**	**0.2~0.5 mm**	**0.5~1 mm**	**1~2 mm**	**2~3 mm**	**Bulk**
Layer 1	Highest	0.0331	0.0357	0.0393	0.0432	0.0486	0.0384
	Lowest	0.0000	0.0167	0.0353	0.0420	0.0483	0.0281
Layer 2	Highest	0.0330	0.0357	0.0392	0.0431	0.0485	0.0382
	Lowest	0.0000	0.0124	0.0351	0.0419	0.0482	0.0257
Layer 3	Highest	0.0330	0.0356	0.0392	0.0431	0.0485	0.0384
	Lowest	0.0000	0.0000	0.0349	0.0419	0.0482	0.0221
Layer 4	Highest	0.0330	0.0356	0.0391	0.0430	0.0484	0.0384
	Lowest	0.0000	0.0000	0.0348	0.0419	0.0482	0.0221

Table C3-7 Oxidation rates calculated at different pavement layers of MN Cell 1

		r_{O2} (CA/year)					
Depth	**Condition**	**0~0.2 mm**	**0.2~0.5 mm**	**0.5~1 mm**	**1~2 mm**	**2~3 mm**	**Bulk**
Layer 1	Highest	0.0236	0.0239	0.0242	0.0234	0.0239	0.0239
	Lowest	0.0231	0.0238	0.0241	0.0234	0.0239	0.0238
Layer 2	Highest	0.0223	0.0225	0.0229	0.0221	0.0225	0.0226
	Lowest	0.0213	0.0223	0.0228	0.0221	0.0225	0.0224
Layer 3	Highest	0.0212	0.0215	0.0219	0.0210	0.0215	0.0215
	Lowest	0.0198	0.0212	0.0217	0.0210	0.0215	0.0212
Layer 4	Highest	0.0203	0.0206	0.0210	0.0201	0.0206	0.0206
	Lowest	0.0185	0.0202	0.0208	0.0201	0.0206	0.0202
Layer 5	Highest	0.0190	0.0192	0.0196	0.0188	0.0192	0.0192
	Lowest	0.0165	0.0188	0.0194	0.0188	0.0192	0.0188
Layer 6	Highest	0.0185	0.0187	0.0189	0.0183	0.0187	0.0187
	Lowest	0.0153	0.0181	0.0188	0.0182	0.0187	0.0182
Layer 7	Highest	0.0180	0.0182	0.0186	0.0179	0.0183	0.0182
	Lowest	0.0144	0.0177	0.0184	0.0178	0.0183	0.0176
Layer 8	Highest	0.0176	0.0178	0.0182	0.0175	0.0179	0.0178
	Lowest	0.0134	0.0172	0.0180	0.0174	0.0179	0.0171
Layer 9	Highest	0.0169	0.0172	0.0176	0.0168	0.0172	0.0172
	Lowest	0.0126	0.0165	0.0173	0.0166	0.0172	0.0164

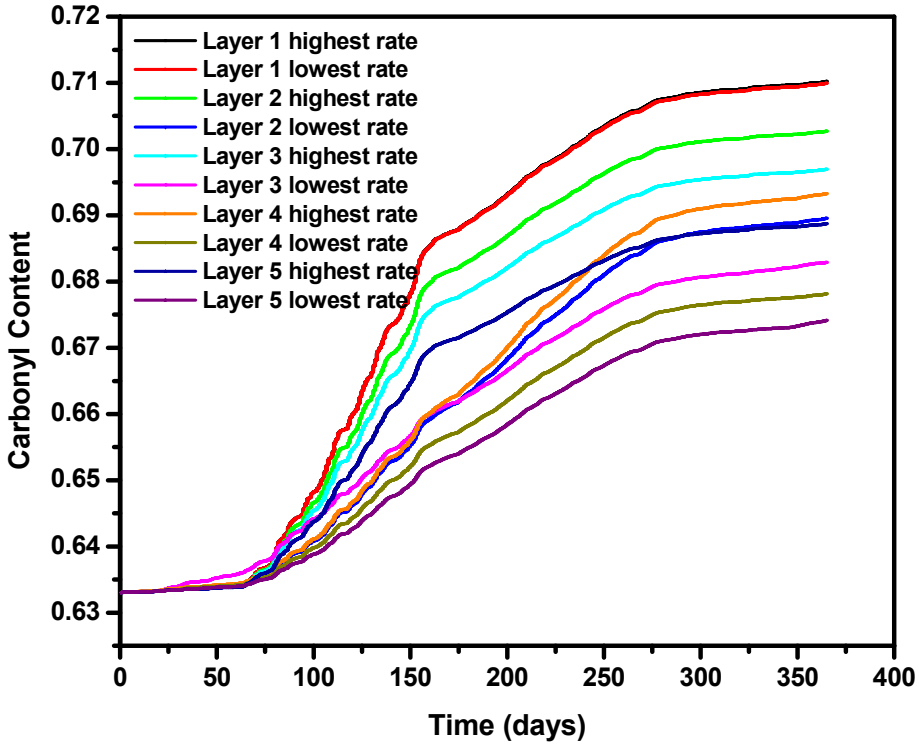

Figure C3-1 Bulk carbonyl growth rates (oxidation rates) of US290 for one year period at different pavement layers

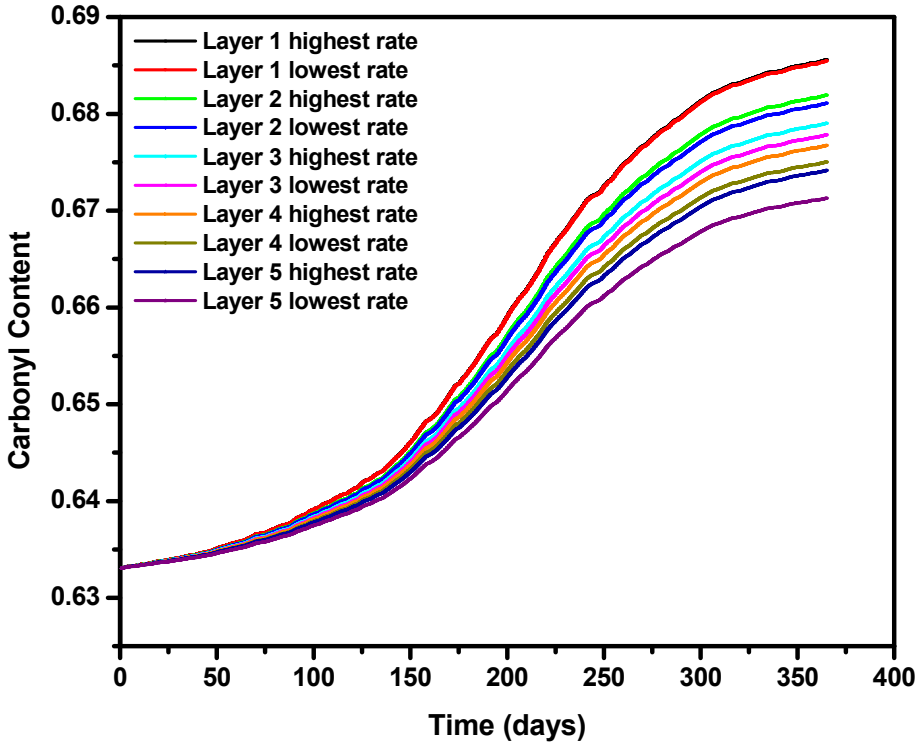

Figure C3-2 Bulk carbonyl growth rates (oxidation rates) of US277 for one year period at different pavement layers

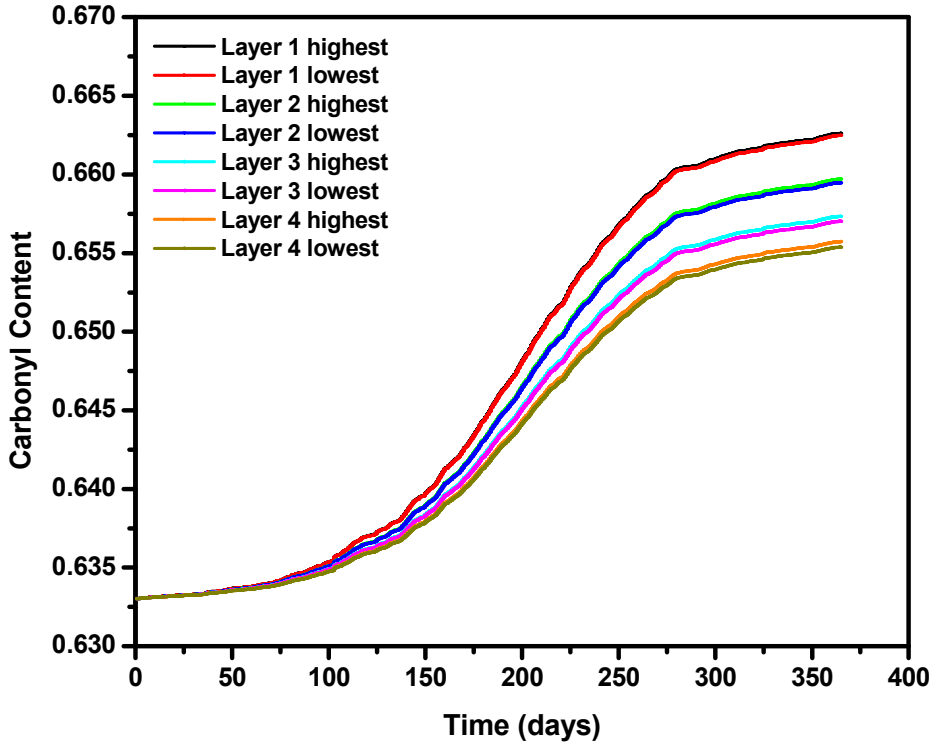

Figure C3-3 Bulk carbonyl growth rates (oxidation rates) of US69 for one year period at different pavement layers

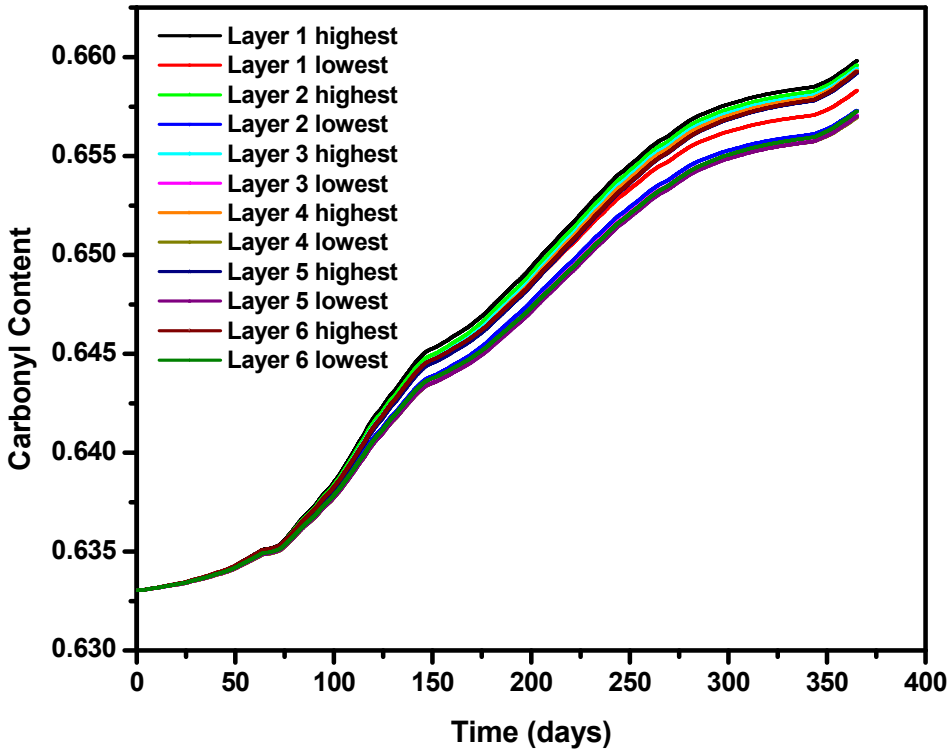

Figure C3-4 Bulk carbonyl growth rates (oxidation rates) of IH35-Waco for one year period at different pavement layers

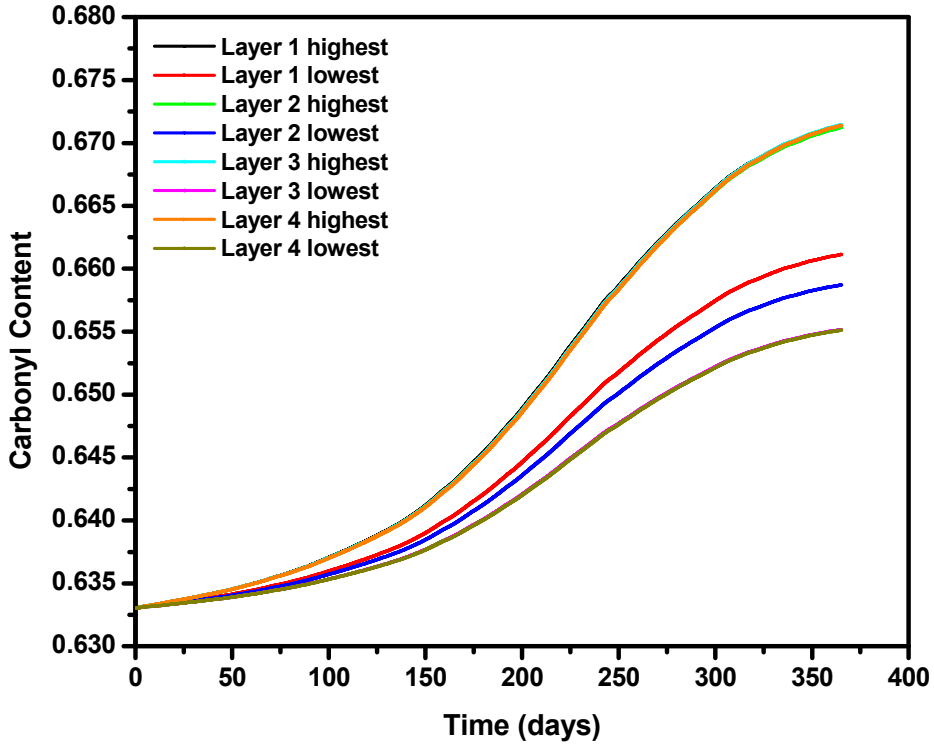

Figure C3-5 Bulk carbonyl growth rates (oxidation rates) of IH35-LRD for one year period at different pavement layers

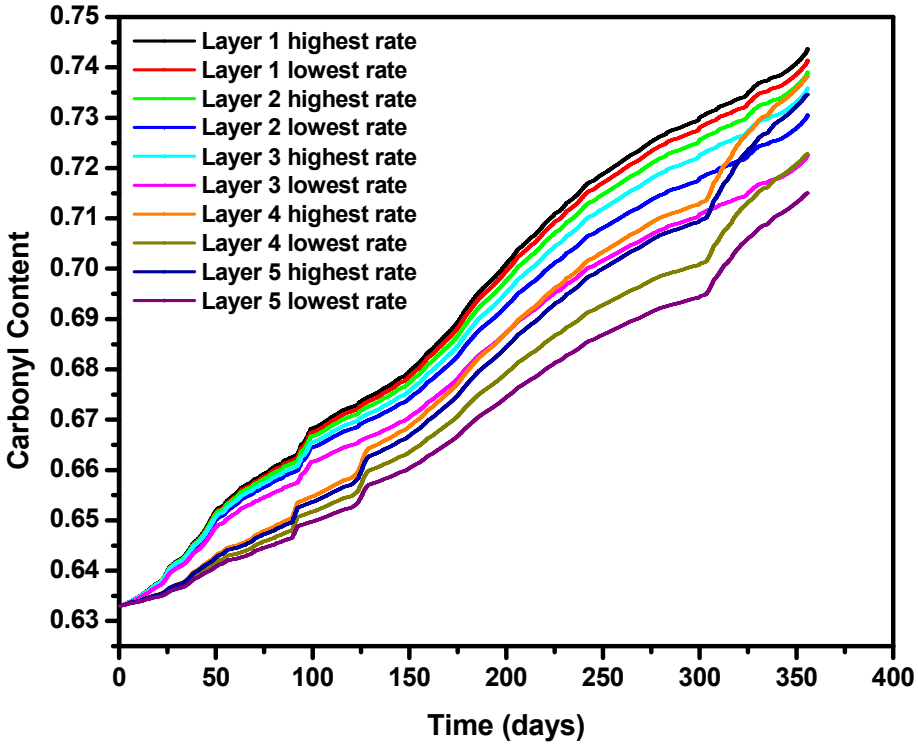

Figure C3-6 Bulk carbonyl growth rates (oxidation rates) of US54-AMR for one year period at different pavement layers

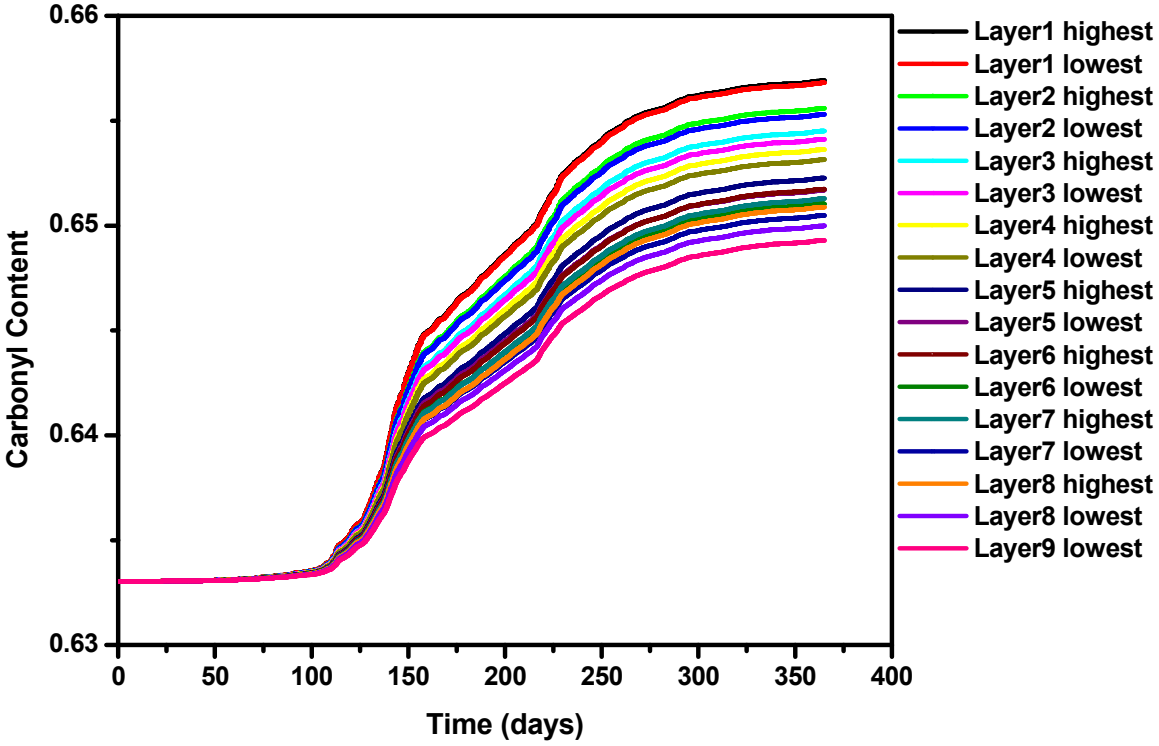

Figure C3-7 Bulk carbonyl growth rates (oxidation rates) of MN Cell1 for one year period at different pavement layers

VITA

Rongbin Han was born in Shaanxi, China. He received his Bachelor of Engineering in biochemical engineering from Tianjin University in Tianjin, China and his Master of Science in bioengineering from National University of Singapore in Singapore. He graduated with his Ph.D. in chemical engineering from Texas A&M University, College Station, Texas, in May 2011. He can be reached through the following address:

Department of Chemical Engineering, c/o Dr. Charles J. Glover
Texas A&M University
3122 TAMU
College Station, TX, 77843-3122